Summer 2015

NMR T$_1$ studies of colloidal unimolecular polymer (CUP) surface water

Yousef Abobaker Dawib

NMR T_1 STUDIES OF COLLOIDAL UNIMOLECULAR POLYMER (CUP)

SURFACE WATER

PROBING POLYMER CHAIN DYNAMICS BY SOLID STATE NMR

HETEROCYCLIC ORGANIC CORROSION INHIBITORS

by

YOUSEF ABOBAKER DAWIB

A DISSERTATION

Presented to the Faculty of the Graduate School of the

MISSOURI UNIVERSITY OF SCIENCE AND TECHNOLOGY

In Partial Fulfillment of the Requirements for the Degree

DOCTOR OF PHILOSOPHY

In

CHEMISTRY

2015

Approved

Dr. Michael R. Van De Mark, Advisor
Dr. Thomas P. Schuman
Dr. Jeffrey G. Winiarz
Dr. Amitava Choudhury
Dr. Surender Maddela

PUBLICATION DISSERTATION OPTION

This dissertation has been prepared in the form of three manuscripts for publication. Papers included are prepared as per the requirements of the journal in which they are submitted or to be submitted. This dissertation is formatted according to Missouri University of Science and Technology specification. This dissertation contains the following three manuscripts for publication:

PAPER I pages 27-57 will be submitted to the Colloid and Polymer science Journal

PAPER II pages 58-87 have been submitted to European Polymer Journal.

PAPER III pages 88-125 have been submitted to Corrosion Science Journal.

ABSTRACT

This dissertation is subdivided into three topics: Experimental study of colloidal unimolecular polymer (CUP) hydration; probing of polymer chain dynamics by ^{13}C solid state NMR technique; and the anticorrosive effect of 5-mercapto-1, 3, 4-thiadiazole-2(3H)-thione (MTT) derivatives.

The states of water in colloidal unimolecular polymer system were investigated by low field proton NMR. Bound and free water fractions were determined using spin-lattice relaxation measurements. A model equation was used to analyze the inversion recovery data.

The proton cross polarization and the pulse sequence for total spinning sideband suppression CP-TOSS NMR method were developed to determine the chain mobility of polymers as a function of temperature. ^{13}C solid state NMR spectra were analyzed over a temperature range 260K-370°K. Peak intensities of each carbon were plotted verses sample temperature. The plots revealed two linear regions with intersection point close to the first deviation temperature measured by differential scanning calorimetry (DSC).

Finally, various 5-mercapto-1,3,4-thiadiazole-2(3H)-thione (MTT) derivatives were synthesized and tested for their ability to inhibit corrosion on steel and 304 stainless steel substrates in a 3.5% NaCl solution. The effect of structure, substituent size, and steric hindrance on corrosion inhibitor performance were investigated. The size of substituent has a pronounced impact on corrosion inhibition ability.

ACKNOWLEDGMENTS

Foremost, I would like to express my sincere gratitude to my advisor, Dr. Michael R. Van De Mark for his guidance, support, and encouragement during the course of my work. His critical thinking improved my research skills and prepared me for future challenges. It was a great honor for me t to be part of his research group.

I am particularly thankful to Dr. Rex E. Gerald II for his inestimable support, and scientific advice. I am deeply grateful to him.

Special thanks are due to my committee members Dr. Thomas P. Schuman, Dr. Jeffrey G. Winiarz, Dr. Amitava Choudhury, and Dr. Surender Maddela for their support and guidance throughout the completion of my Ph.D. program.

I acknowledge my fellow lab mates in Van De Mark's Group: Cynthia Riddles, Dr. Jigar Mistry, Dr. Ming Han Chen, Dr. Ameya Natu, Dr.Sagar Gade, Catherine Hancock, and Peng Geng for their help and support at various occasions.

I gratefully acknowledge the Ministry of Higher Education – Libya for financial support during my pursuit of graduate studies at Missouri S&T.

Finally, I wish to thank my entire family, my parents, my sisters, and my brothers. Special thanks are due to my wife for her patience and support.

TABLE OF CONTENTS

LIST OF ILLUSTRATIONS

PAPER III

LIST OF TABLES

NOMENCLATURE

CUP	Colloidal Unimolecular Polymer
MEK	Methyl ethyl ketone
THF	Tetrahydrofuran
MMA	Methyl Methacrylate
MAA	Methacrylic acid
BA	Butyl Acrylate
AA	Acrylic Acid
TFEMA	2,2,2-trifluoroethyl methacrylate
AIBN	2,2′-azobis(2-methylpropionitrile)
ASTM	American Society for Testing and Materials
GPC	Gel Permeation Chromatography
NMR	Nuclear Magnetic Resonance
DSC	Differential Scanning Calorimetry
Tg	Glass Transition Temperature
^{1}HNMR	Proton Nuclear Magnetic Resonance Spectroscopy
Mn	Number Average Molecular Weight
DLS	Dynamic Light Scattering
AV	Acid Value
ASTM	American Society for Testing and Materials
KHP	Potassium Hydrogen Phthalate
P(MMA/MAA)	Methyl Methacrylate – co – Methacrylic Acid copolymer
ϕ	Bound Water Fraction
T_{1b}	Spin-lattice relaxation time constant of the bound water
T_{1f}	Spin-lattice relaxation time constant of the free water

η	Viscosity of Suspension
D	Diffusion Coefficient
γ	Gyromagnetic Ratio
FID	Free Induction Decay
RF	Radio Frequency
MAS	Magic Angle Spinning
CP	Cross Polarization
CP-MAS	Cross polarization combined with magic angle spinning
TOSS	Total Suppression of Spinning Sidebands
IHP	Inner Helmholtz Plane
OHP	Outer Helmholtz Plane
DL	Diffusion Layer
LFER	Linear -Free Energy Relationships
QSAR	Quantitative Structure Inhibition (activity) Relationship
HOMO	Highest Occupied Molecular Orbital
LUMO	Lowest Unoccupied Molecular Orbital
MTT	5-mercapto-1,3,4-thiadiazole-2(3H)-thione
R_Ω	Solution Resistance
CPE	Constant Phase Element
Rct	Charge Transfer Resistance
EIS	Electrochemical Impedance Spectroscopy

1. INTRODUCTION

1.1 COLLOIDAL UNIMOLECULAR POLYMER

Colloidal unimolecular polymer (CUP) is a unique colloidal system contains true nanoparticles dispersed in aqueous media. The CUP particles are spheroidal particles that have a collapsed hydrophobic backbone and charged surface, see Figure 1.1 [1,2]. The polymer-solvent and polymer-polymer interactions have the key role in formation of CUP particles. In view of Flory-Huggins theory, a copolymer of methyl methacrylate (MMA) and methacrylic acid (MAA) prefers to be in random coil configuration in organic solvent as a result of strong polymer-solvent interaction. Changing the solution media from organic to the mixture of organic and water results in changing the polymer's configuration due to decrease in polymer-solvent interaction and an increase in polymer-polymer interaction. Removing the organic solvent results in a spheroidal particle. The presence of charged groups on CUP surface prevents particle aggregation and drives its spheroidal shape. The typical size of CUP particle is 2-9 nm based on the molecular weight of copolymer. Due to its size, the surface area per unit gram is ultra-high. These water-based particles can hold an appreciable amount of water associated with its surface that play a decisive role in CUP properties and application. A previous study [3] on CUP-water interaction confirmed the presence of approximately two water layers associated with CUP particle.
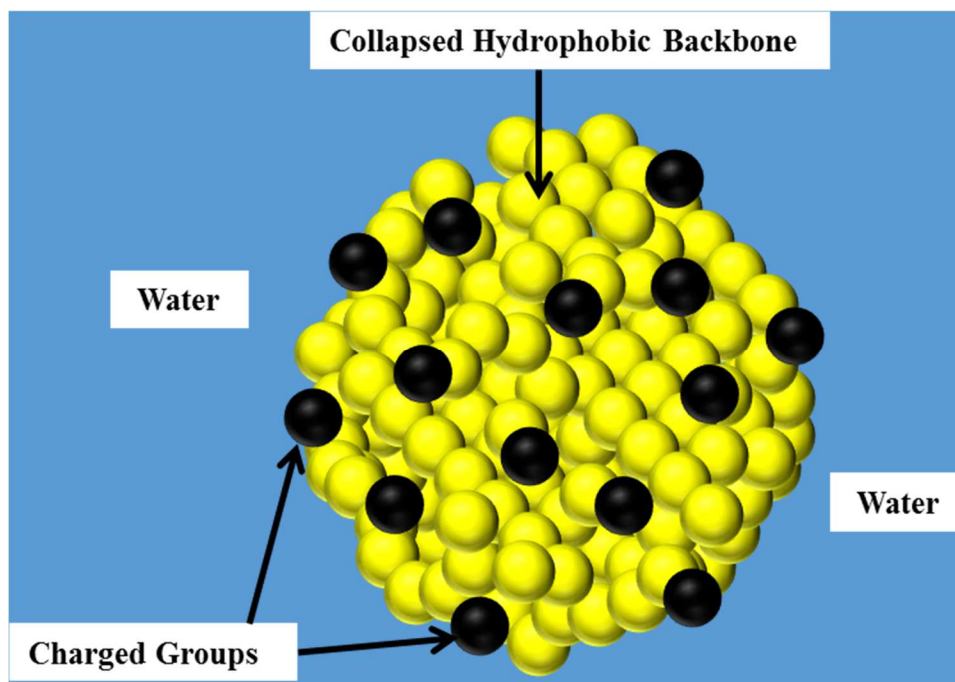
Figure 1.1. Colloidal Unimolecular Particle (CUP).

1.1.1 Bound Water

Newton and Gortner [4] have proposed that colloidal particles always have an associated amount of surface water known as bound water. The states of water in colloidal system consist of free or ordinary water, and bound or associated water, so, the colloidal system is defined by a two-phase model [5, 6]. It has been found that the bound water molecules are significantly different in their properties from that of bulk water [6].

In the past, many attempts have been made to furnish evidence on the existence of bound water in biological and colloidal systems. Moran [7] used a dilatometric method to measure the amount of bound water in a mammalian muscle within a temperature range of -1.5 to -20˚C. Unfortunately, he was unable to detect an appreciable amount of bound water. Hill [8] was also unable to

detect a considerable amount of bound water in different colloidal systems. Greenberg and Greenberg [9] reported the same finding when they used an ultrafiltration method to determine bound water in solutions of gelatin, casein, starch, glycogen, and blood serum. They assumed that "bound" water loses its solvent properties, and only a very tiny fraction of the water can be associated with the colloids in this form.

In 1930, Grollman [10] studied the state of water in gelatin and gum acacia by using vapor pressure measurements. Results indicated that the hydration in gelatin is relatively small at pH=7 and cannot be detected in gum acacia solutions. In conclusion, hydrophilic colloids do not need to be strongly hydrated. However, Gortner [11] looked for different approaches when he used freezing-point depression measurements to determine the amount of bound water in gum acacia in aqueous sucrose solutions. Results revealed that the amount of bound water extended up to 0.6-0.7 grams per gram of gum. He considered this to be evidence that bound water does exist.

In1952, Buchanan et al. [12] conducted microwave dielectric measurements on a protein solution to estimate the amount of bound water associated with proteins. This technique is based on the fact that bound water molecules are unable to rotate at high frequency field. Therefore, bound water molecules that hydrate a protein would have an influence on dielectric constant measurement. Results of this study indicated that bound water molecules shows no change over the pH range 2.1-11.7. Moreover, estimation of bound water

molecules for serum albumin shows no change within the temperature range 15-40° C.

Differential scanning calorimetry (DSC) has also been used to determine the bound water fraction of macromolecule systems. The method is based on the measurement of the heat of melting or crystallization of water. Wang and Gunasekaran [13] studied the state of water in a chitosan and polyvinyl alcohol (PVA) hydrogel. They concluded that the bound water fraction increased as the PVA concentration increase. In addition, results revealed that the addition of hydrophilic groups lowers both the total water content and free water content. Polyvinyl alcohol contains the hydrophilic group –OH. This group has a tendency to form a hydrogen bond with free water molecules, producing a higher bound water fraction. Siahboomi et al. [14] validated this finding when they studied the water distribution within cellulous ethers. They concluded that the bound water quantity is highly dependent on the substitution type on the polymer chains. The highest bound water content was recorded when the hydrophilic substituent (hydroxypropylcellulose) was present on the polymer chain.

The quantification of a bound water fraction was also studied by infrared spectroscopy [15]. This technique relies on measurements of a change in the natural vibration frequency produced by an interaction between water molecules and polymer's solid surface. Results from methylcellulose films exposed to several humid environments indicated the existence of two types of water: bound water and free water. These results also revealed that bound water increases as the moisture on the methylcellulose films increased.

Additionally, a Raman spectroscopy technique was used to study the state of water in polymer solutions. Sekine and co-worker [16] investigated the temperature dependence of structural changes of bound water in dried glassy poly-N, N,-dimethylacrylamide in the temperature range 286.1-329.7° K. Results indicated the presence of two type of bound water. First type: water is forming a shell layer around polymer chains. And the second type: water is bound to the polar groups of polymer chains. At temperature below 310°K, water molecules that exist in shell layer evaporates whereas the second water type began to evaporate above 310°K.

As the bound water molecules have lower mobility than free water molecules, nuclear magnetic resonance (NMR) is the most useful technique for studying molecular mobility. The nuclear spin-lattice relaxation time (T_1) is directly related to the molecular motion. The spin-lattice relaxation (T_1) is a process that quantifies the rate of energy transfer from excited spins to the surrounding molecules "the lattice". This relaxation process can be described by the Bloch equation:

$$M_Z = M_O(1 - e^{\frac{-t}{T_1}})$$

(1)

Where M_z is the magnetization at time t and Mo is the magnetization at equilibrium.

The objective of this part of the research was to investigate and characterize the states of water in colloidal unimolecular polymer (CUP) suspension systems.

The work includes synthesizing of two acrylic copolymers (polymethyl methacrylate/methacrylic acid) with molar ratio of MMA: MAA 9:1, and different molecular weight. Various concentrations of CUP solutions were prepared in order to carry out the low field NMR study. Based on the fact that spin-lattice relaxation time (T_1) of bound water molecules is lower than free water molecules, T_1 were measured as a function of CUP concentration, CUP size, and temperature. The bound and free water population was calculated using a model equation. The bound water relaxation time T_{1b} was also calculated.

1.2 POLYMER DYNAMICS

The polymers applications are determined based on their state as a function of temperature. Amorphous polymers are in glassy state at low temperature and as temperature increases, the polymer becomes soft and this state represents so-called the rubbery state. The transition from glassy to rubbery state occurs over a temperature range known as a glass transition region. At the glass transition temperature, the polymer molecules begin reptational motion [17]. The glass transition temperature is associated with a change in some properties, these are specific heat capacity, elasticity modulus, viscosity, refractive index, and coefficient of thermal expansion [17, 18]. The determination of the glass transition temperature relies on measuring these properties as a function of temperature. One of the most utilized method in measuring glass transition temperature is the differential scanning calorimetry method (DSC). In the DSC method, the polymer sample is subjected to a programmed linear temperature change, and the heat flow into or out of a sample

is measured. The glass transition temperature is defined as the temperature at which one half of the increase in the heat capacity has occurred [17, 18]. As the polymer molecule attains motion, the heat capacity increases. According to ASTM standard E1356 – 08[19], the glass transition temperature region is represented by a range of temperatures, not only a specific temperature, see Figure 1.2.
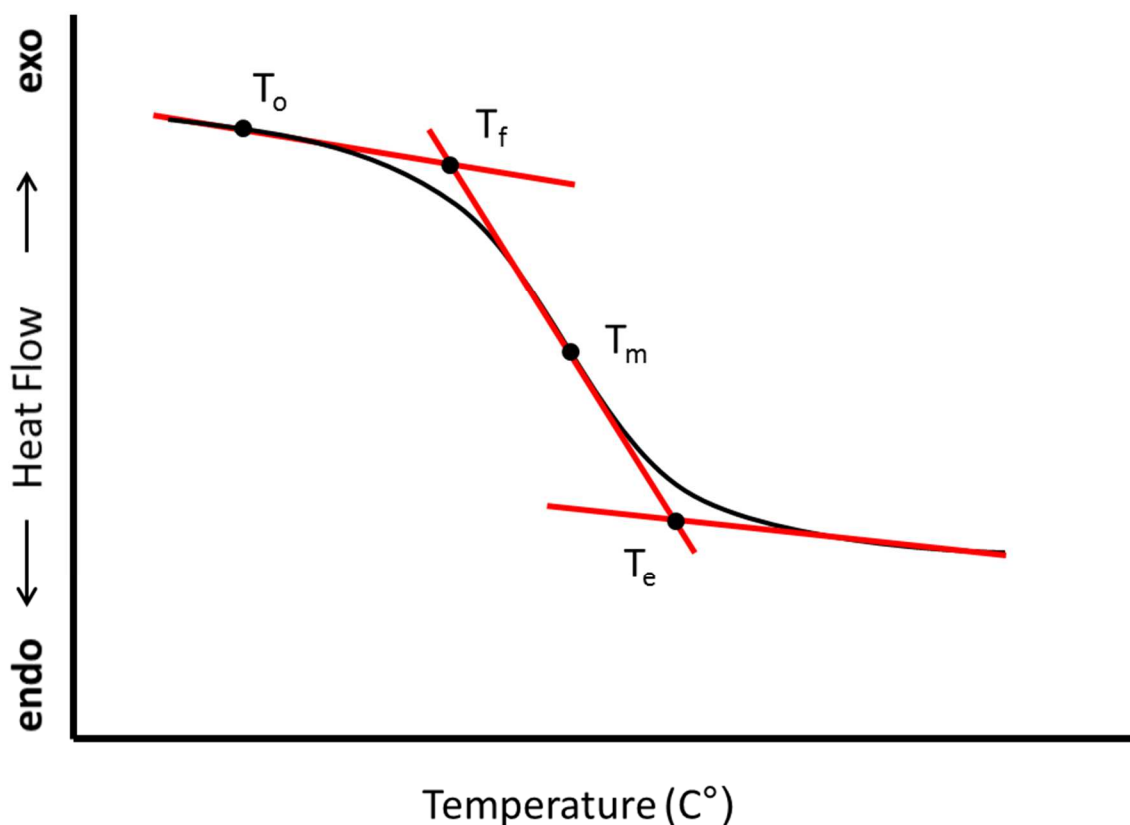
Figure 1.2. Glass transition region measured temperatures.

Where T_o is a temperature of first deviation (the point of first detectable deviation from the extrapolated baseline prior to the transition), T_f is an extrapolated onset temperature (point of intersection of the tangent drawn at the point of greatest slope on the transition curve with the extrapolated baseline prior

to the transition), T_m is a midpoint temperature (the point on the thermal curve corresponding to 1⁄2 the heat flow difference between the extrapolated onset and extrapolated end, and T_e is an extrapolated end temperature (the point of intersection of the tangent drawn at the point of greatest slope on the transition curve with the extrapolated baseline following the transition[19].

1.2.1 Nuclear Magnetic Resonance Spectroscopy

There is no doubt that the nuclear magnetic resonance spectroscopy (NMR) is one of the most powerful techniques in providing information about molecular architecture and dynamics. The wide applications and popularity of NMR spectroscopy emerge from the fact that this technique can be applied on a large number of samples using a variety of methods. Broad-line proton NMR measurements have been used to study polymer dynamics [20]. It has been found that at temperatures below the glass transition temperature, the line is broad, and at temperature above, the signal is sharp. The reason behind this change is attributed to the increase in random proton orientation distribution as the chain segments become more mobile [20].

The basic principle of NMR technique is established in view of the quantum physical concept that protons possess spin that generates its own magnetic moment, and placing the sample in strong external magnetic field allows characterizing its behavior. In the absence of magnetic field, the individual nuclear magnetic moments have random orientation. Once the external magnetic field applied, the nuclear magnetic moments either aligned preferentially with or against magnetic field. As a result, two spin states are

generated, low energy state α where nuclear spin magnetic moment aligned with magnetic field and high energy state β where nuclear spin magnetic moment aligned against magnetic field. The magnetic moment of spin starts to rotate (precession) about the axis of magnetic field. The precession is called a Larmor frequency ω_o and equal to:

$$\omega_o = -\gamma B_o \tag{2}$$

Where γ is the gyromagnetic ratio, a characteristic constant of each type of nucleus, and B_o is the applied magnetic field. The radio frequency pulse RF applied in order to perturb the system. As a result, the net magnetization rotates in xy, and magnetization precession about xy plane, an oscillating signal is induced. This signal is called a free induction decay (FID) [21-23].

1.2.1.1 Chemical Shift Anisotropy

In NMR experiments, the nucleus absorbs radiation at a frequency known as a chemical shift. The chemical shift value greatly depends on the environment surrounding the nucleus. Electron distribution around nucleus can either shield or deshield the nucleus from an external magnetic field. The orientation of a nucleus is important in determining the magnitude of the shielding. In the liquid state, the molecule is tumbling very fast, so the chemical shift observed is the average of the shift corresponding to different orientations. This is known as an isotropic chemical shift. Contrary to liquid, in the solid state there is a lack of molecular-level motion. Molecules are not tumbling, so the molecular orientations are almost equal. The chemical shift is the so-called anisotropic and results from

molecules that are almost static with respect to external magnetic field. The signal obtained in solid state NMR depends on the molecular orientation, hence broad NMR lineshapes are produced.

1.2.1.2 Dipolar Coupling

Nuclear spin produces a magnetic moment, and a dipolar field is generated. A nuclei neighboring the dipolar field will sense this field, and spin interaction takes place. This interaction occurs through space and the dipolar coupling constant of two nuclei I and S separated by internuclear distance, r, is equal to

$$R_{IS} = \frac{\mu_o \gamma_I \gamma_S \hbar}{4\pi r_{IS}^3}$$
(3)

The dipolar coupling constant is highly dependent upon the distance between two spins and their gyromagnetic ratio. For example, the hetronuclear interaction of C-H is lower than the H-H interaction with similar distance. Dipolar interaction can not be observed in the liquid state because molecules are moving, thus dipolar coupling changes and average to zero. However, unlike the liquid state, molecules in the solid state do not freely tumble, and the dipolar interaction becomes pronounced. Another factor that effects the energy of dipolar interaction is the angle between the external field and the vector joining the two spins.

$$E = \frac{A}{r^3}(1 - 3\cos^2\theta)$$
(4)

Where r is the distance between the two spins and Θ is the angle between the external field and the vector joining the two spins. The constant A depends on the magnetic moment of the two spins. See Figure 1.3.
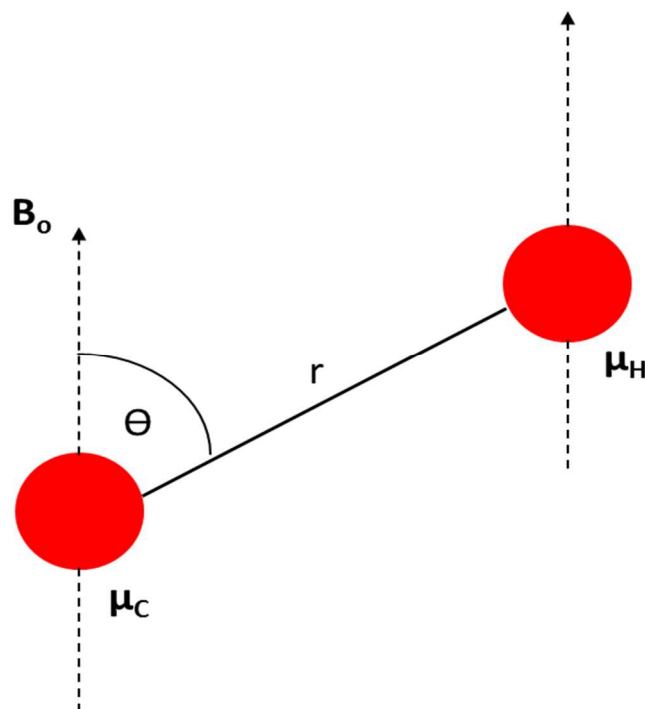
Figure 1.3. Dipolar interaction between ^{1}H spin and ^{13}C spin.

The dipolar coupling or chemical shift anisotropy can not be removed from the spectra and make it difficult to interpret the solid state NMR spectra. Fortunately, due to the recent development in solid state technique, the dipolar coupling and chemical shift anisotropy issues has been solved and can easily get NMR spectra free of these effects [21, 22].

1.2.1.3 Magic-Angle Spinning

Identical nucleuses in the solid state are oriented differently to B_o, therefore, produce a broad line. Very rapid sample spinning at an angle of approximately 54.7° is adequate to average $(3\cos^2\theta-1)$ to zero, as a consequence, the signal intensity enhances and sharp lines are produced. The 54.7° is called magic angle spinning (MAS). MAS removes the effect of both the chemical shift anisotropy and dipolar coupling [21, 22].Figure 1.4 depicted the MAS.
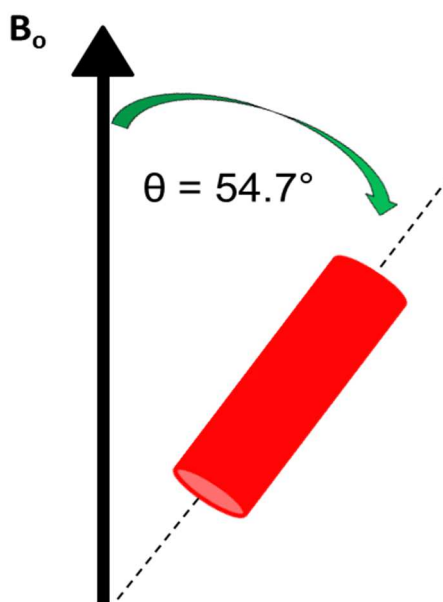
Figure 1.4. Magic angle spinning.

1.2.1.4 Cross Polarization

The ^{13}C isotopic abundance in solid state is low, and their relaxation time is long. Recording of the FID cannot be easily achieved. In order to circumvent this problem, pulses are applied on the proton and carbon frequencies. It is

required that the precession frequencies of all nuclei are approximately similar. This can be achieved by applying spin-locking field of the same strength on both proton and carbon spins. Transferring polarization from the proton to carbon atom greatly enhances the signal intensity [21, 24]. Figure 1.5 illustrates a diagram of cross polarization.
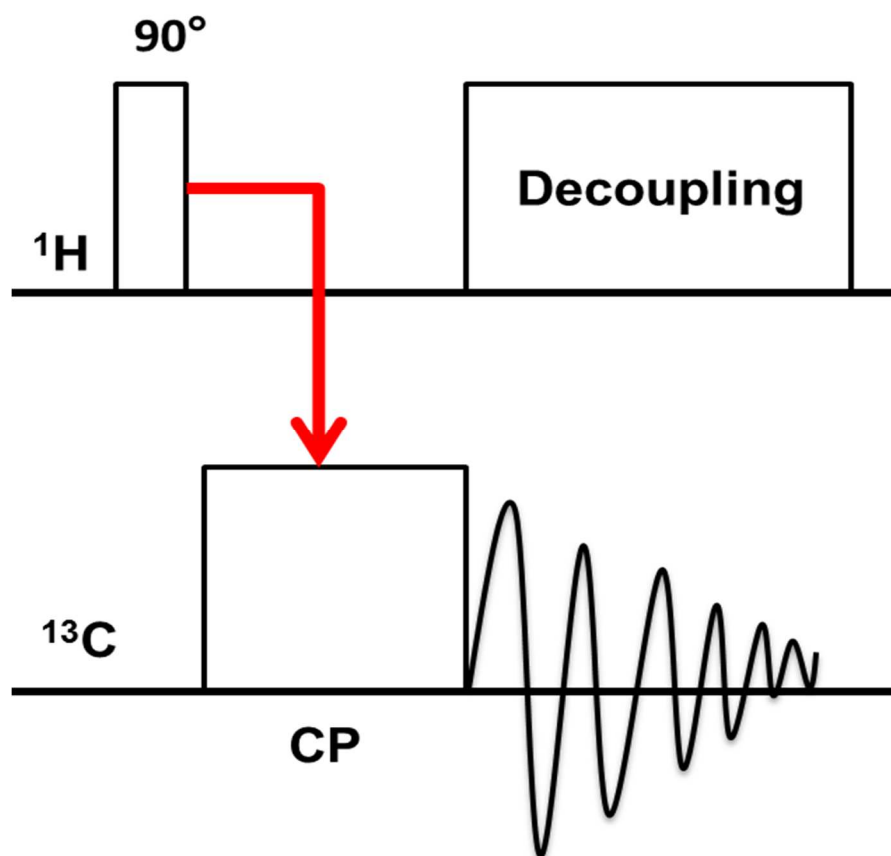
Figure 1.5. Schematic diagram of employing cross polarization.

A 90° pulse applied to the ^{1}H spin creates transverse ^{1}H spin which is transferred to the ^{13}C spin. Decoupling is applied to the ^{1}H spin for line narrowing of the ^{13}C spin spectrum during acquisition [25].

1.2.1.5 Total Suppression of Spinning Sidebands

Spinning of solid state NMR samples produce spectra that contain sets of sidebands. Therefore, the spectra assignments and interpretation are complicated [26]. The most utilized technique to eliminate spinning sidebands from CP-MAS spectra is total suppression of spinning sidebands (TOSS). Dixon [27, 28] demonstrated this method by using a series of pulses synchronized with the MAS rotor [26, 27, 28].The 180° pulses can change a precessing nucleus's phase, thus sidebands disappear and only centerbands are left [26-28].

The objective of this part of the research was to study polymer chain dynamic of both homopolymer and copolymer by ^{13}C CP-TOSS method. This method was developed in view of the fact that the carbon signal intensity dependence on the distance of neighboring protons and the angle between the external field and the vector joining the carbon and proton spins. Temperature variation of the polymer sample will result in changing these two parameters (distance and angle). At a certain temperature, the change in peak intensity will become significant. This temperature will be defined as the temperature at which each segment in polymer chain attains the onset motion which can be related to a polymer glass transition temperature (Tg).

1.3. CORROSION

Corrosion is a process that causes material degradation. The National Association of Corrosion Engineering defines corrosion as the degradation of material that results from a reaction with its environment [29]. Ores contain chemically combined state of metals, typically an oxide. The ores possess the

lowest energy state, therefore, it is the most stable state by nature. Conversion of ores into metals requires energy to be supplied in order to accomplish the transformation. The metals uses in our life exist in higher energy state than ores, and according to thermodynamic laws, they have a great potential to convert back to their original oxidized state. The metal degradation occurs via electrochemical reactions, oxidation and reduction reactions. The two reactions have to be combined and cannot occur separately. Metals loose electrons by an oxidation reaction known as the anodic reaction and take place at the anode. The reduction reaction consumes electrons by reduction reaction known as the cathodic reaction, and take place at the cathode. In general, the corrosion of steel typically consist of the oxidation of iron and the reduction of a non-metallic species. At the anode, iron oxidizes and forms a soluble ferrous iron:

$$Fe \rightarrow Fe^{+2} + 2\ e^-$$

At the cathode, oxygen reduction is the major reduction reaction. In neutral, and alkaline solutions, both oxygen and water presence at the cathode and act as electron acceptor.

$$\tfrac{1}{2}\ O_2 + H_2O + 2e^- \rightarrow 2OH^-$$
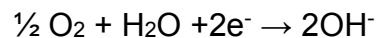
In dearated acidic or neutral solutions, the only possible reduction reactions is the hydrogen evolution reaction

$$2H+ + 2e^- \rightarrow H_2$$

$$2H_2O + 2e^- \rightarrow H_2 + 2OH^-$$
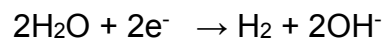
Both oxygen reduction and hydrogen evolution generate hydroxyl ions, thus the pH at the cathode increases. The oxygen reduction become the predominant cathodic reaction at high pH [30-32].

The cathodic and the anodic reactions are coupled, thus the rate of anodic reaction will be directly proportional to the rate of cathodic reaction. When a metal comes in contact with an aqueous environment, oxidation of metal begins at high rate; metal atoms are removed from their lattice to metal cations into the electrolyte. Eventually, dynamic equilibrium is attained and the oxidation process slows to zero as a result of negative charge build up on metal surface. Polar water molecule will be attracted to the negatively charged metal surface to form an ionic structure layer [33]. Figure 1.6 shows a schematic electrical double-layer model.
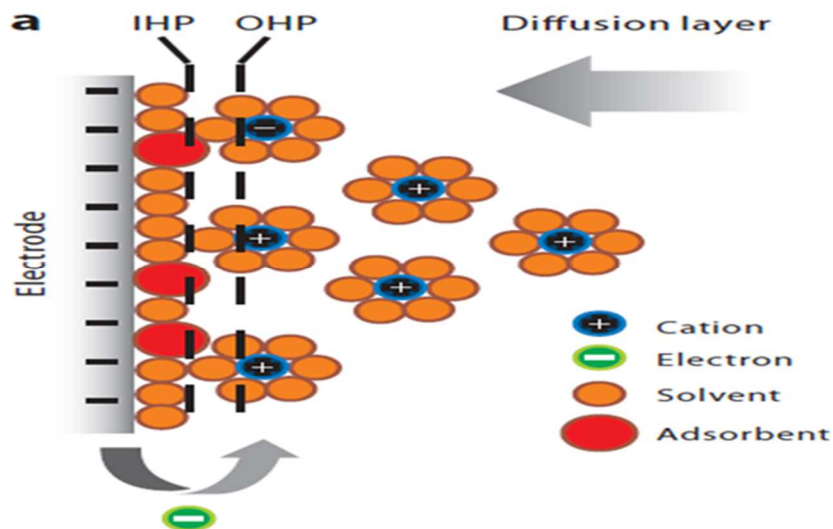
Figure 1.6. Schematic electrical double layer [34].

Electrical double layer consist of:

1-The Inner Helmholtz Plane (IHP) which is an ionic layer that consists of adsorbed dipole molecules. Only specific adsorbed anions bonded to metal surface.

2-The Outer Helmholtz Plane (OHP) consists of a plane of adsorbed solvated cations.

3-The Diffusion Layer (DL) is a thick layer located in a region of diffuse ions in contact with the OHP and the bulk of the solution.

1.3.1. Organic Corrosion Inhibitors

One of the approaches to inhibit corrosion is to eliminate contact between metal and electrolyte. Organic inhibitors can adsorb on metal surface and form a protective barrier that blocks the active dissolution sites of metal. Once the organic molecule reaches the metal surface, adsorption of the inhibitor molecule takes place. This will led to change in the potential difference between the metal surface and the electrolyte as a result of unbalanced electric charge distribution at metal- solution interface [32]. Adsorption of organic molecule on metal surface is governed by residual charge on the surface of the metal and chemical structure of inhibitor [32]. The two main types of the adsorption of an organic inhibitor on a metal surface are physical and chemisorption. Chemisorption is the transfer, or sharing of the inhibitor molecules electrons (ligation) to the metal surface, forming a coordinate-type bond [32].

Organic molecules have to have various aspects in order to be able to inhibit the corrosion process. The organic molecules should have reactive atoms which is the active site of chemisorption process and the strength of chemisorption relies on the electron density and polarizability of these functioning atoms [32]. The effectiveness of functioning atoms in the adsorption process varies according to the following sequence:

Selenium > Sulfur > Nitrogen > Oxygen
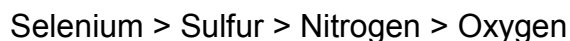
This order is explained by lower electronegativity of elements on the left that make their compounds easily susceptible to polarization [35]. Additionally, the affinities of organic molecule toward a metal surface highly influence the binding strength. In terms of their polarizability, organic inhibitors can be classified as either soft or hard inhibitors. The hard molecule is a molecule that has high charge density and a small orbital. In turn, the soft molecule is a molecule that has lower charge density and a larger orbital. According to the soft and hard theory [36] the metal prefers to bond to a soft base (i.e., sulfur-containing inhibitors). However, the hard bases (i.e., nitrogen-containing inhibitors) do not adsorb as strongly on metal surface as do sulfur containing inhibitors [32, 35, 36, 37].

A substituent on an organic molecule may alter its inhibition ability. In view of this proposition, the Hammett equation [38] has been utilized in the field of organic corrosion inhibitors. The effectiveness of inhibitors can be correlated with Hammett's σ parameter by conducting linear -free energy relationships (LFER) [39]. These relationships assume that the substituent electronic structure

plays an important role on the adsorption process. Either the LFER or Hammett relation is given by [40, 41].

$$\log \frac{R}{R_o} = \rho\sigma$$

(5)

Where Ro and R are the corrosion rates in the absence and presence of inhibitors, respectively, ρ is the constant for given reaction, and σ reflects the influence of a substituent on the electron density of reaction center in molecule. The negative σ value represents the electron donating property of the substituent. The substituents that attract electrons from the reaction center are assigned a positive σ value. A study of triazole derivatives[41] found that plotting log R/ Ro vs σ produce a good correlation by providing a straight line with slope ρ= 1. The positive sign indicates that the corrosion process is inhibited by increasing electron's density at electron's center. Sastri and Perumareddi [42] conducted a study on pyridine derivatives and concluded that either the corrosion rate decreased or the percent inhibition increased as the negative σ value increased.

The molecular weight of an organic molecule has been correlated with the ability of that molecule to retard corrosion. Li, Tan and Lee [43] suggested that the molecular weight of an organic molecule greatly influences the corrosion inhibitive efficiency. They deduced that a larger molecule will offer better corrosion protection as long as the molecule still possesses a minimum solubility in water.

Previous studies correlated the compound symmetry to corrosion inhibition property. Foster et al [44] concluded that symmetrical compounds have poor inhibitive properties. However, there is lack of studies to support this proposition. Later study indicated that organic compounds with an asymmetrical structure are more effective inhibitors than compounds with a symmetrical structure [35].

Many studies [45-49] have correlated quantum chemical parameters to corrosion inhibition efficiencies by the quantitative structure inhibition (activity) relationship (QSAR) approach. The highest occupied molecular orbital (HOMO), the lowest unoccupied molecular orbital (LUMO), the HOMO–LUMO gap, and the dipole moment (μ) have each been used to characterize inhibitor performance. The HOMO is the highest energy orbital containing electrons. These electrons can be easily donated to metals surface to form coordinating bonds. The organic molecules that have high HOMO energy have a great tendency to donate electrons to unoccupied d orbitals of the metal. The interaction between organic molecule and metal substrate increase the corrosion inhibitive efficiency of organic molecules [32]. The LUMO is the lowest energy empty orbital, and is associated with the ability of a molecule to accept electrons. The lower the ELUMO value of molecule the more likely it is to accept electrons. Thus, the effective corrosion inhibitor molecule is capable of electron donating to the unoccupied orbital of the metal in conjunction with its ability to accept free electrons from the metal [45]. The EHOMO–ELUMO energy difference is directly related to the molecule's stability. A large energy gap results in a high stability

during chemical reactions [47, 48]. A smaller (EHOMO-ELOMO) gap leads to easier polarization. Sastri [42, 49] found that a smaller EHOMO-ELOMO value can enhance corrosion inhibition. The dipole moment is an indication of an organic molecule's polarity [47]. It has been stated that the organic molecule with low dipole moment is more prone to adsorb on metal surface and display good inhibition performance [45, 50]. However, other studies [47, 51] stated that there is no correlation between the dipole moment and the inhibition efficiency.

5-mercapto-1,3,4-thiadiazole-2(3H)-thione (MTT) is one of the organic compounds that possess many reactive atoms. This compound has three sulphur atoms and two nitrogen atoms. In addition, it has two acidic hydrogen that can be easily substituted. The corrosion inhibition performance of this compound in acidic solution has been investigated [52]. Results indicated that MTT inhibit corrosion process of mild steel and copper in acid solutions.

The objective of this part is to synthesis a series of 5-mercapto-1, 3, 4-thiadiazole-2(3H)-thione (MTT) derivatives. The corrosion inhibition efficiency of these derivative on different metal surfaces in 3.5% NaCl was investigated by two techniques, electrochemical impedance spectroscopy and electrochemical polarization. The chemical structure of MTT derivative were correlated with their corrosion inhibition efficiency. The goal was to assess which factor of molecule chemical structure has a more pronounced impact of corrosion inhibition performance.

REFERENCES

1. Riddles C J, Zhao W Hu, Hua-Jung, Chen M, Van De Mark, Michael R. "Self-assembly of water insoluble polymers into Colloidal Unimolecular Polymer (CUP) particles of 3-9 nm," Polymer, Vol. 55, No.1, pp 48-57 (2014).

2. Chen M, Riddles C J., Van De Mark, Michael R. "Electroviscous Contribution to the Rheology of Colloidal Unimolecular Polymer (CUP) Particles in Water," Langmuir, Vol. 29, No.46, pp 14034-14043 (2013).

3. Chen M, Riddles C J, Van De Mark, Michael. "Gel point behavior of colloidal unimolecular polymer (CUP) particles," Colloid. Polym. Sci., Vol.291, No.12, pp 2893-2901 (2013).

4. Newton R, Gortner R A. "A method for estimating hydrophilic colloid content of expressed plant tissue fluids". Bot. Gaz,Vol 74 pp 442–446(1922).

5. Gortner R A. "The state of water in colloidal and living systems," Transactions of the Faraday Society, Vol. 26, pp 678-704(1930).

6. Chandler, Ray Calvin. "Nature of bound water in colloidal systems," Plant Physiology, Vol. 16, pp 273-91(1941).

7. Moran T, "Frozen state in mammalian muscle," Proceedings of the Royal Society of London, Series B, Vol. 107, pp182-187 (1930).

8. Hill A.V, "State of water in muscle and blood and the osmotic behavior of muscle," Proceedings of the Royal Society of London, Series B, Vol. 106, pp 477-505 (1930).

9. Greenberg D M, Greenberg M M, "Ultrafiltration. II. "Bound" water (hydration) of biological colloids," The Journal of general physiology, Vol. 16, No.4, 559-69 (1933).

10. Grollman, A, "The vapor pressures of aqueous solutions with special reference to the problem of the state of water in biological fluids," The Journal of general physiology , Vol.14, No.5, pp 661-683 (1931).

11. R Gortner R A, Gortner W A, "The cryoscopic method for the determination of "bound water," The Journal of general physiology, Vol.17, pp 327-39 (1933).

12. Buchanan T J, Haggis G H, Hasted J B and Robinson B G, "The dielectric estimation of protein hydration," Proceedings of the Royal Society of London. Series A, Mathematical and Physical Sciences, Vol. 213, No. 1114, pp. 379-391(1952).

13. Tao Wang, Sundaram Gunasekaran, "State of water in chitosan-PVA hydrogel," Journal of Applied Polymer Science, Vol. 101, pp 3227–3232 (2006).

14. McCrystal C. B, Ford, J. L, Rajabi-Siahboomi, A. R, "Water Distribution Studies within Cellulose Ethers Using Differential Scanning Calorimetry. 2. Effect of Polymer Substitution Type and Drug Addition," Journal of Pharmaceutical Sciences, Vol. 88, No. 8, pp 797-80 (1999).

15. Velazquez G , Herrera-Gomez A, Martın-Polo M O, "Identification of bound water through infrared spectroscopy in methylcellulose," Journal of Food Engineering, Vol.59, pp 79–84 (2003).

16. Yurina Sekine, Tomoko Ikeda-Fukazawa, "Temperature Dependence of the Structure of Bound Water in Dried Glassy Poly-N,N,-dimethylacrylamide," Journal of Physical Chemistry, Vol.114, 3419–3425 (2010).

17. Sperling L.H. Introduction to physical polymer science, Fouth edition, John Wiley & Sons, Inc. pp 349 (2006).

18. Painter P C, Coleman M M, Fundamentals of Polymer Science, Technomic Publishing Company,Inc, page247—287(1994).

19. ASTM E1356 −08, Standard Test Method for Assignment of the Glass Transition Temperatures by Differential Scanning Calorimetry.

20. Apperley D C, Hodgkinson P, Harris R K, Solid-state NMR: Basic Principles & Practice, Momentum Press, LLC (2012).

21. Jurt S, Zerbe O, Applied NMR Spectroscopy for Chemists and Life scientist, (2013).

22. Duer M J, Solid State NMR Spectroscopy: Principles and Applications, Wiley (2008).

23. Fyfe C A, Mossbruger H, and Yannoni C S, "A Simple'Magic-Angle' Spinning Apparatus for Routine Use in NMR Spectroscopy of Solids," J. Magn. Reson. Vol. 36, pp 61-68 (1979).

24. Rovnyak D, "Tutorial on Analytic Theory for Cross-Polarization in Solid State NMR," Concepts in Magnetic Resonance Part A, Vol. 32A, No.4, pp 254–276 (2008).

25. Metz G, Wu X, Smith S O, "Ramped-amplitude cross polarization in magic-angle-spinning NMR," Journal of Magnetic Resonance, Series A, Vol.110, No.2, pp 219-227 (1994).

26. Antzutkin O N, Song Z, Feng X, Levitt M H, "Suppression of sidebands in magic-angle-spinning nuclear magnetic resonance: general principles and analytical solutions," Journal of Chemical Physics, Vol. 100, No.1, pp130-40(1994).

27. Dixon, W. T., Schaefer J, Sefcik M. D, Stejskal E. O, and McKay R A "Total Suppression of Spinning Sidebands in CPMAS C-13 NMR," Journal of Magnetic Resonance, Vol. 49, No.2, pp341-345 (1982).

28. Dixon W.T, "Spinning-sideband-free and spinning-sideband-only NMR spectra in spinning samples," Journal of Chemical Physics, Vol. 77, No.4, pp1800-1809 (1982).

29. Van Delinder L S, Corrosion Basics, an Introduction, Houston, TX: NACE, (1984).

30. Shreir L L, Corrosion, John Wiley & Sons, Inc. Volume 1, (1976).

31. Talbot D, Talbot J, Corrosion Science and Technology, CRC Press LLC, (1998).

32. Sastri V S, Corrosion Inhibitors: Principle and Applications, John Wiley & Sons, Inc, New York, (1998).

33. Nestor P, Electrochemistry and Corrosion Science, Kluwer Academic Publishers, (2004).

34. Byoung-Yong C, Su-Moon P, "Electrochemical impedance spectroscopy," Annual review of analytical chemistry, Vol.3, pp 207–229 (2010).

35. Rozenfeld I L, Corrosion Inhibitors, McGraw-Hill Inc., New York (1981).

36. Pearson R G, "Hard and soft acids and bases (HSAB). I. Fundamental principles," Journal of Chemical Education, Vol.45, No.9, 581-587(1968).

37. Aramaki K, Mochizuki T, Nishihara H, Proc.10th Int. Congress on Metallic Corrosion, New Delhi, India. Vol. 3, pp 2759(1987).

38. Hammett L P, "Some relations between reaction rates and equilibrium constants," Chem.Rev, Vol. 17, pp 125-136 (1935).

39. Donahue F M, Nobe K, "Theory of organic corrosion inhibitors. Adsorption and linear free energy relations," Journal of electrochemical society, Vol.112, No.9, pp886-891(1965).

40. Vasseghi S, Nobe K, "The effect of substituted purines on the corrosion behavior of iron," Corrosion NACE, Vol. 35, No.7, pp 300-303 (1979).

41. Tadros A B, Abd-El-Nabey B.A, "Inhibition of the acid corrosion of steel by 4-amino-3-hydrazino-5-thio-1,2,4-triazoles," Journal of Electroanalytical Chemistry and Interfacial Electrochemistry, Vol. 246, No. 2, pp 433-439 (1988).

42. Sastri V S, Perumareddi J R, "Selection of corrosion inhibitors for use in sour media," Corrosion, Vol. 50, No.6, pp 432-437 (1994).

43. Li P, Tan T C, Lee J Y, "Gray relational analysis of amine inhibition of mild steel corrosion in acids," Corrosion (NACE),Vol. 53, No.3, pp 186-194 (1997).

44. Foster G L, Oakes B D, Kucera C H, "Acetylenic corrosion inhibitors," Industrial and Engineering Chemistry, Vol.51, pp 825-828 (1959).

45. Fang J, Li J, "Quantum chemistry study on the relationship between molecular structure and corrosion inhibition efficiency of amides," Journal of Molecular Structure, Vol. 593, pp 179–185 (2002).

46. El Ashry E H , El Nemr A, Esawy S A, Ragab S, "Corrosion inhibitors. Part II: Quantum chemical studies on the corrosion inhibition of steel in acidic medium by some triazole, oxadiazole and thiadiazole derivatives," Electrochimica Acta, Vol. 51, No.19, pp 3957–3968 (2006).

47. Gokhan G, "The use of quantum chemical methods in corrosion inhibitor studies," Corrosion Science, Vol. 50, No.11, pp 2981–2992 (2008).

48. Zhou Z, Parr R G, "Activation hardness: new index for describing the orientation of electrophilic aromatic substitution," Journal of the American Chemical Society, Vol.112, No. 15, pp 5720-5724 (1990).

49. Sastri V S, Perumareddi J R, "Molecular orbital theoretical studies of some organic corrosion inhibitors," Corrosion (NACE), Vol. 53, No.8, pp 617-622 (1997).

50. Sahin M, Gece G, Karcı F, Bilgic S, "Experimental and theoretical study of the effect of some heterocyclic compounds on the corrosion of low carbon steel in 3.5% NaCl medium," Journal of Applied Electrochemistry, Vol. 38, No.6, pp 809-815 (2008).

51. Guo Gaoa, Chenghao Liang, "Electrochemical and DFT studies of β-amino-alcohols as corrosion inhibitors for brass," Electrochimica Acta, Vol. 52, No.13, pp 4554–4559 (2007).

52. Wen Chen, Hong Qun Luo, Nian Bing Li, "Inhibition effects of 2,5-dimercapto-1,3,4-thiadiazole on the corrosion of mild steel in sulphuric acid solution," Corrosion Science, Vol. 53, No.10, pp 3356–3365 (2011).

PAPER

I. SURFACE AND BULK WATER IN COLLOIDAL UNIMOLECULAR POLYMER (CUP) SYSTEMS INVESTIGATED BY SPIN-LATTICE (T_1) RELAXATION MEASUREMENTS

Yousef Dawib, Rex Gerald II, and Michael Van De Mark[*]

Department of Chemistry, Missouri University of Science and Technology

*Corresponding Author. mvandema@mst.edu

ABSTRACT

Water-based colloidal unimolecular polymers (CUP) have ultra-high surface areas per gram of particles. Many properties of the colloidal CUP system are dominated by the associated surface water. Proton spin-lattice relaxation (T_1) NMR experiments were conducted at low magnetic field (20 MHz, ^{1}H) over a temperature range of 18-37°C to examine the free and surface water populations in the system as a function of concentration, temperature, and two molecular weights (29kD and 111kD). Inversion recovery T_1 NMR data was analyzed using a model equation consisting of the sum of two mono-exponential terms and five adjustable parameters. The amount of bound water was found to be in the range of 2.7-8.1% of the total water in this system, and the bound water layer thickness ranged from 0.20 to 0.69 nm. The observed spin-lattice relaxation time constant T_1 varied with the CUP concentration; the T_1 value decreased as the CUP concentration increased. The spin-lattice relaxation time constant of the bound water (T_{1b}) was shorter than the relaxation time constant of the free water (T_{1f}) by a factor of approximately 50. Two intrinsic CUP parameters (particle size and the

charge density) were important in determining the amount of associated surface water. Smaller particles had more surface area per gram but the larger particles had a higher surface charge density. As the CUP concentration increased the thickness of the bound water layer decreased. This reduction of bound water layer thickness can be explained on the basis of Manning condensation.

Keywords Colloidal unimolecular polymer (CUP), Bound water, Bulk water, Proton spin-lattice NMR relaxation time constant (T_1), surface charge density, surface area, low field NMR.

INTRODUCTION

The term "bound water" in a macromolecular system has been used since 1922. Newton and Gortner [1] raised the hypothesis that a certain amount of water exists in close proximity to constituent particles in hydrophilic colloids; the water associated with a macromolecule surface is defined as bound water. Water molecules that exist freely in a solution are known as bulk water. In general, water molecules bond to the colloidal particle surface via hydrogen bonding [2]. In turn, bulk water molecules are not bounded to colloidal particle surface. These molecules are considered to move freely in solution media.

The bound water molecules have been found to possess properties that differ from water molecules located further from the surface. For example, bound water molecules exhibit a lower vapor pressure, a lower mobility, and a lower freezing point than water molecules located far away from the surface [3, 4].

Gortner [5] studied the state of water in both colloidal and living systems, suggesting that two states of water exist within lyophilic hydrosols and hydrogels: bulk water and bound water. He explained the nature of bound water by using two hypothesis: an oriented adsorption of the water dipoles at the interface, and an oriented adsorption of hydrogen and hydroxyl ions. Another model for waters interacting described by Zimmerman and Brittin [6] explains water behavior in view of the differences of ^{1}H NMR relaxation rates between adsorbed water and free water molecules. They concluded that both transverse and longitudinal relaxation data described two-phase systems. Nandi and Bagchi [4] [stated] that the bound water molecules are those molecules which have single or double hydrogen bonds with either a protein or a self-assembled aggregate.

Because the mobility of bound water molecules is lower than the mobility of free bulk molecules, the nuclear magnetic resonance (NMR) probing method has been used to gain a deep understanding about the state of water in colloidal systems. Clifford and Pethica carried out numerous studies regarding the use of relaxation rate measurements in determining water states in colloidal systems. In 1965 [7], they studied the spin lattice relaxation time constants of water protons in micelle solution. Results revealed that the hydrocarbon chain length influenced the rate of spin relaxation in water molecules in proximity to the chain. This effect was attributed to dipole-dipole interactions between the alkyl chain protons and water protons, and water molecules near alkyl chains exhibit slower rotational Brownian motion than the water molecule in the bulk. Also a linear relationship was observed between temperature and spin lattice relaxation rate. A

subsequent study [8] conducted on carboxylic acid soaps confirmed this finding, and concluded that hydrogen-bonded water molecules to the head group were immobile. Another study conducted by Clifford [9] used the spin-lattice relaxation time constant measurements of CH_2 protons in micelles in D_2O. They concluded that the spin relaxation rates of CH_2 protons were greatly increased as the environment changed from D_2O to liquid hydrocarbon. Clifford et al. [10] has also studied the behavior of a water-silica system. The study examined the spin lattice relaxation time constants as a function of hydroxyl group densities on two types of silica beads. Results indicated that the hydrogen bonding interaction between water molecules and the surface highly influenced the NMR relaxation time. The strongly hydrogen bonded molecules on the surface OH group exhibited slower motion. Clifford concluded that in the water-solid particle system, there are less than two monolayers of water physisorbed on the surfaces of the solids they studied [8, 10].

Clifford and Pethica et al. [11] attempted to confirm the existence of bound water on colloid particles. They prepared polyvinyl acetate (PVA) in the form of monodisperse solutions consisting of spherical particles with varying size less than 1μm. A direct measurement of relaxation times (T_1 and T_2) of 0.13μm and 0.8μm diameter particle, were used. Results indicated that the relaxation rates ($1/T_1$ and $1/T_2$) increased linearly up to a certain concentration. Above this concentration a rapid increase of relaxation rates were noticed. The authors explained this change in view of *a* co-operative effect. As the particle approached each other, the cooperative effect became dominant. The study concluded that

the total amount of bound water per unit surface area was greater for the larger

particle [8, 11].

Katayama and Fujiwara [12] investigated the states of water in a

polyacrylamide gel by means of spin-lattice relaxation time constant (T_1)

measurements. Their study concluded that the macromolecule must have a

hydrophilic substituent such as R–OH, -CO$_2$H, R-CO, R-CHO, R-CONH$_2$, R-NH,

to be able to capture a certain amount of water. They stated that the nature of a

substituent plays an important role in determining the amount of bound water.

Another study [13] supported this finding, as the authors studied the effect of a

substituent type of cellulose ethers on both the state and the dynamics of water

in hydrogels. The water proton spin-lattice (T_1) and the spin-spin (T_2) relaxation

time constants were measured to probe polymer/water interaction at room

temperature. The results indicated that the T_1 and T_2 values of water in hydrogels

decreases as polymer concentration increases. The number of bound water

molecules is also highly dependent on the substituent type. The presence of

hydrophilic substituents on polymer chains produces a high bound water fraction.

Moreover, the relaxation rate (1/T_1) is sensitive to the type of polymer substituent

but insensitive to the molecular mass of the polymer.

The spin-lattice (T_1) and the spin-spin (T_2) relaxation times were utilized to

study water behavior in poly (methylmethacrylate) hydrocolloids [14]. Results

revealed that the relaxation rate (either 1/T_1 or 1/T_2) increased as the amount of

polymer increased. The translational diffusion coefficient of water molecules in

hydrocolloids decreased as the polymer concentration increased. This decrease

may be attributed to a restriction of motion of water molecules located on the polymer's surface. Thus, the relaxation rate was found to be directly proportional to the bound water fraction.

Duff [15] examined the temperature and frequency dependence of spin-lattice relaxation time constants in a porcine L dorsi muscle. Spin-lattice (T_1) relaxation time constants were recorded at 10.7, 30, 60, and 90 MHz over a temperature range 203-263°C. Duff found that the bound water fraction decreased from 0.15 at 263°C to 0.07 at 203°C.

Nystrom et al. [16] conducted ^{1}H NMR experiments at 99.6 MHz over a temperature range of 14-44°C to study the motion of small molecules in cellulous gels. They also examined the temperature dependency of spin-lattice time constant (T_1) and diffusion coefficient (D). Their results demonstrated that the presence of a polymer reduced the values of T_1 and D to the same degree. Over the temperature range, the ratio of T_1 in gel to T_1 in solvent remained constant.

Blinc et al. [17] measured the T_1/T_2 ratio of fibrin gels, plasma, and blood clots to determine the bound water fraction, in addition to the temperature effect on T_1 and T_2. Both the T_1 and the T_2 values decreased as the temperature decreased from 40°C to below 0°C. The bound water fraction in the fibrin gel at room temperature was approximately 3×10^{-3}, whereas, in the collapsed fibrin gel the bound water fraction was 10^{-2}. Blinc et al. [18] further investigated the dependence of water self-diffusion coefficients, the proton spin-lattice, and spin-spin relaxation rates on the concentration of gelatin and collagen. In a gelatin water system, the water behavior was explained with a two-phase exchange

model. The spin-lattice and the spin-spin relaxation rates (1/T_1 and 1/T_2, respectively) varied linearly with the bound water fraction. The spin-lattice relaxation rate of bound water was equal to 24.7 sec^{-1}. The spin-spin relaxation rate of bound water was equal to 206 sec^{-1}. In turn, in the collagen water system, the spin-lattice relaxation time constant was analogous to the water-gelatin system. However, the spin-spin relaxation profile exhibited a non-exponential decay and displayed two T_2 values. The third water component that exists in the collagen-water system was defined as the structural water that stabilizes collagen's helical structure.

A ^{1}H NMR relaxometry study [19] examined water adsorbed on colloidal latex particles in polyelectrolyte solution. It was found that the water relaxation rate increased as the concentration increased. This increase was due to the increase of bound water fraction attached to polymer chains. The linear relationship between the water relaxation rate and the polymer concentration was only observed at a low concentration whereas, at a high concentration, deviation from linearity occurred. They attribute this deviation to structural changes in the polymer solution.

In summary, the following trends were observed for spin relaxation phenomenon in water-containing systems; the spin lattice relaxation time is proportional to the temperature and varied linearly with bound fraction. Also, the spin-lattice relaxation time constants for protons in bound water (T_{1b}) is shorter than the spin-lattice relaxation time constants for protons in free water molecules (T_{1f}). The amount of bound water in water-colloid systems is very small, and

substituent on the surface play an important role in determining bound water layer thickness.

Colloidal Unimolecular Polymer

Colloidal unimolecular polymer (CUP) system is a new colloid system that exists as solid spheroid particles suspended in an aqueous media. A CUP particle has charged groups located on the sphere's surface, in conjunction with a collapsed hydrophobic backbone chain [20]. The hydrophilic groups can be anionic, cationic, or non-charged analogues to a micelles (see Figure 1).
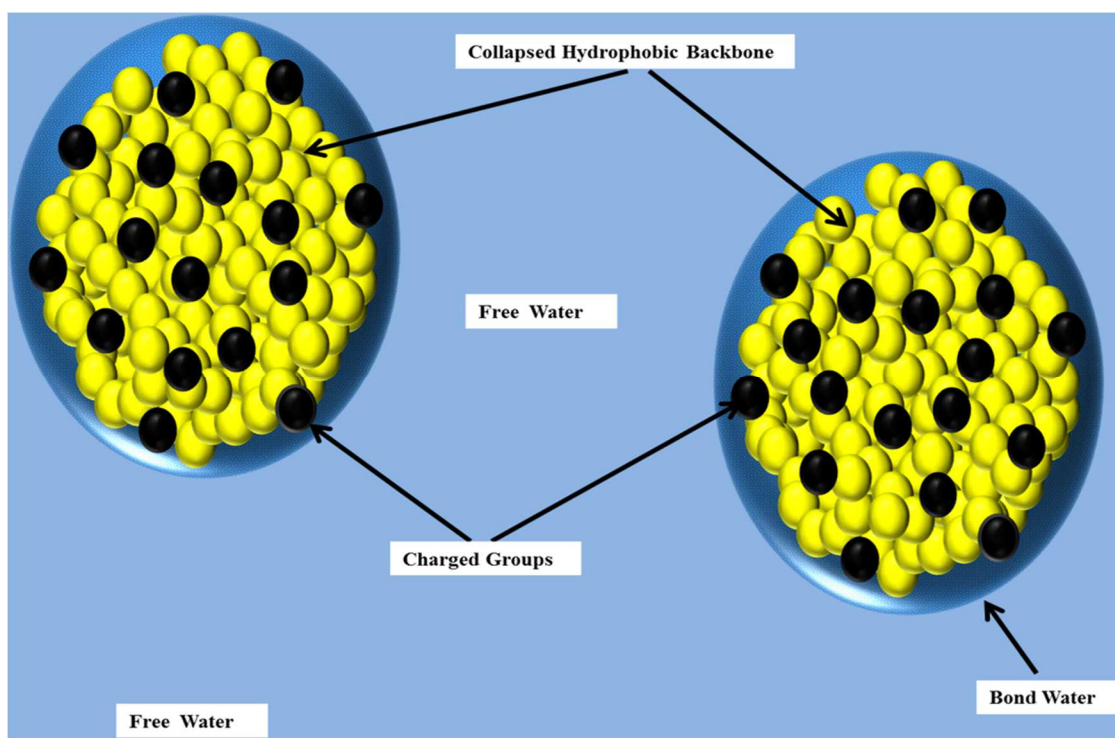
Fig. 1 Colloidal Unimolecular Particles System.

Figure 2 shows the steps in the process of forming a CUP particle in a solution. The formation of CUP particles is simply accomplished in view of the Flory-Huggins theory. A specific amount of a copolymer (MMA-MAA) is dissolved

in an organic solvent. In this step the polymer chains are in random coil configuration (structure I). Based on the acid number value, the acid groups were neutralized by base. Neutralizing the acid groups creates a charge repulsion, thus the random coil configuration becomes extended (structure II). Water of pH 8-9 was added to the solution to change solvent environment. The water addition raises the dielectric constant of polymer solution, so charge repulsion increases. In order to minimize the charge repulsion, the polymer chain changes its configuration to be an extended chain (structure III) at which point the Mark–Houwink parameter (a) attains its highest value approaching 2. By continuously adding water to the polymer solution, the polymer solution reaches the point at which the polymer-polymer interaction became greater than the polymer-solvent interaction. Hence, water released from the backbone entropically favors the polymer chain collapse (structure IV). Finally, the organic solvent was stripped off leaving only solid spheroid particles suspended in aqueous media (structure V) at which point the Mark–Houwink parameter (a) approaches zero. The presence of an ionic group on the surface is the driving force for preventing particle aggregation, and aids in the formation of the spheroidal shape. CUP suspensions can be considered as a unique colloidal system, they have typical particle sizes of 2 to 9 nm based on the molecular weight of the copolymer. Moreover, CUP systems contain only charged particles, water, and counterions without any additives.
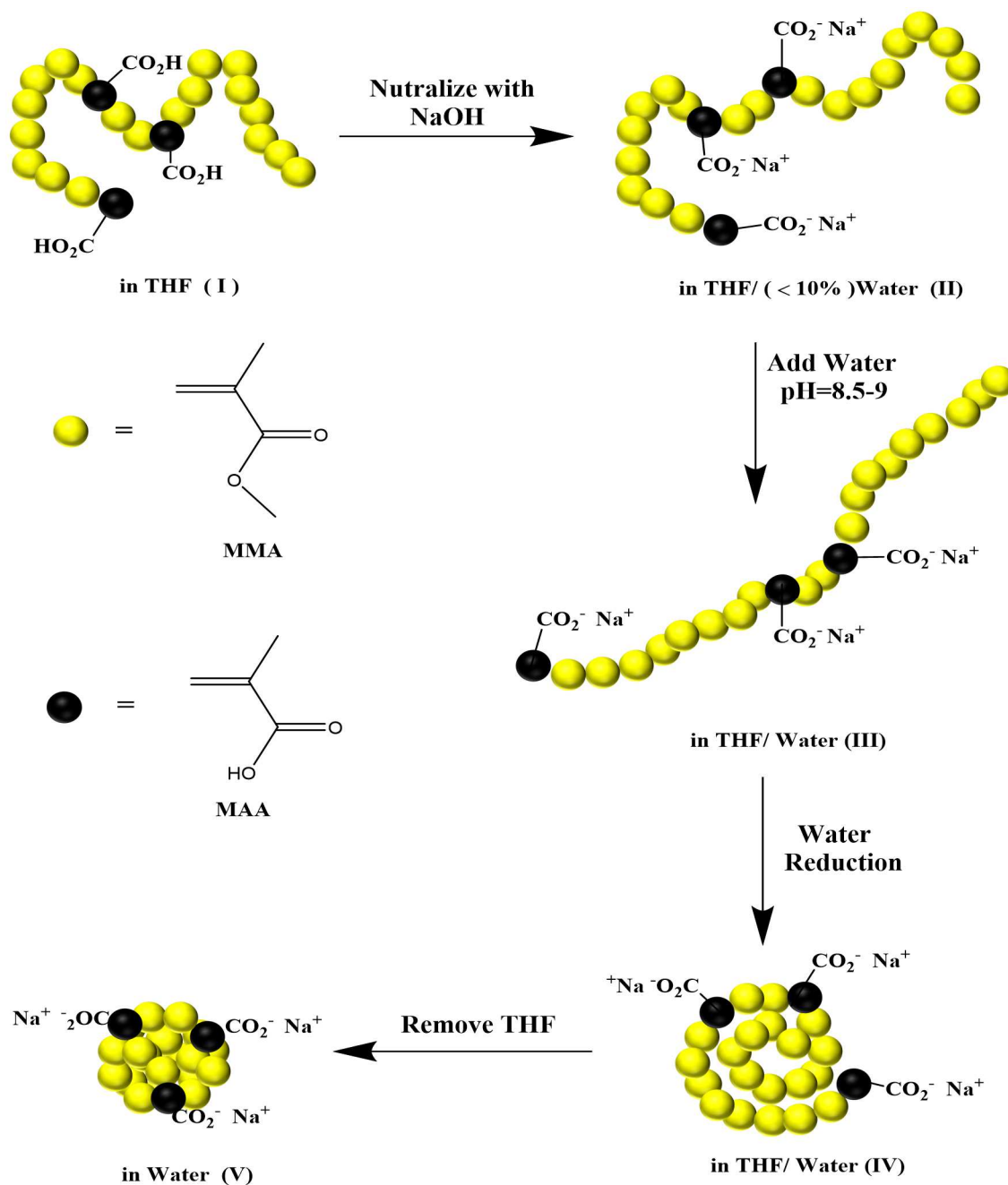
Fig. 2 Process of forming CUP particles

The rheological properties of CUP particles in water suspension was studied by Van De Mark et. al. [21]. Results showed that the rheology behavior of CUP particles is highly influenced by primary and tertiary electrovisocus effects in dilute solutions. The surface water layer thickness increased as the

particle size increased due to the increase of surface charge density. In addition, a study on the gel point and rheology measurements of a CUP system was conducted [22]. A capillary viscometer and a cone-and-plate rheometer were used to measure viscosities. Results indicated that the thickness and the density of surface water around the CUP particles play an important role in determining the gel point. CUP suspension intrinsic viscosity values were found to be analogous to spherical polyelectrolytes. This suggested that CUP particles are behaving as highly charged spheroid particles. Calculations based on the random close packing assumption and the density of bound water and free water revealed that the bound water layer thickness was 0.57 nm. Also, a dynamic surface tension study [23] using a maximum bubble pressure surface tensiometer indicated the existence of bound water in a cationic CUP system, and found that the density of bound water was 1.6% larger than the density of bulk water.

This study investigated the bound water in CUP systems experimentally by means of low field ^{1}H NMR. Proton NMR spin-lattice relaxation time constants were measured for CUP colloidal systems as a function of CUP particle size, concentration, and temperature.

EXPERIMENTAL

Materials

Chemicals used; Methyl methacrylate (MMA), methacrylic acid (MAA), 2, 2′-azobis (2-methylpropionitrile) (AIBN), and 1-dodecanethiol were purchased from Aldrich. MMA was washed with a 10% (w/w) solution of sodium bicarbonate, and then deionized water and brine solution. This solution was dried over sodium sulfate and filtered. Finally, the solution was distilled under nitrogen gas. MAA was purified by distillation. AIBN was re-crystallized from methanol, and 1-dodecanethiol was used as received.

Synthesis and Characterization of Poly (MMA/MAA) Copolymers

The two copolymers of MMA and MAA under investigation were prepared in a molar ratio of 9:1 by a free radical polymerization method. To a stirred 2L three neck flask were added (750g) of tetrahydrofuran (THF), methyl methacrylate MMA (225.25g, 2.25mol), and methacrylic acid MAA(21.5g, 0.25 mol). A chain transfer agent 1-dodecanethiol was added. The amount of chain transfer agent was calculated based on the desired molecular weight of the polymer (2.15g for 25kD and 1.2g for 111kD). The initiator AIBN 0.3g was then added. The reaction mixture was heated to reflux for 24 hours under nitrogen gas. The solution was then allowed to cool to room temperature and precipitated in cold de-ionized water under high shear mixing. Finally, the polymer was placed in a 50°C oven under vacuum for 24 hours. The absolute molecular weight of the copolymers was measured using gel permeation chromatography using a Viscotek model 305 instrument manufactured by Malvern Corp. Flow rate of THF

was 0.5ml/min, and the injection volume was 100µl. The GPC was equipped with a refractive index detector, low and right angle light scattering detector, and intrinsic viscosity detector, thus yielding absolute molecular weight. Table 1 shows the parameters that characterized the two synthesized polymers.

Table 1 Molecular weight, particle size, and acid number of copolymers

Polymer MMA-MAA	Mn	Particle Size (nm)		Acid value	Acid groups per chain	Acid groups per nm² *
		Calculated	DLS			
RX25	29 kD	4.2	4.1	59.1	~29	0.55
RX22	111 kD	6.6	6.5	62.2	~112	0.85

*Charge density on CUP surface.

Acid Number

Acid numbers were determined by titration method in accordance with ASTM D-974. This standard was slightly modified by using potassium hydrogen phthalate (KHP) in lieu of hydrochloric acid and phenolphthalein in place of methyl orange.

Water Reduction

Ten grams of synthesized polymer was dissolved in 40g tetrahydrofuran (THF) (20% w/w) and stirred overnight. Based on the value of the acid number, 1M sodium hydroxide solution was added to neutralize all the acid groups. Then 80 g of modified water (pH=8~9 adjusted by 1 M NaOH) was added to the polymer solution by a peristaltic pump at a rate of 1.24g/minute. It is important to maintain the pH of the solution between 8.3 and 9.0. THF was then stripped in-

vacuo and filtered through a 0.45μm Millipore membrane to remove any foreign materials. For higher concentrations, the water was removed under reduced pressure. Once all the CUP solutions of various concentrations were prepared, one gram of each solution was transferred into 10mm-diameter flat bottom NMR tubes, and sealed with a plastic cap.

Particle Size Analysis

The particle size of CUP was measured by Microtrac Nanotrac 250 with a dynamic light scattering method (DLS). Also an average theoretical diameter of CUP particles was calculated from the absolute molecular weight (Mn) measured by GPC. The purpose of using two techniques is to compare and confirm the results.

The proton spin-lattice relaxation time constants were measured using a Bruker MiniSpec 20-MHz NMR magnet interfaced to a Unity Varian spectrometer. A series of 30 spin-lattice relaxation recovery spectra were observed by using a standard inversion recovery **180˚- τ -90˚** pulse sequence. All experiments were performed without field-frequency locking at 18˚, 27˚, and 37˚C; field stabilization was achieved through thermal stabilization of the magnet. The temperature was controlled by placing the Bruker magnet in Fisher isotherm incubator. The accuracy of temperature control was ± 0.2˚C. Each measurement was repeated five times on different days to confirm its reproducibility. All data reported in this paper are average values.

RESULTS AND DISCUSSION

The solid unreduced sample of poly (MMA/MAA) copolymers RX-25-29kD was initially measured by low field proton NMR in order to determine its signal contribution to the results. We were unable to detect any significant signal, therefore, the polymer's contribution to the NMR signal was neglected. Proton NMR spin-lattice relaxation time constants, T_1, for the water solvent were measured as a function of CUP concentration at three different temperatures. Initially, the data was analyzed using a mono-exponential recovery model. Figures 3 and 4 show the plot of T_1 vs CUP concentration for various temperatures. T_1 indeed varied inversely with CUP concentration; as the CUP concentration increases, the T_1 values decrease. This behavior strongly suggested a two-phase model because a different contribution from each phase results in lowering T_1 values, and that the data should be analyzed on the basis of a bi-exponential recovery model. The spin lattice relaxation time constant can therefore characterize the proton relaxation for at least two different proton environments. Our data suggested that the measured T_1 value obtained from a mono-exponential analysis represented the weighted average value of the spin-lattice relaxation time constants for protons in bound water (T_{1b}) and in free water molecules (T_{1f}). The decrease in T_1 value with increasing CUP concentration seen in Figures 3 and 4 indicated a progressive increase of the shorter T_{1b} contribution. The relationship between the bound and free water fraction can be re-expressed using a bi-exponential model expressed in equation (1). The bound water molecules have lower molecular mobility than bulk water, and as reported

in the literature [13, 18], the nuclear magnetic relaxation time constant, T_{1b}, is much shorter than the proton spin relaxation parameter for free water, T_{1f}.

$$\frac{1}{T_1} = \frac{\phi}{T_{1b}} + \frac{1 - \phi}{T_{1f}} \qquad (1)$$

Where, ϕ is the fraction of bound water molecules, and is given by

$$\phi = \frac{N_b}{N_b + N_f} \qquad (2)$$

Here, N_b is the number of bound water molecules, and N_f the number of free water molecules.
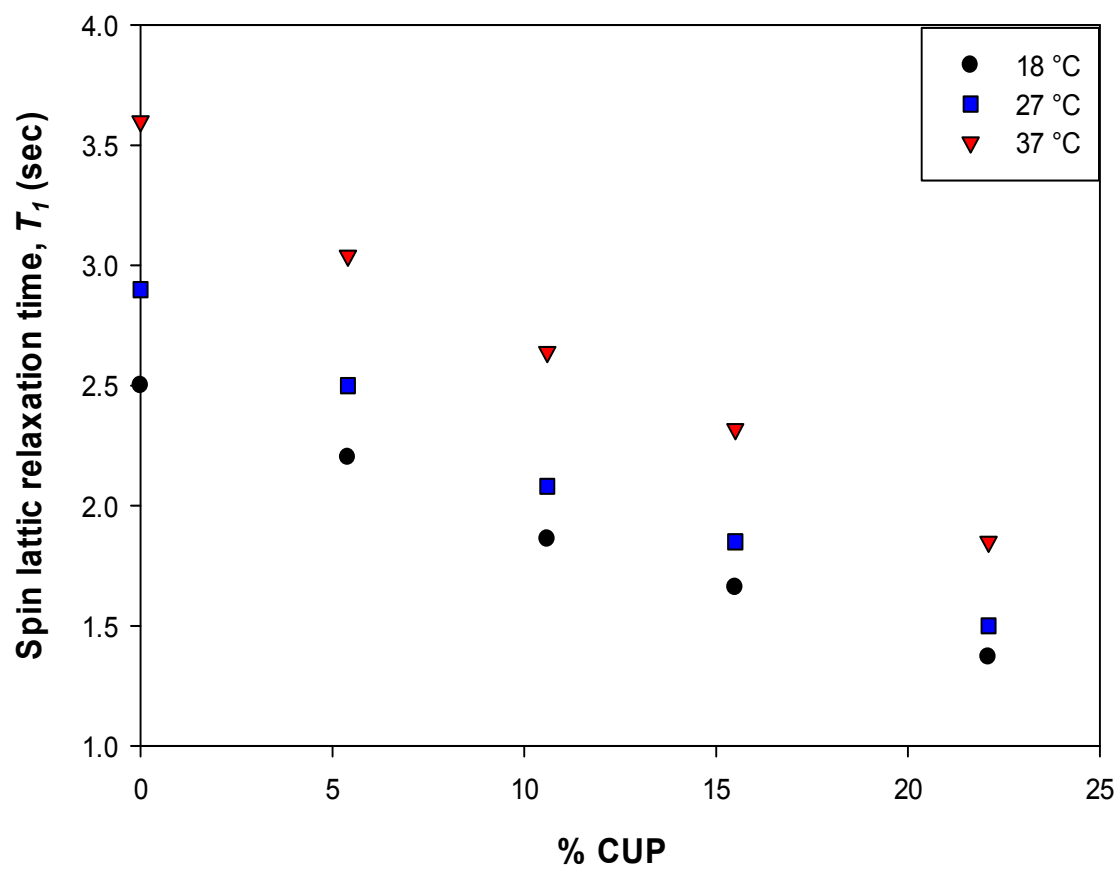
Fig. 3 Water proton NMR spin-lattice relaxation time (T_1) of RX25- 29kD as a function of CUP concentration.
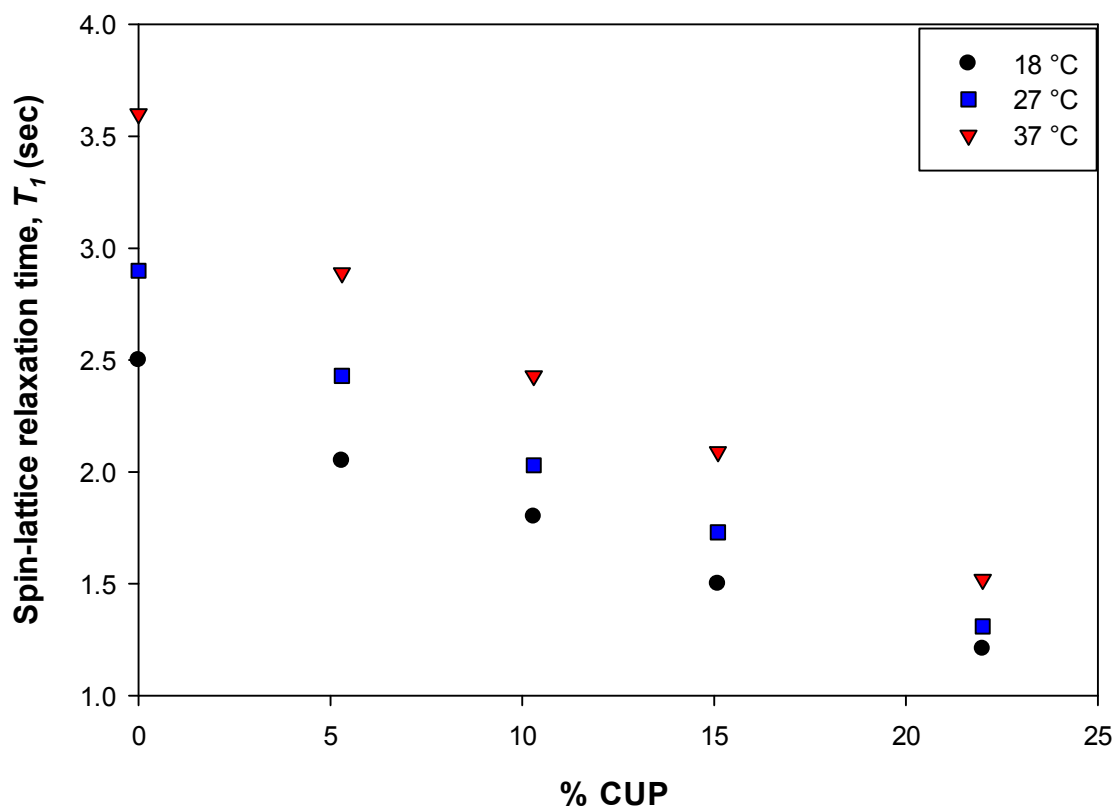
Fig. 4 Water proton NMR spin-lattice relaxation time (T_1) of RX22-111kD as a function of CUP concentration.

Even though the NMR measurements were conducted on similar concentrations of both polymers, the spin lattice relaxation time constants, T_1, for solutions of RX22-111kD were smaller than T_1 values of RX25-29kD (see Figure 5). The difference became more pronounced as the CUP concentration increased. This change was interpreted in terms of the fact that the RX22-111kD had greater surface charge density per unit area than RX25-29kD. Therefore, the RX22-111K particles associated a larger amount of bound water than RX25-29K particles.
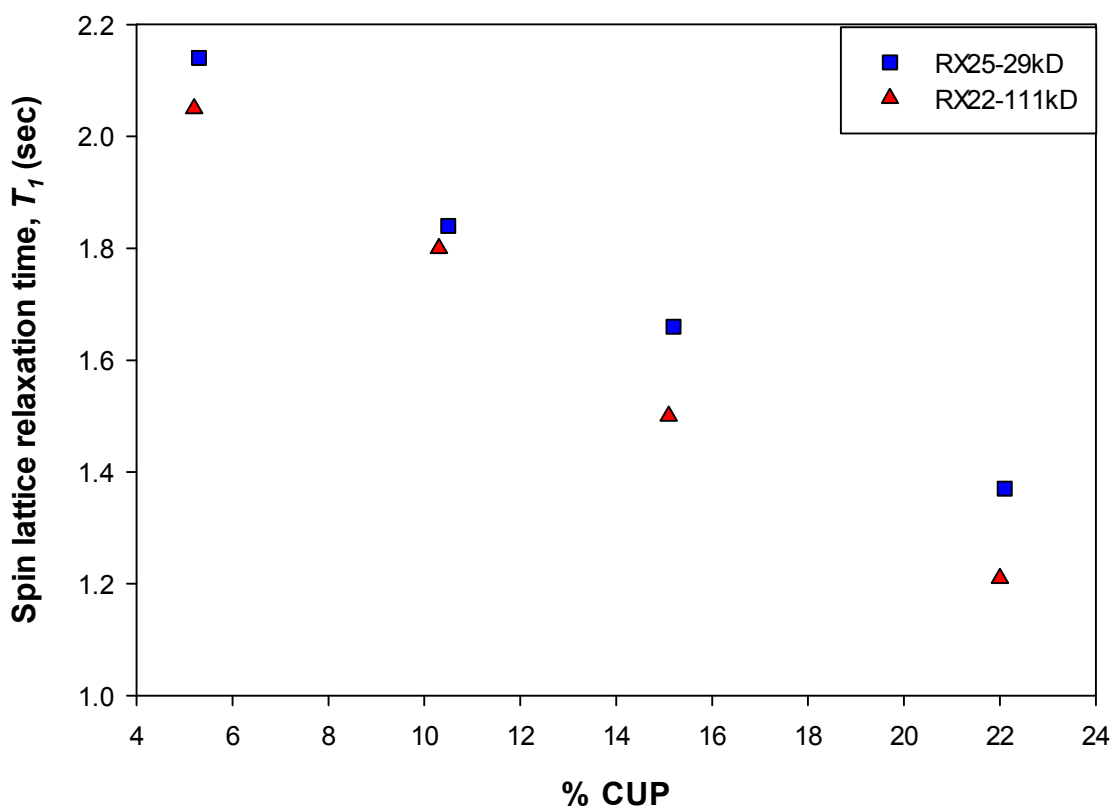
Fig. 5 Water proton NMR spin-lattice relaxation time (T_1) of both polymers at 18° C as a function of CUP concentration.

Figure 6 and 7 show the variation of the spin-lattice relaxation time constant T_1 over the temperature range 291-310 K. We interpreted the experimental results where the T_1 values increased with temperature to be due to the increase in the rate of molecular motion of the waters. The relationship between T_1 and 1/T for pure water was linear, but it deviated slightly from linearity for CUP solutions. The deviation is probably due to the existence of two types of waters (free and bound). The temperature has a direct influence on the

diffusion coefficient, D, of bulk water molecules. According to the Stokes-Einstein equation, the diffusion coefficient, D, is given by:

$$D = \frac{kT}{6\pi\eta r}$$ (3)

Where k is Boltzmann constant, T is absolute temperature, η is viscosity of the solvent (water,) and r is radius of the diffusing solute particle. The diffusion coefficient of water molecules is proportional to the temperature and inversely proportional to the viscosity of water. Viscosity measurements of CUP solutions [21] found that the CUP solution viscosity increased as CUP volume fraction increased. Subsequently, the diffusion constant decreased. The proton spin-lattice relaxation time constant, T_1, has also been related to the diffusion coefficient, viscosity, and temperature by the following relationship [24]:

$$T_1 \alpha\ D\ \alpha\ \frac{T}{\eta} \alpha\ \exp\left(\frac{-E}{RT}\right)$$

Where E is the activation energy, R is gas constant. Proton spin-lattice relaxation time constant (T_1) measurements of CUP-water systems agreed with the above relationship. The T_1 values increased as the temperature increased due to the increase in the diffusion coefficient of water molecules. As the concentration of cup particles increased, it was likely that the electroviscous effect caused an increased deviation from linearity in the plots.
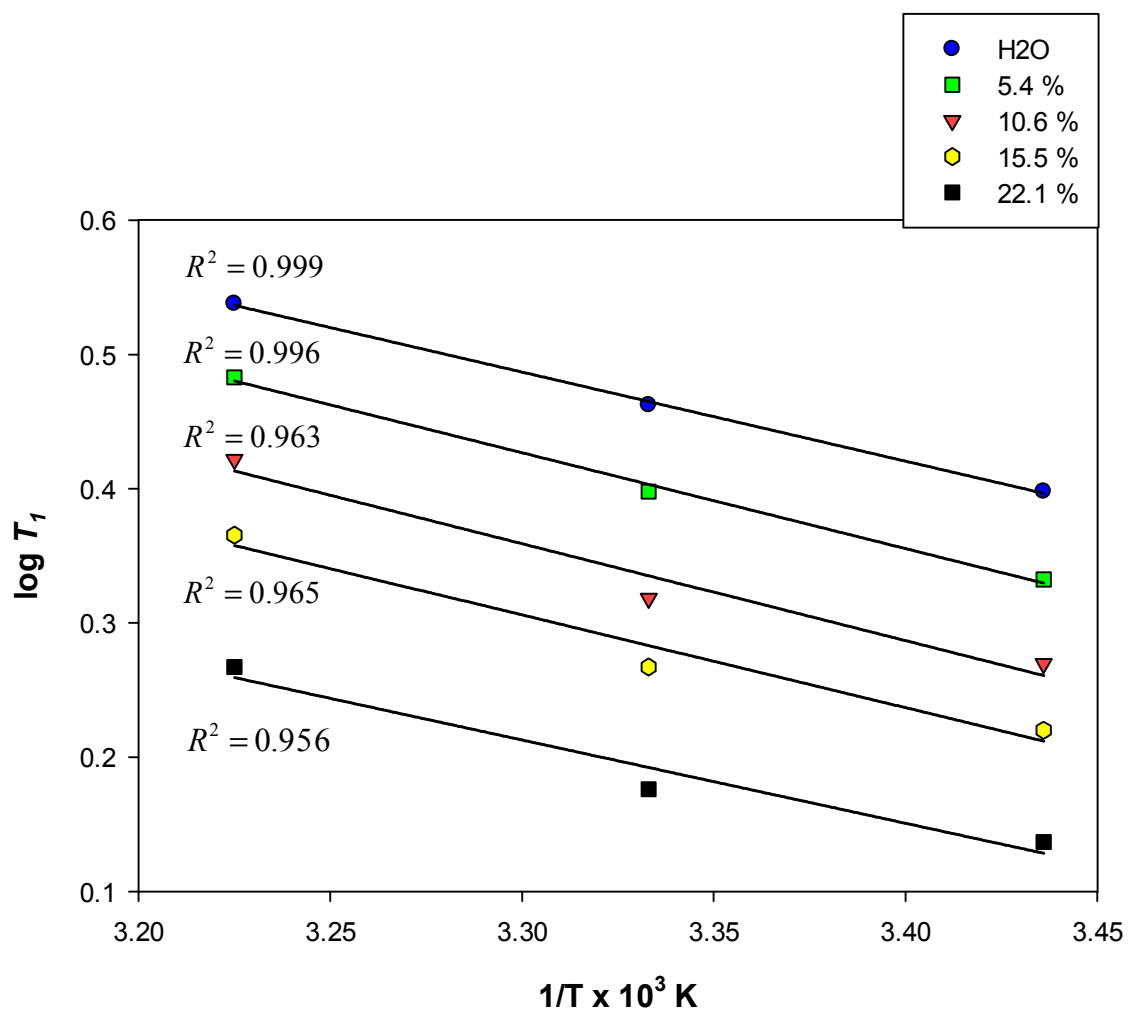
Fig. 6 Temperature dependence of the proton spin-lattice relaxation time of RX25-29kD.

48
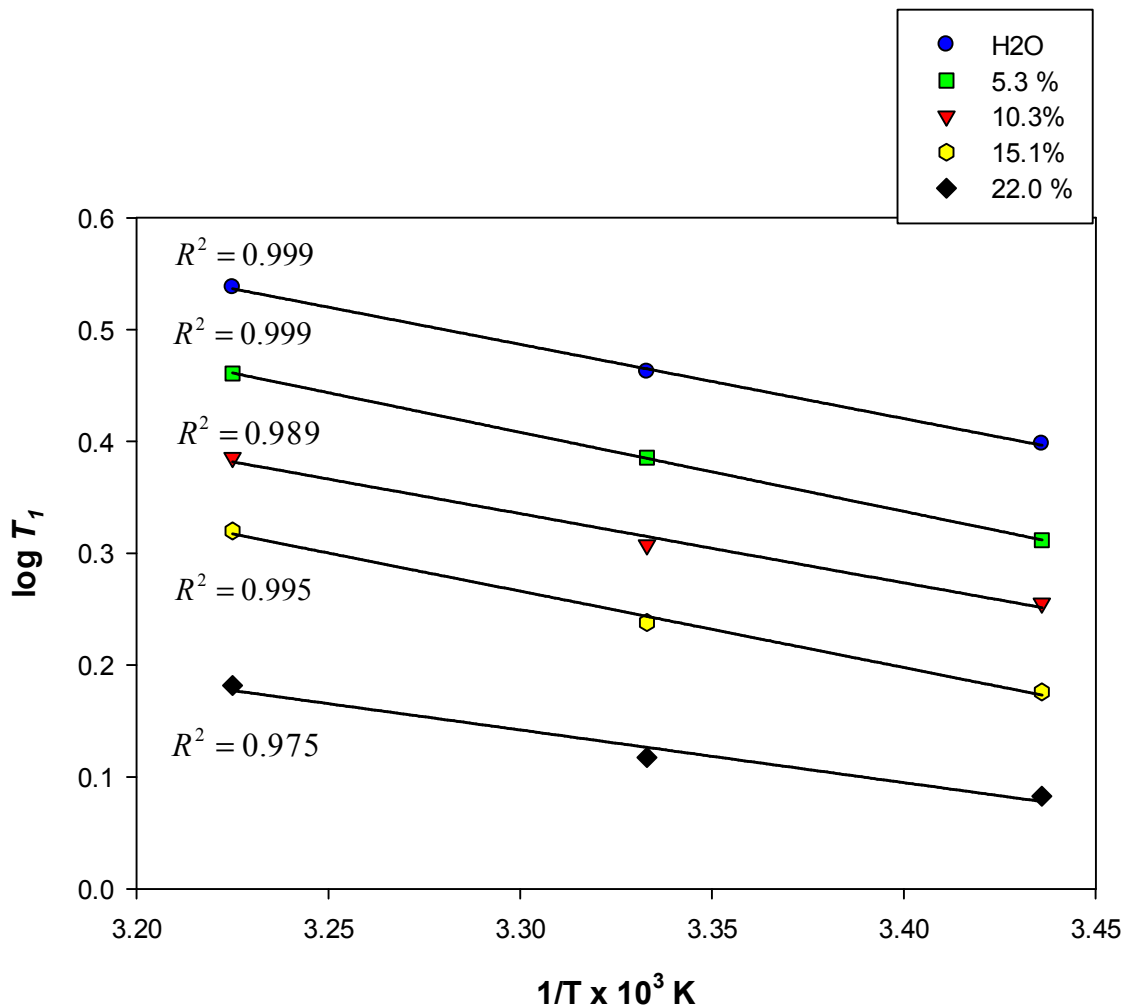
Fig. 7 Temperature dependence of the proton spin-lattice relaxation time of RX22-111kD.

In order to calculate the amount of bound and free water in the CUP system as well as T_{1b} and T_{1f}, the proton spin inversion recovery data was analyzed by a model equation consisting of the sum of two exponential terms, including five fit parameters (a model that describes a two-site system):

$$F(t) = \sum_{i=1}^{n} A_i (1 - 2 \exp^{-t/T_{1i}})$$

(4)

Where, A_1 = amount of bound water; A_2 = amount of free water, T_{11} = relaxation time constant for bound water, and T_{12} = relaxation time constant for free water. This mathematical construct was effectively used to quantify content and microscopic distribution of oil in shale samples [25]. Data analysis was performed by SigmaPlot version 12.5 software. Results are presented in Figures 8 and 9.
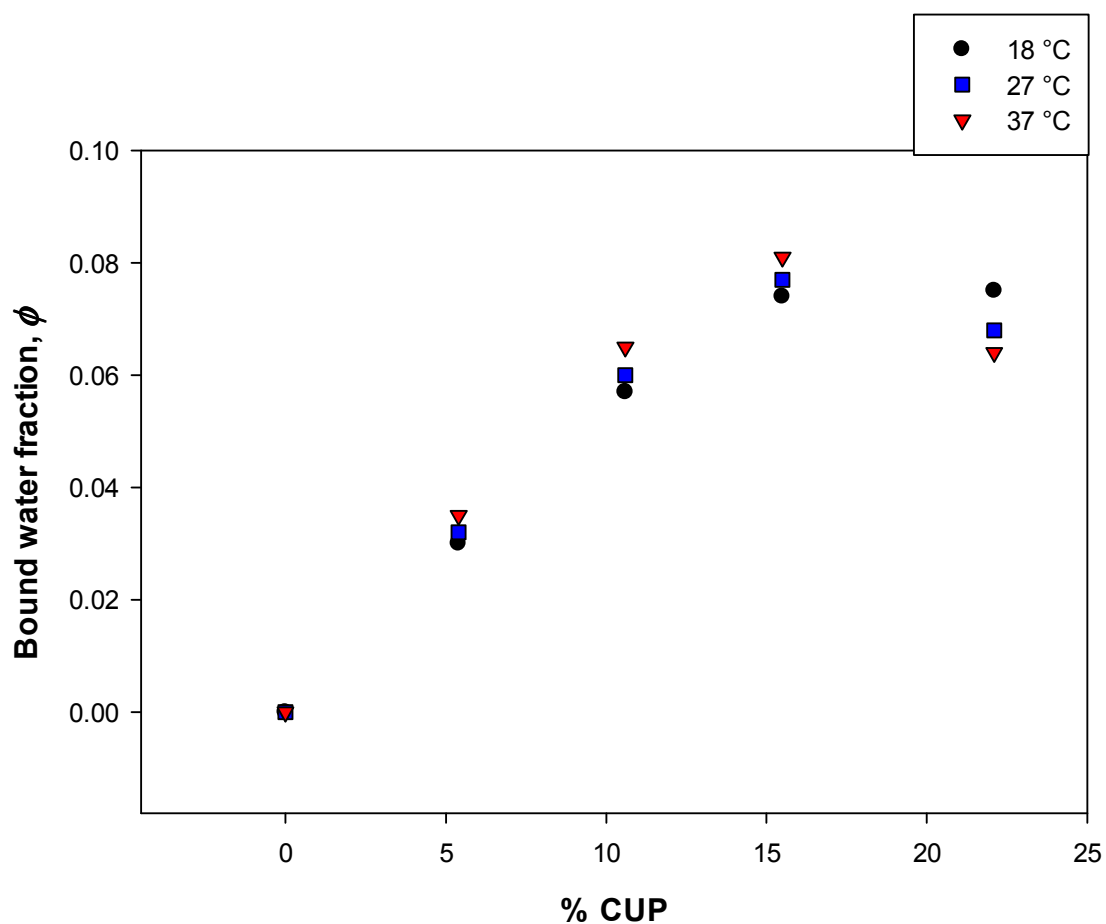
Fig. 8 Bound water fraction of RX25-29kD as a function of CUP concentration.
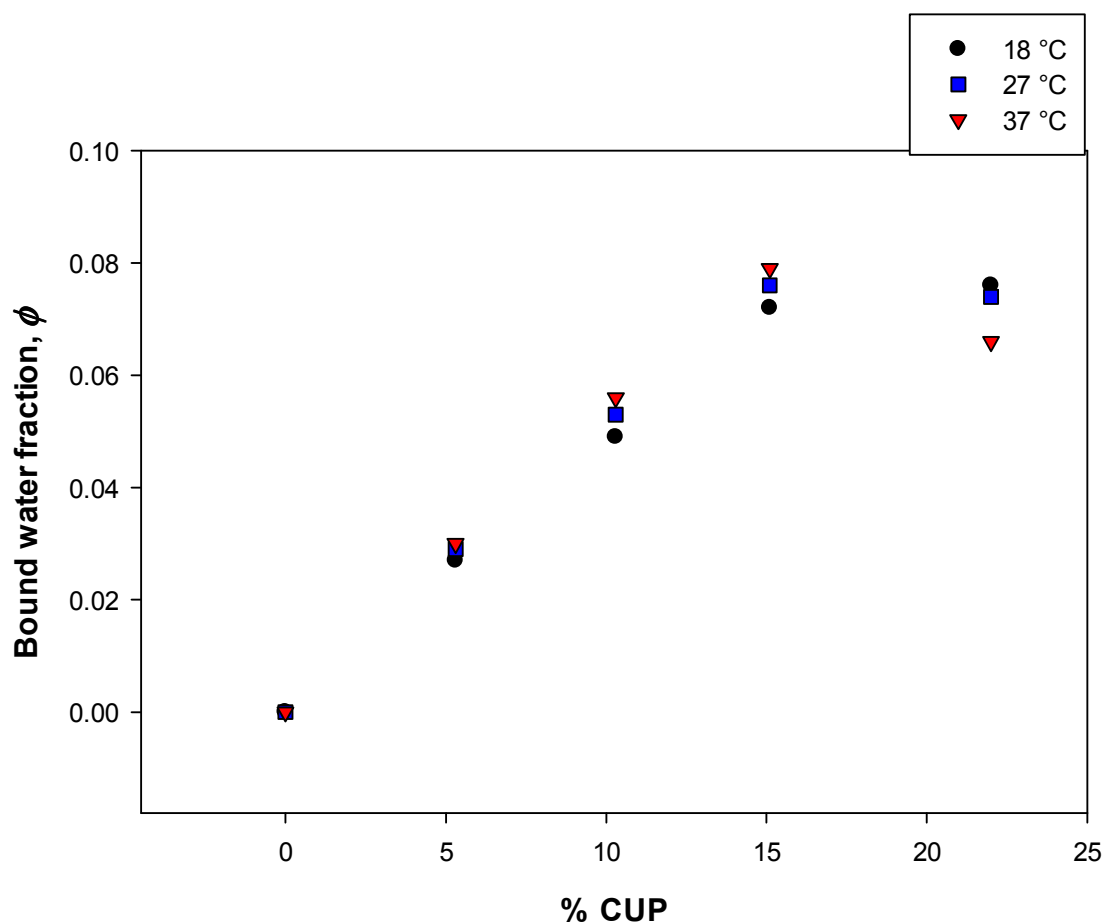
Fig. 9 Bound water fraction of RX22-111kD as a function of CUP concentration.

It can be seen from Figures 8 and 9 that the bound water fraction ϕ varies almost linearly with CUP concentration up to 15%. At higher CUP concentrations, the data deviated from linearity. The reason for the deviation is a surface charge density effect. The CUP particle is a charged spheroid particle with negative charges on their surface due to the carboxylate groups. According to the Manning counterion condensation model [26], the surface charge causes a counterion condensation. There are two type of condensation; short range and long range condensation. The short range counterion condensation results from neighboring charge repulsion located on the same particle whereas the long

range counterion condensation results from charge repulsion between two particles. The long range counterion condensation is more pronounced at high concentrations. Calculation of surface charge density on CUP particles has been performed [21] using the Belloni program. Results indicated that the effective charge decreased as the CUP volume fraction increased.   The higher the molecular weight, the greater effective charge number. The increase in CUP concentration led to an increase in counter ion concentration. This results in the accumulation of these ions on the CUP surface causing the electric double layer to be shortened, hence a reduction in the bound water layer thickness.

To gain a deeper understanding of CUP hydration, it is important to relate our results to a microscopic model of the CUP system by calculation of the bound water layer thickness.   The weight of bound water was calculated from the following formula:

$$\phi = \frac{m_{bound}}{100 - m_{cup}} \tag{5}$$

Where m_{bound} is the weight of bound water, m_{cup} is the weight of CUP, (the total weight of CUP solution was 100 g). To get the total volume of bound water, the weight of bound water was divided by the density of bound water, which is equal to 1.0688 g/cm^3 [22].The total surface area of the CUP particles was calculated based on the measured diameter of a single CUP spheroid. Then, the water layer thickness was calculated by dividing the total volume of bound water by the total surface area of the CUP particles.

Table 2 Bound water layer thickness for various concentrations of two CUP systems at the indicated temperatures.

Concentration	RX25-29kD			RX22-111kD		
	Bound water layer thickness in nm			Bound water layer thickness in nm		
	18˚ C	**27˚C**	**37˚C**	**18˚ C**	**27˚C**	**37˚C**
~ 5%	0.45	0.48	0.52	0.63	0.67	0.69
~10%	0.41	0.43	0.46	0.56	0.60	0.63
~15%	0.34	0.36	0.39	0.52	0.55	0.57
~ 22%	0.23	0.21	0.19	0.53	0.33	0.30

Table 2 shows that the bound water layer thickness was larger for RX22-111kD than RX25-29kD. The typical diameter of a hydrogen bonded water molecule used in our calculations was 0.27-0.28 nm. At low concentrations of CUP, the RX22-111kD particle holds approximately 2.3 bound water layers whereas the RX25-29kD particle hold about 1.7 bound water layers. The acid groups on CUP particles surface have a propensity to bond with water molecules via hydrogen bonding. The RX22-111kD has more carboxylate groups per unit area than RX25-29kD, Table 1. Accordingly, the surface charge density of RX22-111kD is higher than RX25-29kD [21]. Higher surface charge density requires more hydrated sodium ions at the CUP surface which cause the bound water layer to be thicker. These results agreed with the rheology study [22] that indicated the existence of two bound water layers hydrating the CUP particle,

and the higher surface charge density holding more water molecules. As the concentration of CUP increased the number of counterions increased (see Figure 10). The electrostatic coupling between negatively charged CUP particles and positively charged sodium ions causes counterions condensation on the CUP surface. This charge accumulation reduces the effective charge density [21]. For this reason, the bound water layer thickness decreases as the concentration of CUP increases above 15%.
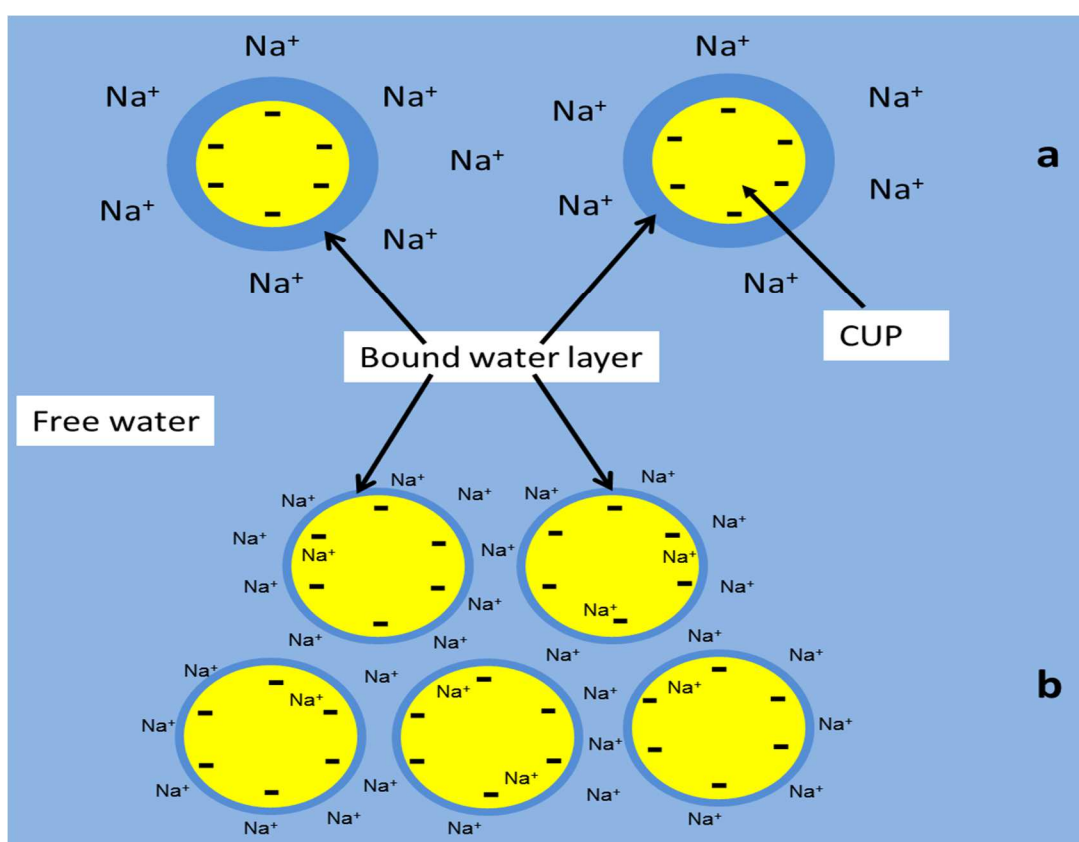
Fig. 10 The effect of CUP concentration on bound water layer thickness: (**a**) Dilute solution CUP particles are far from each other and counterion concentration is low. (**b**) Concentrated solution CUP particles approach each other and counterions condense, reducing the size of the thickness of bound water layer.

We observed that there was an insignificant increase in bound water fraction as the temperature was increased. This may be explained in terms of increasing molecular mobility. Some water molecules are too tightly bound and may go "dark" and can not be detected by T_1 analysis. As the temperature rises, these water molecules become slightly mobile and captured by T_1 measurements.

From the analysis of the inversion recovery NMR data, we found that the bound water relaxation time T_{1b} does not change as the CUP concentration increased and as the particle size increased. This suggested that the interaction between CUP particle and water molecules take place via only one regime. The most probable mechanism is through hydrogen bonding interaction. The value of T_{1b} =42 ± 3 ms. This value is similar to the bound water relaxation time that was previously reported in a gelatin-water system (T_{1b} = 40.5 ms) [18], and cellulose ether polymer-water system (T_{1b}= 57.1 ms) [13].

CONCLUSION

In CUP-water systems, there are generally two states of water; free and bound water. One to two water layers directly hydrated the CUP particle surface. The hydration of CUP particles was found to be strongly dependent on surface charge density of the CUP particle, the higher the surface charge density, the thicker the bound water layer. However, as the concentration of CUP particles increased, the bound water layer thickness decreases as a result of Manning condensation. The bound water layer thickness is not significantly affected by

temperature at low concentration, but it significantly changed at high concentration ~ 22% over temperature range 18-37°C.

ACKNOWLEDGMENTS

REFERENCES

1. Newton R, Gortner R A (1922) A method for estimating hydrophilic colloid content of expressed plant tissue fluids. Bot. Gaz. 74:442–446

2. Watano, Satoru, Powder Technology Handbook (3rd Edition) (2006), 265-267

3. Cooke R, Kuntz D (1974) Properties of water in biological systems. Annual Review of biophysics and bioengineering.3: 95-126

4. Nandi N, Bagchi B (1997) Dielectric Relaxation of Biological Water. Journal of Physical Chemistry. B 101(50):10954-10961

5. Gortner RA (1930) The state of water in colloidal and living systems. Transactions of the Faraday Society 26:678-704

6. Zimmermann JR, Brittin WE (1957) Nuclear magnetic resonance studies in multiple phase systems: lifetime of a water molecule in an adsorbing phase on silica gel. Journal of Physical Chemistry 61:1328-33

7. Clifford J, Pethica B (1965) Properties of micellar solutions. III. Spin lattice relaxation times of water protons in solutions of sodium alkyl sulfates. Transactions of the Faraday Society 61(1): 182-9

8. Clifford J, Pethica B (1968) Hydrogen bonding in aqueous colloid systems. Hydrogen-Bonded Solvent Systems, Proc. Symp.:169-179

9. Clifford J (1965) Properties of micellar solutions. IV. Separation lattice relaxation times of hydrocarbon chain protons in solutions of sodium alkyl sulfates. Transactions of the Faraday Society 61(6): 1276-82

10. Clifford J, Lecchini S (1967) State of liquid water near solid interfaces. SCI Monograph 25:174-95

11. Johnson GA, Lecchini S, Smith E G, Clifford J, Pethica B A(1966) Role of water structure in the interpretation of colloid stability. Discussions of the Faraday Society 42: 120-33

12. Katayama S, Fujiwara S (1979) NMR study of the spatial effect of polyacrylamide gel upon the water molecules confined in it. Journal of the American Chemical Society 101(16):4485-8

13. Saša Baumgartner, Gojmir Lahajnar, Ana Sepe, and Julijana Kristl (2002) Investigation of the state and dynamics of water in hydrogels of cellulose ethers by ^{1}H NMR spectroscopy. AAPS PharmSciTech 3 (4) article 36 1-8

14. Kristl J, Lahajnar G, Jezernik K, Smid-Korbar J(1992) Water behavior in poly(methyl methacrylate) hydrocolloids studied by NMR techniques and electron microscopy. S.T.P. Pharma Sciences 2(3): 265-9

15. Duff I D, Derbyshire W (1974) NMR investigation of frozen porcine muscle. Journal of Magnetic Resonance 15(2):310-16

16. Nystroem B, Moseley M E, Brown W, Roots J (1981) Molecular motion of small molecules in cellulose gels studied by NMR. Journal of Applied Polymer Science 26(10): 3385-93

17. Blinc A, Lahajnar G, Blinc R, Zidansek A, Sepe A (1990) Proton NMR study of the state of water in fibrin gels, plasma, and blood clots. Magnetic Resonance in Medicine 14(1): 105-22

18. Blinc R, Rutar V, Zupancic I, Zidansek A, Lahajnar G, Slak J(1995) Applied Magnetic Resonance 9(2): 193-216

19. Schwarz B, Schonhoff M (2002) A 1H NMR relaxation study of hydration water in polyelectrolyte mono and multilayers adsorbed to colloidal particles. Colloids and Surfaces, A: Physicochemical and Engineering Aspects 198-200, 293-304.

20. Riddles C J, Zhoa W, Hu HJ, Van De Mark M R (2011) Colloid unimolecular polymers (CUPs) synthesized by random copolymerization of MMA/MAA. Polymer Preprints 52(2):232-233

21. Chen M, Riddles C J, Van De Mark M R (2013) Electroviscous Contribution to the Rheology of Colloidal Unimolecular Polymer (CUP) Particles in Water. Langmuir 29(46): 14034-14043

22. Chen M, Riddles C J, Van De Mark M R (2013) Gel point behavior of colloidal unimolecular polymer (CUP) particles. Colloid and Polymer Science 291(12):2893-2901

23. Natu A, Wiggins M, Van De Mark M R (2015) Synthesis and characterization of cationic colloidal unimolecular polymer (CUP) particles. Colloid and Polymer Science 293(4): 1191-1204

24. Simpson J H, Carr H Y (1958) Diffusion and nuclear spin relaxation in water. Physical Review 111: 1201-2

25. Rex G E II, Chi L, Zhang H, Woelk K (2011) Low-field NMR spin-lattice relaxation time-constant distributions of shale. 46th Midwest and 39th Great Lakes Regional Meeting of the American Chemical Society, 19-22 MWGL-16.

26. Manning G S (1975) A limiting law for the conductance of the rod model of a salt-free polyelectrolyte solution. Journal of Physical Chemistry 79(3): 262-5

II. PROBING POLYMER CHAIN DYNAMICS BY ^{13}C SOLID-STATE NMR USING CP-TOSS

Yousef Dawib, Rex E. Gerald II, Cynthia J. Riddles, and Michael Van De Mark

Missouri University of Science and Technology

*Corresponding Author. mvandema@mst.edu

ABSTRACT

A method for the detection of detailed polymer mobility was developed using solid state NMR. Solid-state ^{13}C NMR spectra were obtained for a commercial homopolymer and an acrylic copolymer using magic angle spinning with proton cross polarization and the pulse sequence for total spinning sideband suppression, CPMAS-TOSS. The observed peak intensities of the backbone carbons and side chain carbons were monitored as a function of temperature. As the temperature increased, the peak intensities decreased because a concomitant increase in polymer mobility disrupted proton cross polarization, a requirement for the enhancement and observation of ^{13}C NMR peaks. The decays in peak intensities in solid-state ^{13}C CP-TOSS NMR spectra were related to specific polymer chains dynamics. The plot of peak intensity vs. temperature for a well-resolved peak revealed two intersecting lines. Several intersection point temperatures were found to be close to the temperatures of the first deviations from the extrapolated baselines measured by differential scanning calorimetry (DSC). The NMR method allows distinguishing between the onsets temperatures for mobility of the main chain versus the side chains. As expected,

the carbons in the rigid backbone displayed higher intersection point temperatures than the side chain carbons.

Keywords: polymer mobility, solid-state NMR, cross-polarization, ^{13}C CP-TOSS NMR, chain dynamics, intersection point temperature, DSC, Tg

1. INTRODUCTION

In the field of spectroscopy, generally, nuclear magnetic resonance spectroscopy (NMR) is the most useful tool for identification of polymer molecular architecture. Liquid state proton and ^{13}C NMR dominate utilization capacity for structure identification. For determining molecular dynamics, proton NMR has a limitation unless, for example, deuterium isotope substitution is performed [1, 2].

Differential scanning calorimetry (DSC) is commonly used to measure the glass transition temperature (Tg) of polymers. The Tg is commonly understood as the temperature at which a polymer changes from a glassy state to a rubbery state. The DSC technique relies on the measurement of endo and exo heat flow to/from the sample when subjected to a programmed linear temperature change [3, 4]. As the sample temperature is raised or lowered, there is absorption or release of energy [5]. The TG measured by DSC represents a temperature range, rather than a specific temperature [6]. The midpoint of the range of temperatures over which the molecule shows an increase in heat flow is generally reported as the glass transition temperature (TG).

Solid state ^{13}C NMR has been used routinely to investigate the chemical structure of organic molecules. The growth of usage of solid state NMR can be

attributed to several advantages over liquid state NMR such as an absence of solvent effects and sample solubility limitations. Also, the instrumentation developments of the technique were able to remove the effects of chemical shift anisotropies and dipolar interactions, hence narrow spectra were produced. This improvement has made solid state NMR an attractive method for also characterizing molecular dynamics [7, 8].

There are many ^{13}C solid state NMR experiments employed to gather information about structure and chain conformation characteristics [1]. Cross polarization (CP) combined with magic angle spinning (MAS) is the most common solid-state NMR experiment (CP-MAS). In the CPMAS experiment, the sample is rapidly spun around the rotor axis which is placed at the magic angle (54.74°) with respect to the external applied magnetic field, B_o. Then, cross polarization is employed in order to enhance the signal to noise ratio of the ^{13}C signal by transferring ^{1}H polarization to ^{13}C [7]. The ^{1}H spins interact with the ^{13}C nuclear spins according to the dipolar interaction [8]. This interaction occurs through space and depends on the gyromagnetic ratio of both nuclei and the distance between them [7, 8]. The dipolar coupling constant R quantifies the magnitude of the dipolar interaction and is equal to:

$$R_{CH} = \frac{\mu_O \gamma_H \gamma_C \hbar}{4\pi \left\langle r_{CH}^3 \right\rangle} \tag{1}$$

Where μ_o is the permeability constant of free space, γ_H and γ_C are the gyromagnetic ratio of hydrogen and carbon, respectively, $\hbar$ is the reduced Planck constant, and r_{CH} is the distance between carbon and hydrogen spins. As the distance between a carbon-proton spin pair increases the dipolar coupling constant decreases, and a concomitant decrease in the polarization transfer effect results in weaker ^{13}C NMR signals. For instance, the R_{CH} value is equal to 22.54 kHz when the distance between the carbon and hydrogen is 1.1 Å, the typical hydrogen-carbon bond length. This value drops to 3.75 kHz as the distance increases to 2Å, the typical distance between a carbon and hydrogen located on an adjacent carbon. A large R_{CH} value results in a large enhancement of the carbon signal intensity for relatively short CP contact times. It turns out that the larger the R_{CH} value, the shorter CP time is required to transfer polarization. Since polarization fades away back to equilibrium, it is best to transfer polarization from protons to carbon as quickly as possible. Large R_{CH} values make it possible to transfer polarization quickly and thereby maximize the enhancement of ^{13}C NMR signals. Therefore, enhanced CP efficiency will be greatly dependent on carbon-proton distances in a polymer. The CP signal will be much weaker for carbons that are not bonded directly to protons [7, 8]. Another factor that determines the value of the energy of interaction between proton and ^{13}C spins is the angle between the external field and the vector joining the two spins. The energy of interaction is equal to:

$$E = \frac{A}{r^3}(1 - 3\cos^2\theta)$$

<div align="right">(2)</div>

Where r is the distance between the two spins and θ is the angle between the external field and the vector joining the two spins. The constant A depends on the magnetic moment of the two spins. The greater the energy of interaction between a proton-^{13}C spin pair the more efficient and effective the polarization transfer, and the more intense the ^{13}C NMR peak.

The CP-MAS techniques have been widely used to characterize organic and polymer structures. Schaefer and coworkers [9] pioneered the application of this technique. They were able to obtain well-resolved ^{13}C NMR spectra for solid poly(methyl methacrylate) and solid polystyrene samples at room temperature. Later, this technique was used to probe the group dynamics of polymer chains [10, 11]. Schaefer [10] found that the ^{13}C rotating frame relaxation time constant ($T_{1\rho}$) was directly related to motions of main chains in glassy polymers. He stated that for glassy polymers, the ^{13}C ($T_{1\rho}$), is sensitive to motions of the polymers having frequencies comparable to the magnitude in kHz of the applied carbon rf field.

CP-MAS experiments have been carried out as a function of temperature [12, 13]. The combination of variable temperature and CP-MAS added advantages to solid-state NMR. CP-MAS combined with variable temperature makes it possible to investigate both molecular structure and molecular dynamics [12, 13]. Variable temperature CP-MAS experiments were used to provide

information about the amorphous and crystalline state of cured diglycidyl ether of bisphenol A (DGEBA) polymers [13]. The study correlated the solid-state line splitting and line shape to the state of the polymer.

The ^{13}C NMR peak widths for polymers as a function of temperature have been investigated [15, 16]. A study on the effect of solid bisphenol A polycarbonate (BPAPC) molecular motion on NMR line width was performed [2]. Results indicated that the broadening and narrowing of ^{13}C NMR spectra was greatly dependent on temperature. McGrath [15] studied segmental dynamics of polyisobutylene (PIB) and poly (vinylethylene) (PVE). His results confirmed that there was a direct connection between ^{13}C NMR spectra line width and molecular motion [15]. Linewidth measurements from variable temperature ^{13}C CP-MAS spectra were also employed in order to distinguish between crystalline and amorphous states. Lyeria [7] found that the ^{13}C chemical shift may vary due to a variation in intermolecular effects from one molecule to another in the sample.

One of the unique aspects of the CP-MAS experiment is the possibility to perform relaxometry measurements. Spin-lattice relaxation time constants (T_1), spin-spin relaxation time constants (T_2), and proton and carbon rotating-frame relaxation time constants ($T_{1\rho}$) can be determined. The analyses of these parameters over a temperature range provide information about the molecular motion. Schaefer and Stejskal [9] have carried out $T_{1\rho}$ measurements to probe dynamic heterogeneity of the glassy state by conducting a variable temperature study on polypropylene (PP) and polymethyl methacrylate (PMMA). They observed a progressive broadening of the methyl resonance as the temperature

decreased. This broadening was attributed to the reorientation rate of the methyl group. As for the $T_{1\rho}$ data for the quaternary carbonyl and methoxy carbons, the methyl motion had an influence of relaxing other carbons in solids via long-range C-H dipolar interactions [7, 9].

In 1982, Dixon and co-workers [16, 17] developed a CP-TOSS technique, cross polarization with total suppression of spinning sidebands. It was stated that this technique can eliminate spinning sidebands from CP-MAS spectra. In the TOSS technique, the pulse sequence consists of a series of four to six (equally – spaced) 180° pulses applied on the ^{13}C channel just before data acquisition [18]. This will suppress rotational echoes and allow the acquisition of the free induction decay signals without modulations from spinning.

In this study we applied the CP-TOSS pulse sequence to measure the segmental dynamics of poly(isobutyl methacrylate) and copolymer poly (methyl methacrylate/ butyl acrylate/ trifluoroethyl methacrylate/ acrylic acid), poly (MMA/BA/TFEMA/AA). We introduce a simple approach that correlates the decay of the peak intensities with temperature to Tg measured by DSC.

2. EXPERIMENTAL

2.1. Materials

Chemical used; methyl methacrylate (MMA), butyl acrylate (BA), acrylic acid (AA), 2,2,2-trifluoroethyl methacrylate (TFEMA), 2,2′-azobis(2-methylpropionitrile) (AIBN), and 1-dodecanethiol were purchased from Aldrich.

MMA and TFEMA were washed with a 10% (w/w) solution of sodium bicarbonate, and then washed with de-ionized water and brine solution. The solution was then dried over sodium sulfate and filtered. Copper (I) bromide was added to the MMA, and TFEMA as an inhibitor. Finally, the solutions were distilled under nitrogen gas. Acrylic acid (AA) was purified by distillation with copper (I) bromide. AIBN was re-crystallized from methanol, and 1-dodecanethiol was used as received.

2.2 Polymer Synthesis and Characterization

The homopolymer poly(isobutyl methacrylate) was purchased from Aldrich. The copolymer under investigation was synthesized by a free radical polymerization method. To a three-neck flask, 750 grams of methyl ethyl ketone (MEK) and a magnetic stirring bar were added. Then, methyl methacrylate MMA 75.68 g (0.76 Moles), BA 37.90 g (0.30 Mole), AA 8.72 g (0.12 Moles) and TFEMA 6.50 g (0.04 Moles) were added, giving a molar ratio of 19:7.5:3:1 MMA: BA: AA: TFEMA. A chain transfer agent, 1-dodecanethiol (0.81g, 4 mmol) was added. Finally, the initiator AIBN (0.14g, 0.8 mmol) was added. The reaction mixture was slowly heated to reflux for 24 hours under nitrogen gas. The solution was then allowed to cool to room temperature, and the white solid polymer precipitated in cold de-ionized water under high-shear mixing. Finally, the polymer was placed in a 50°C oven under vacuum for 24 hours. The absolute molecular weight of both the homopolymer and copolymers were measured using a Viscotek model 305 gel permeation chromatography (GPC) instrument manufactured by Malvern Corp. Flow rate of THF was 0.5ml/min, and the

injection volume was 100µl. The GPC was equipped with a refractive index detector, low and right angle light scattering detector, and intrinsic viscosity detector, thus yielding absolute molecular weight. Table 1 includes molecular weight values of both polymers.

Table 1 Homopolymer and copolymer molecular weight

Polymer	Mn
Poly(isobutyl methacrylate)	80 kD
poly(MMA/BA/TFEMA/AA), RX19	26 kD

2.3 Glass Transition Temperature Measurements

Glass transition temperature (Tg) of both commercial and synthesized polymers were obtained on a DSC Q2000 from TA Instruments- Waters LLC. Measurements were conducted in accordance with ASTM standard E1356-08. The modulated DSC (MDSC) method was applied by heating samples of mass 5-20 mg in premium aluminum hermetic pans DSC# 84010 & 84011from DSC Consumables, Inc. at a heating rate of 10 °C /min over the temperature range of 0°C to 100°C. The modulated amplitude was ±1°C with a period of 60 s. The typical heat flow thermograms for poly(isobutyl methacrylate) and fluorinated polymer RX-19 are illustrated in Figures 1 and 2. The temperature of first deviation (the point of first detectable deviation from the extrapolated baseline prior to the transition) and the midpoint temperature (the point on the thermal curve corresponding to 1⁄2 the heat flow difference between the extrapolated

onset and extrapolated end) were determined. The first deviation temperature of poly (isobutyl methacrylate) occurred approximately at 48°C (321K) whereas the midpoint temperature, the glass transition temperature, Tg, was 59°C (332K). The synthesized polymer RX-19 revealed a greater Tg value, 70°C (343K), and the first deviation temperature occurred approximately at 55°C (328K).
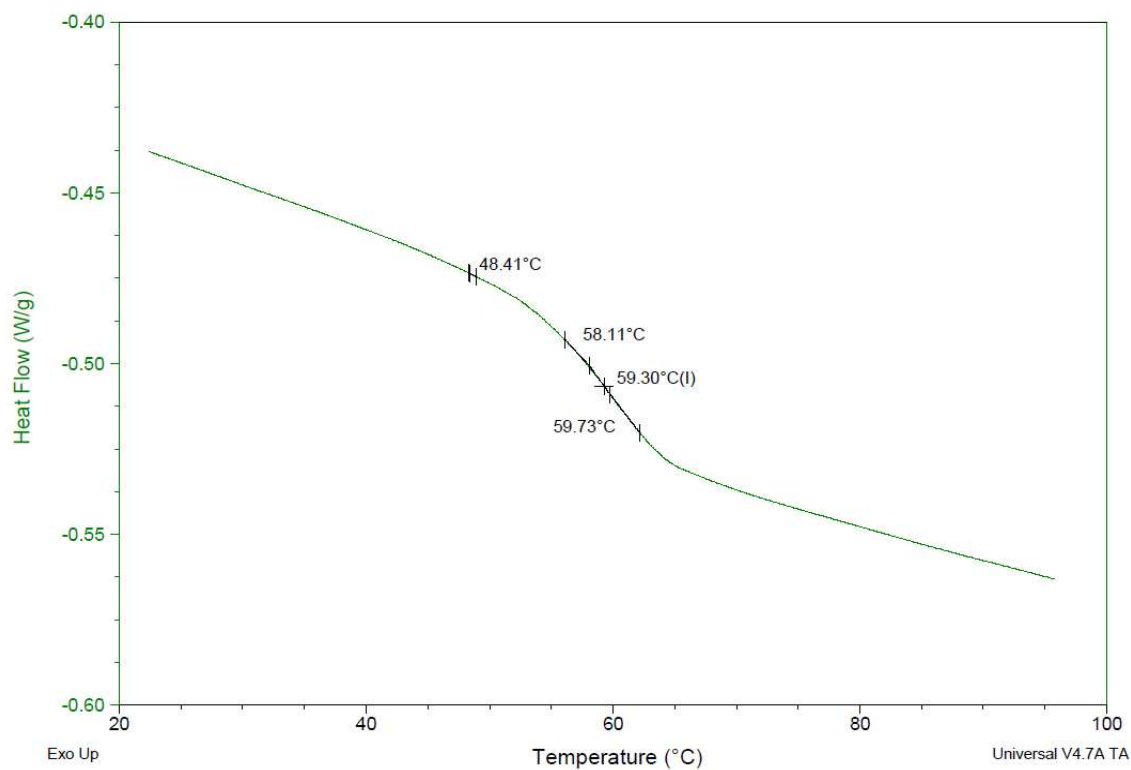
Figure 1. DSC thermogram obtained for poly(isobutyl methacrylate).
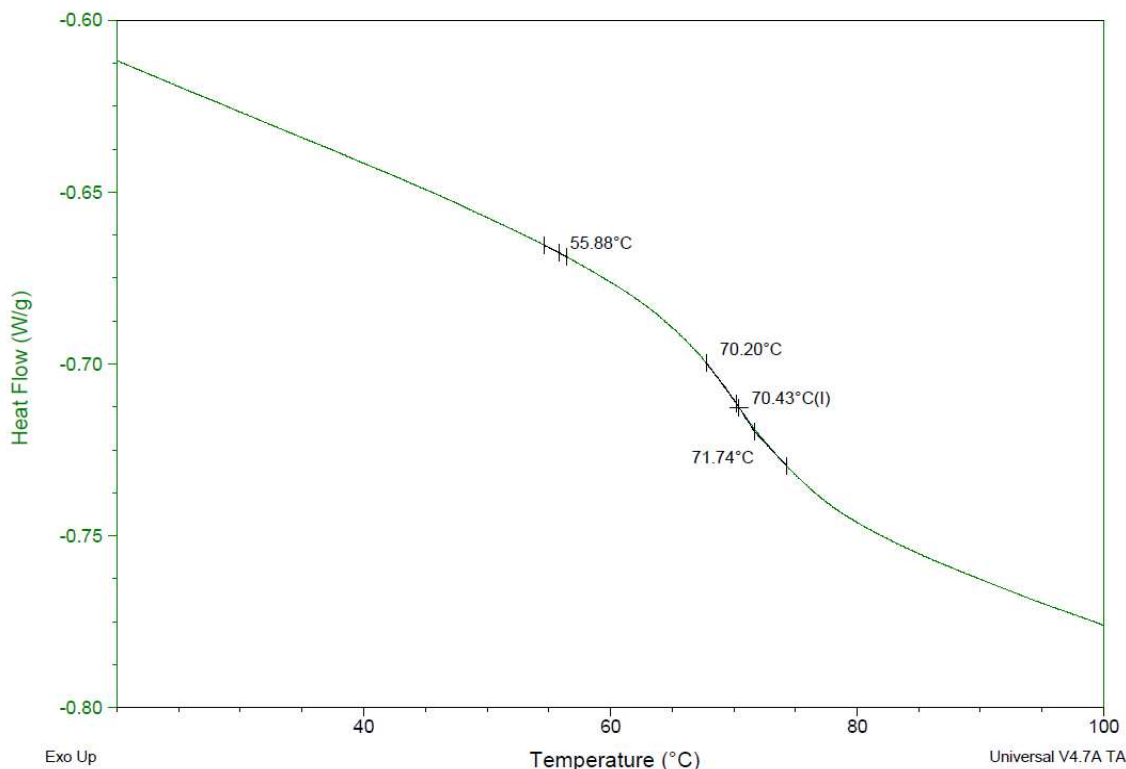
Figure 2. DSC thermogram obtained for copolymer RX-19.

2.4 Solid State NMR Measurements

All solid-state ^{13}C NMR spectra were obtained, from samples crushed into fine powders using a mortar and pestle, on a Bruker AVANCE III 400 Solid-State Spectrometer using magic angle spinning (5 kHz) with broadband proton decoupling and the CPMAS-TOSS pulse sequence for total spinning sideband suppression. The measurements were carried out over the temperature range 260-370K. After collecting data at a specific temperature, the sample and probe were allowed to reach thermal equilibrium over a period of ten minutes at the new specified temperature. NMR data was processed and analyzed using Bruker TopSpin version 3.2.1 software.

3. RESULTS AND DISCUSSION

3.1 Commercial Polymer poly(Isobutyl methacrylate)

The polymer backbone of poly(isobutyl methacrylate) contains a quaternary carbon and methylene carbon. The side chain consists of pendant carbonyl carbon, ($-OCH_2-$), ($-CH-$), and methyl carbons. The chemical structure of poly(isobutyl methacrylate) is shown in Figure 3.to discussion
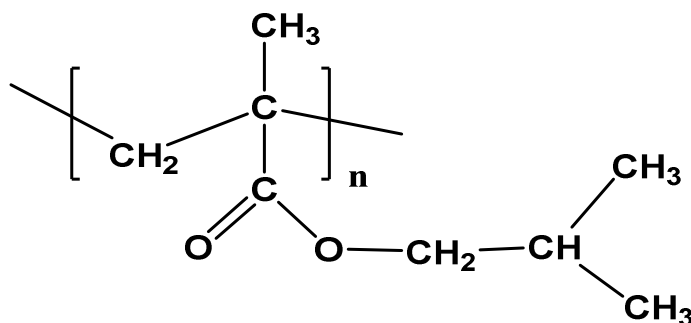
Figure 3. The chemical structure of poly(isobutyl methacrylate).

The peak at 170 ppm in the carbon NMR spectrum was assigned to the pendant carbonyl carbon, and peaks at 65, 22, and 13 ppm arose from ($-OCH_2-$), ($-CH-$), and ($-CH_3$), respectively. There are two types of methyl carbon: methyl carbon bonded to quaternary backbone carbon, and methyl carbon located far away from the backbone. The overlapping of peaks was obvious for both carbons. The quaternary backbone carbon resonance appeared at 38 ppm, and adjacent methylene backbone carbon resonance appeared at 49 ppm. Figure 4 shows the decay of peak intensities for different temperatures. At low temperatures, the peak intensity decay was small. At high temperatures, the peak intensity decay was large. Some peaks almost disappeared completely from the spectra at the highest temperatures.
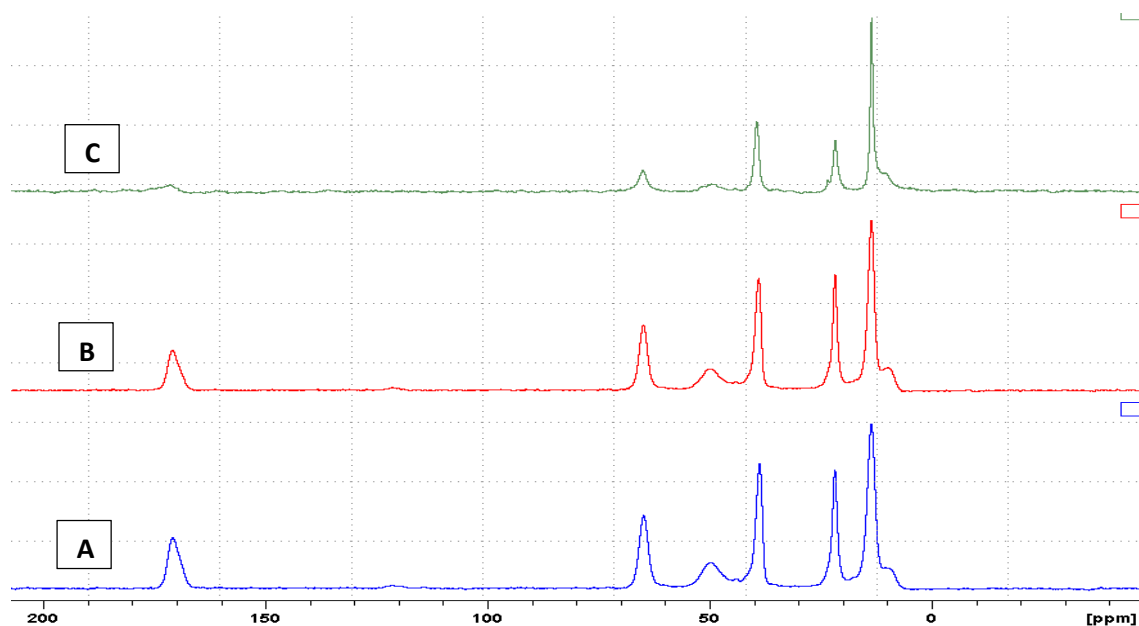
Figure 4. Peak intensity decay of solid-state ^{13}C CPTOSS NMR spectra of poly(isobutyl methacrylate) at (A) 270, (B)320, and (C)370 K.

Peak intensities vs temperatures were plotted for each carbon. The pendant carbonyl carbon peak intensities decayed as a function of temperature as shown in Figure 5. Initially, the decay of peak intensities proceeded very slowly. Then the decay of peak intensities increased significantly. As a result, the curve exhibited an inflection point. Extrapolation of two linear portions to the intersection point yielded the temperature at which the carbonyl carbon may have increased its motion. The temperature was 322 K, very close to the first deviation temperature observed in the DSC thermogram, which occurred at approximately 321 K.
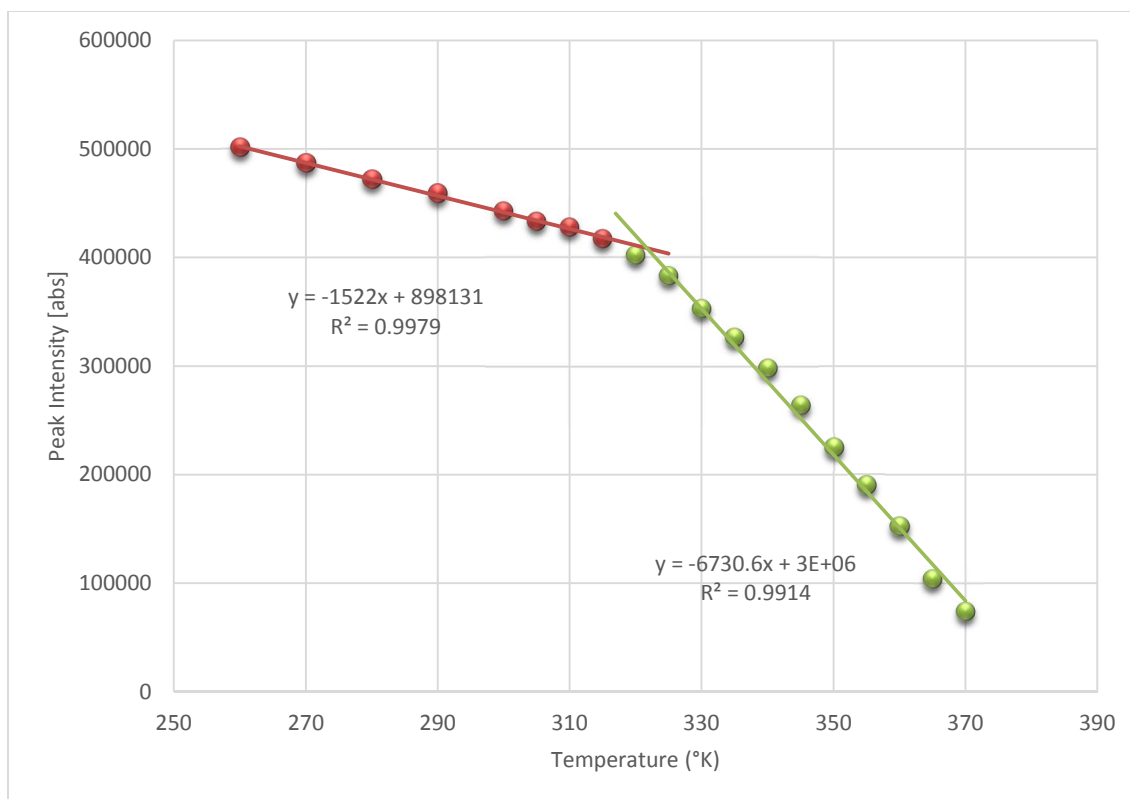
Figure 5. ^{13}C signal intensities of the carbonyl carbon of poly(isobutyl methacrylate) plotted as a function temperature.

Plot of the (-OCH$_2$-) peak intensities as a function of temperature illustrated similar behavior (Figure 6). The two linear regions exhibit an intersection point at 321 K. The lower intersection point of the (-OCH$_2$) carbon compared to that for the carbonyl carbon was probably due to the fact that the (-OCH$_2$-) group was flexible and exo to the backbone, hence segment mobility occurred at a lower temperature.
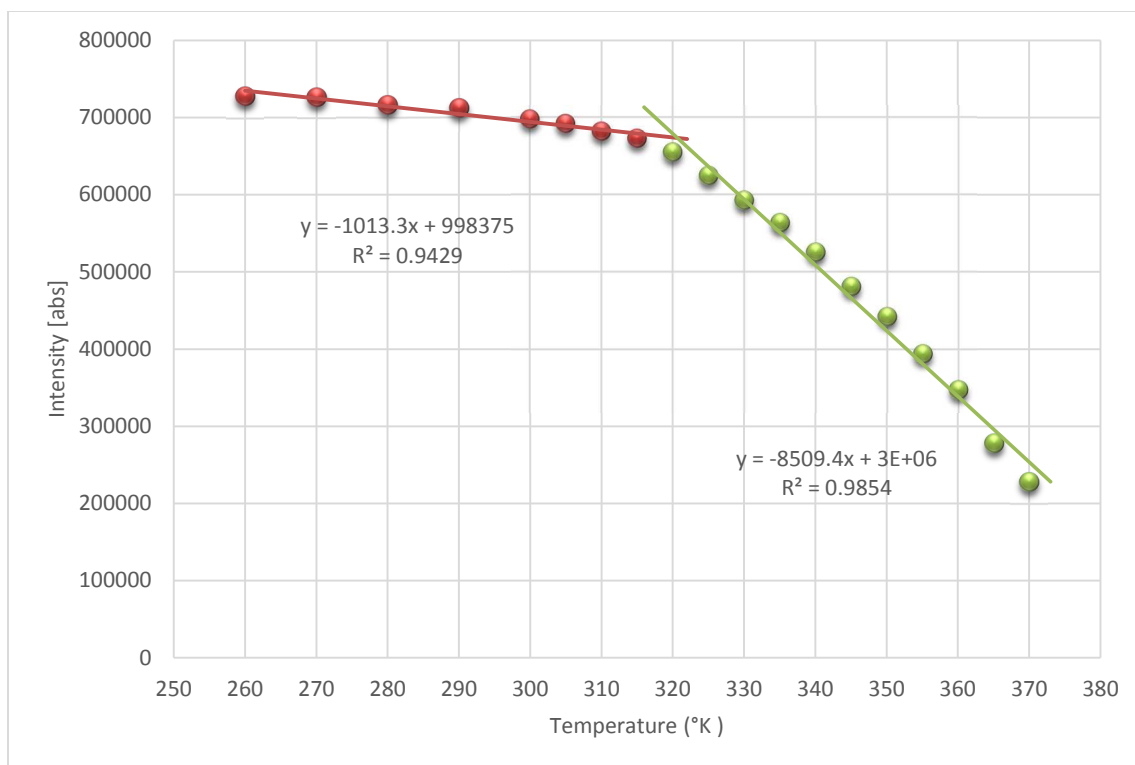
Figure 6. ^{13}C signal intensities of the (-O-CH$_2$) of poly(isobutyl methacrylate) as a function of temperature.

Figure 7 illustrates the decay of the peak intensity for the (-CH-) carbon as a function of temperature. The intersection point in the (-CH-) curve appeared at 314 K. This temperature is lower than the first deviation temperature measured by DSC (321K). The results seem to imply that there is more free volume in the vicinity of the (-CH-) group, likely due to poor polymer packing.
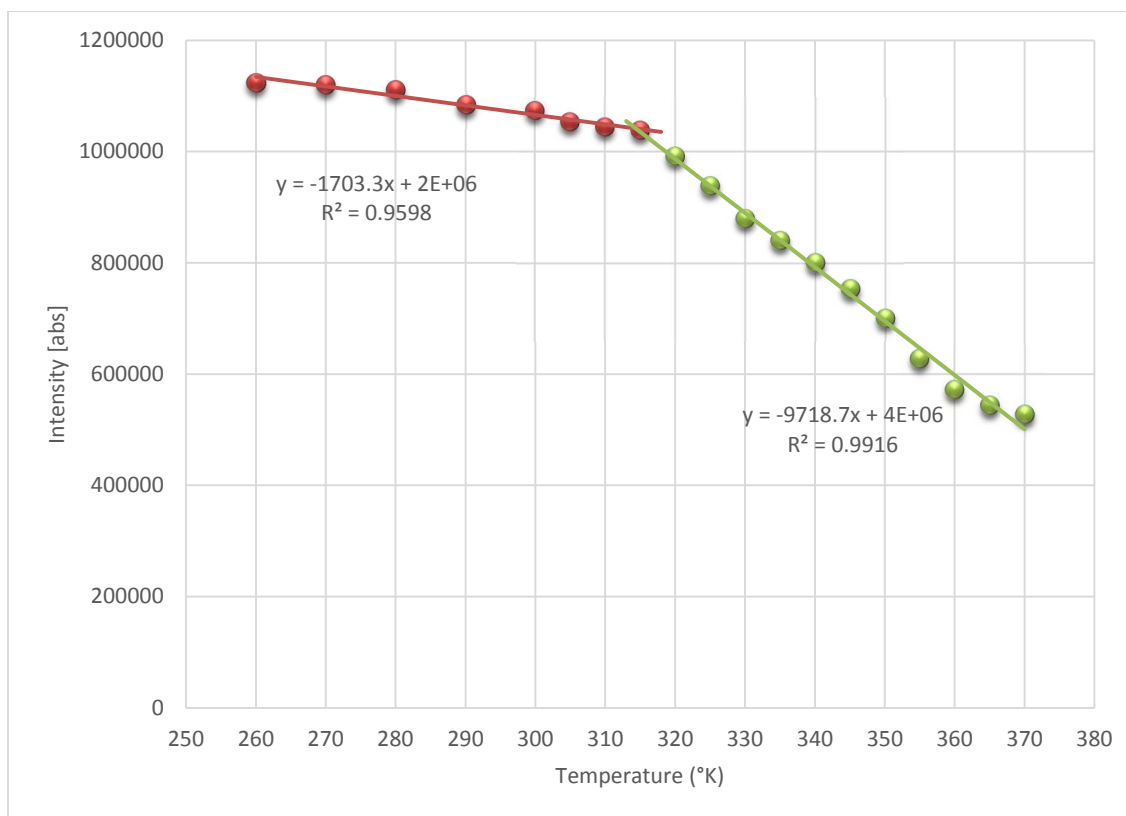
Figure 7. [13]C signal intensities of the (-CH-) carbon of poly(isobutyl methacrylate) as a function of temperature.

The plots of methylene and quaternary backbone carbons are shown in Figures 8 and 9. The methylene and quaternary backbone carbons curves exhibit intersection points at 326K and 324K, respectively.   The backbone carbons possessed the highest intersection point temperatures. These temperature points are somewhat below the 332K midpoint observed in the DSC measurements. This indicates that the NMR method is sensing polymer motion at its earliest onset temperature point. The breadth of the DSC transition encompasses all the chain movements and is consistent with the NMR data.
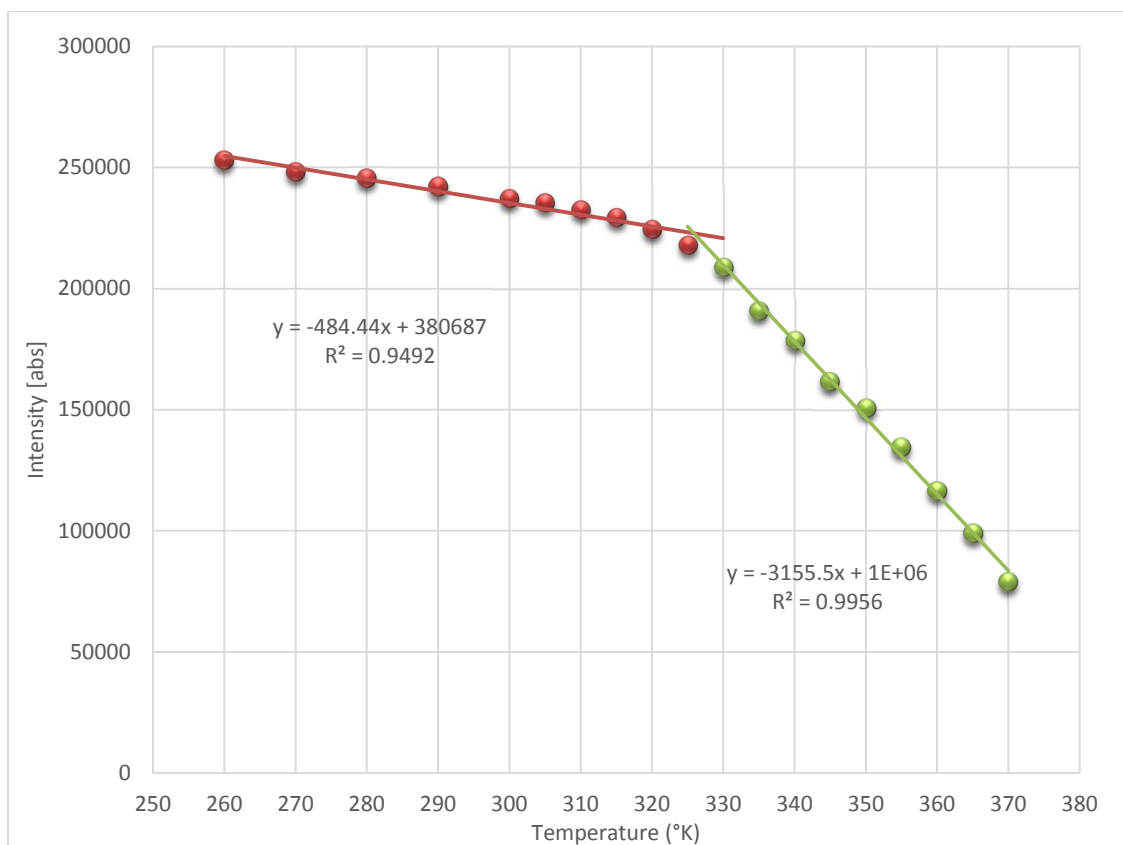
Figure 8. ^{13}C signal intensities of the methylene carbon of poly(isobutyl methacrylate) as a function of temperature.
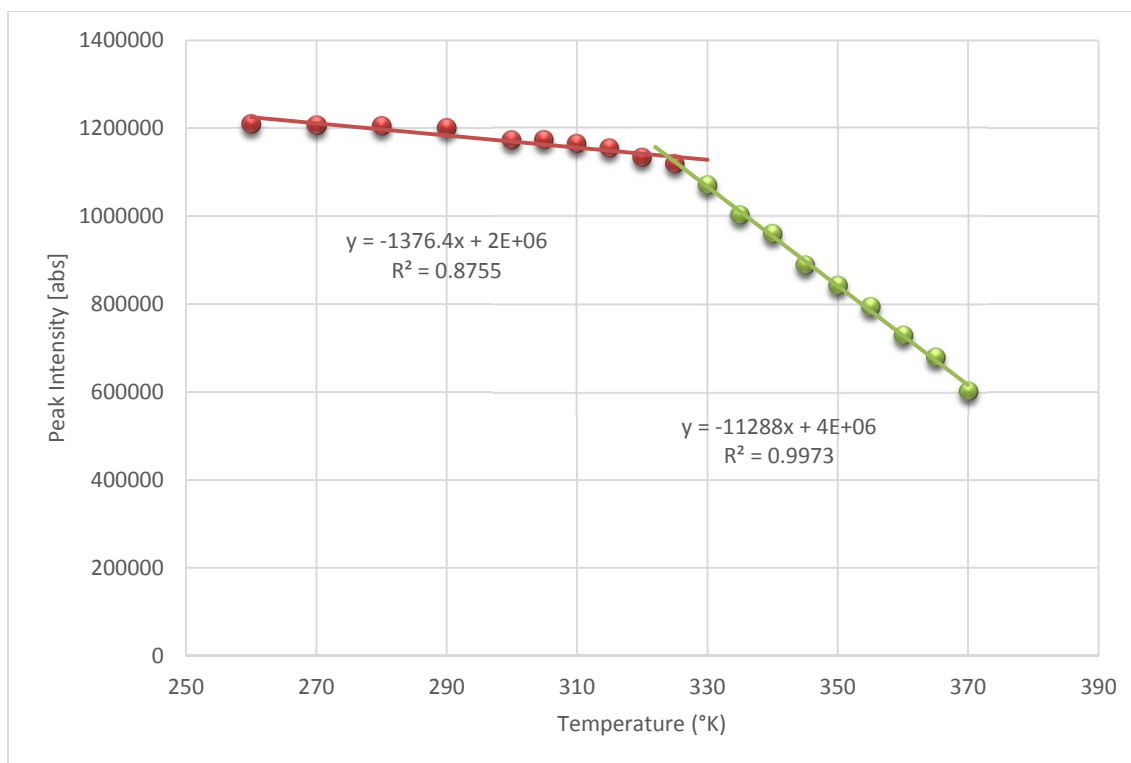
Figure 9. ^{13}C signal intensities of the quaternary carbon of poly(isobutyl methacrylate) as a function of temperature.

The decay of the methyl carbon peak intensity as a function of sample temperature showed large scatter. It was not possible to accurately determine the inflection point temperature (see Figure 10). It would be assumed that the plot displays two intersection points. The first transition occurred at lower temperature and was most likely associated with motion of methyl carbons located far away from the polymer backbone. The second transition occurred at higher temperature and was most likely reflective of the transition of the methyl carbon bonded to polymer backbone. Due to their high molar abundance and direct bonding to three protons, the methyl carbons have the greatest peak intensity. The methyl carbons on the side chain peaks overlaps with pendant

methyl carbon bonded to quaternary carbons in backbone chain. Peak overlap may contribute to inaccurate peak intensity determinations especially since both should exhibit different peak decays with increasing sample temperature.
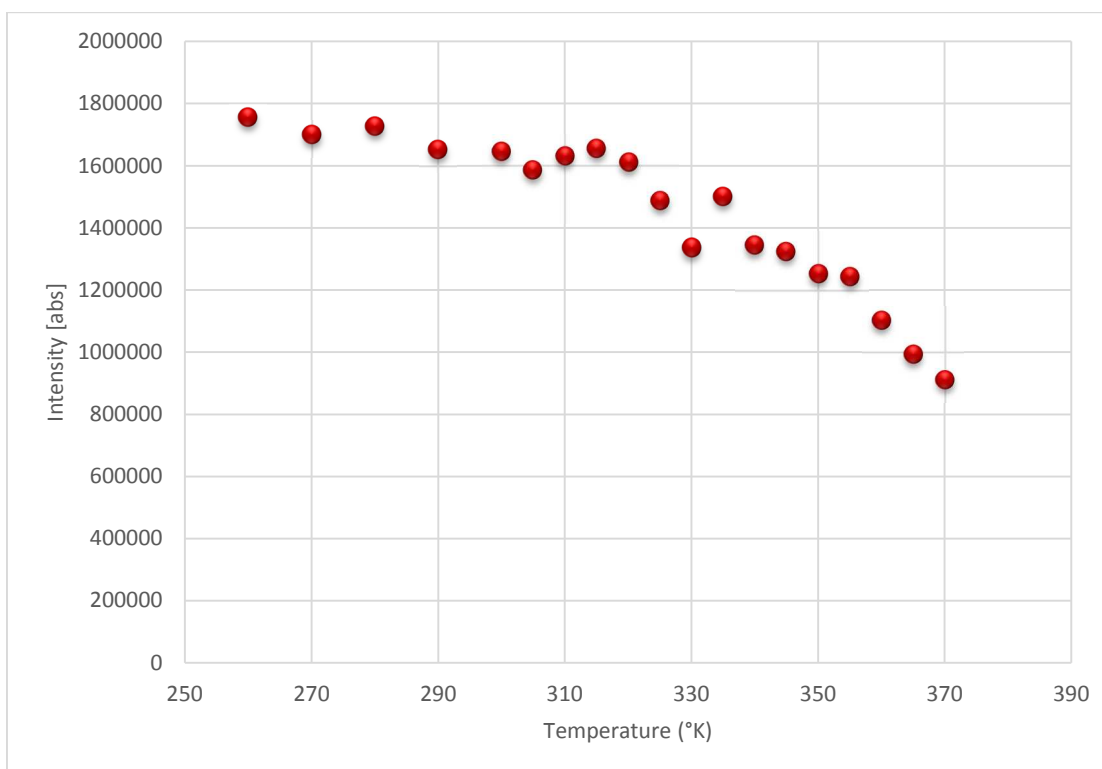
Figure 10. ^{13}C signal intensities of the methyl carbon of poly(isobutyl methacrylate) as a function of temperature.

3.2 Copolymer poly(MMA/BA/TFEMA/AA)

The chemical structure of the synthesized copolymer poly(MMA/BA/TFEMA/AA) is shown in Figure 11. The most intense peaks in ^{13}C CPTOSS NMR spectra were the quaternary and methylene carbons in the polymer backbone as well as the carbonyl carbon. Although the quaternary carbon in the polymer backbone has no directly bonded hydrogens, the high

molar abundance and protons on adjacent methylene and methyl carbons provided substantial signal intensity enhancement through cross polarization. The quaternary backbone carbon resonance appeared around 38 ppm, and a neighboring methylene carbon resonance was observed at 46 ppm. The pendant carbonyl carbon resonance was downfield at 170 ppm. The peak at 59 ppm was assigned to the methoxy carbon. The trifluoromethyl group resonance appeared at 119 ppm. The ^{13}C NMR results were consistent with similar structures reported in the literature [19, 20, 21, 22].
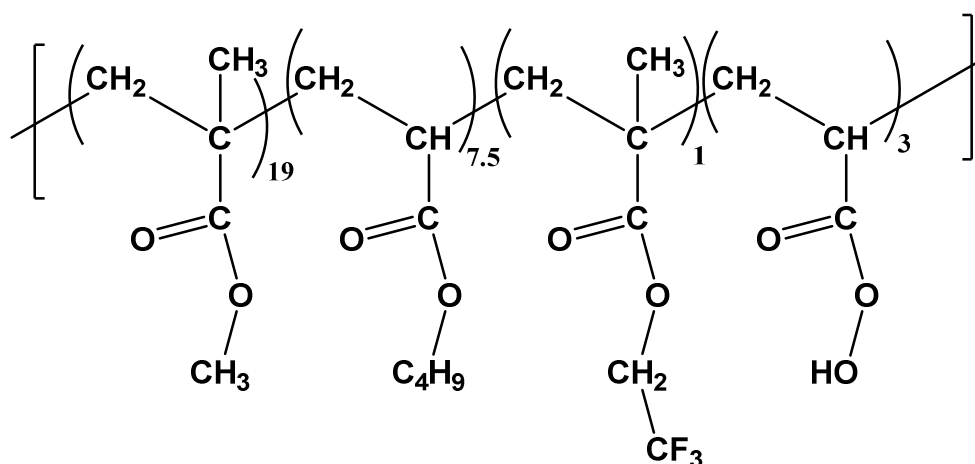
Figure 11. The chemical structure of copolymer RX-19

As the sample temperature increased, a decrease in the intensity of several spectral peaks was observed. Figure 12 includes the ^{13}C NMR spectra recorded at three different temperatures. The reduction of peak intensities was small at low sample temperatures, but was more pronounced at high sample temperatures.
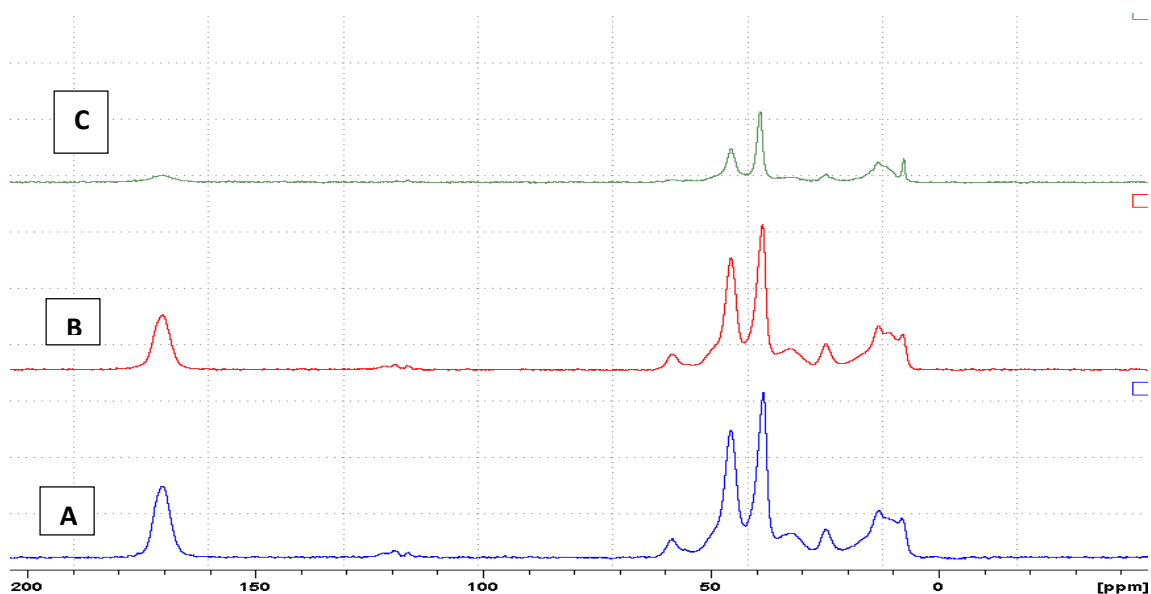
Figure 12. Peak intensity decay of solid-state ^{13}C CP-TOSS NMR spectra of copolymer RX-19 sample at (A) 270K, (B) 320K, and (C) 370 K.

Figure 13 shows the peak intensity of the quaternary backbone carbon versus the sample temperature. It can be seen from the plot that the peak intensity decays slightly as the sample temperature starts to increase, but at a sample temperature that approaches 340 K, a significant decay of the peak intensity was observed. The data points constitute two linear segments. At lower sample temperatures the decay in peak intensity is small, but above the intersection point, the peak intensity decay increases more rapidly. Extrapolating the two linear data point portions yields an intersection point at 338 K. The sample temperature corresponding to the intersection point is most likely the onset motion of quaternary backbone carbon. The intersection point temperature (338 K) was below the DSC midpoint (343 K), and higher than the DSC first deviation temperature (328 K).
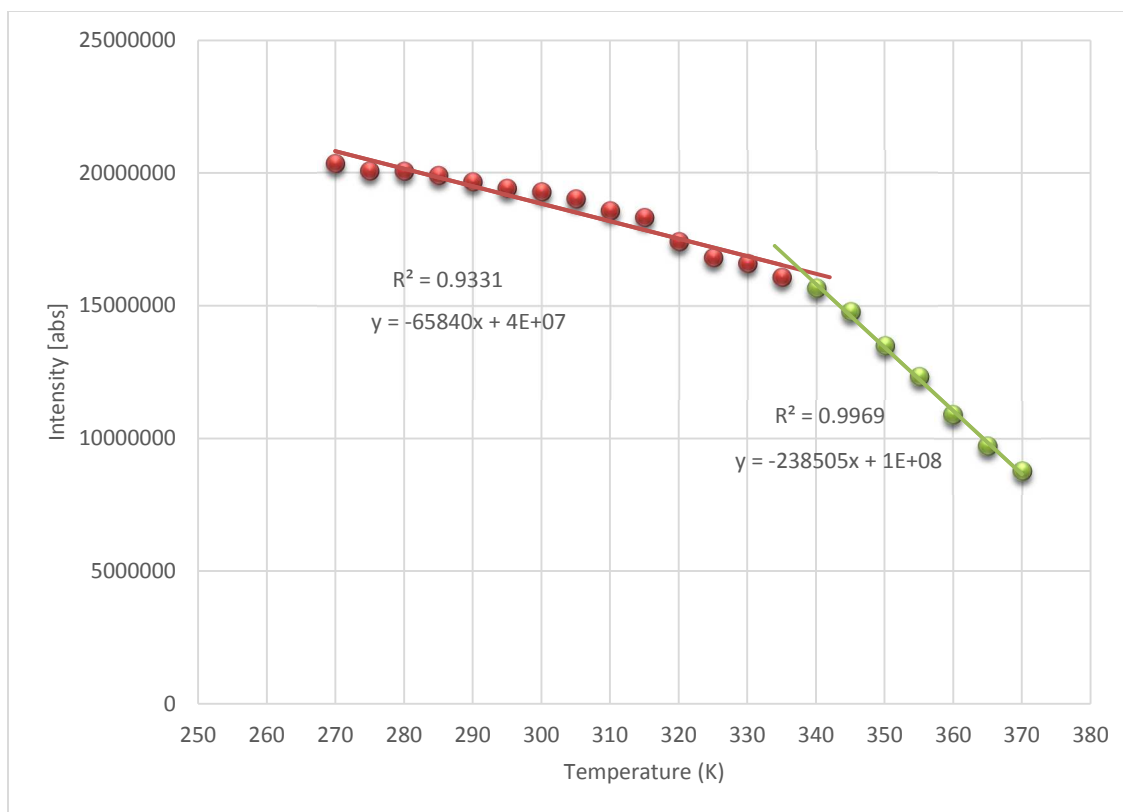
Figure 13. ^{13}C signal intensities of the quaternary carbon of copolymer RX-19 as a function of temperature.

A similar finding was observed for the methylene carbon in the backbone. Figure 14 illustrates the two regions with an intersection point at 338 K. This can be explained based on the fact that both carbons (quaternary and methylene) are in the polymer backbone. Therefore, there is an internal self-consistency in the molecular motion probed by this NMR method.
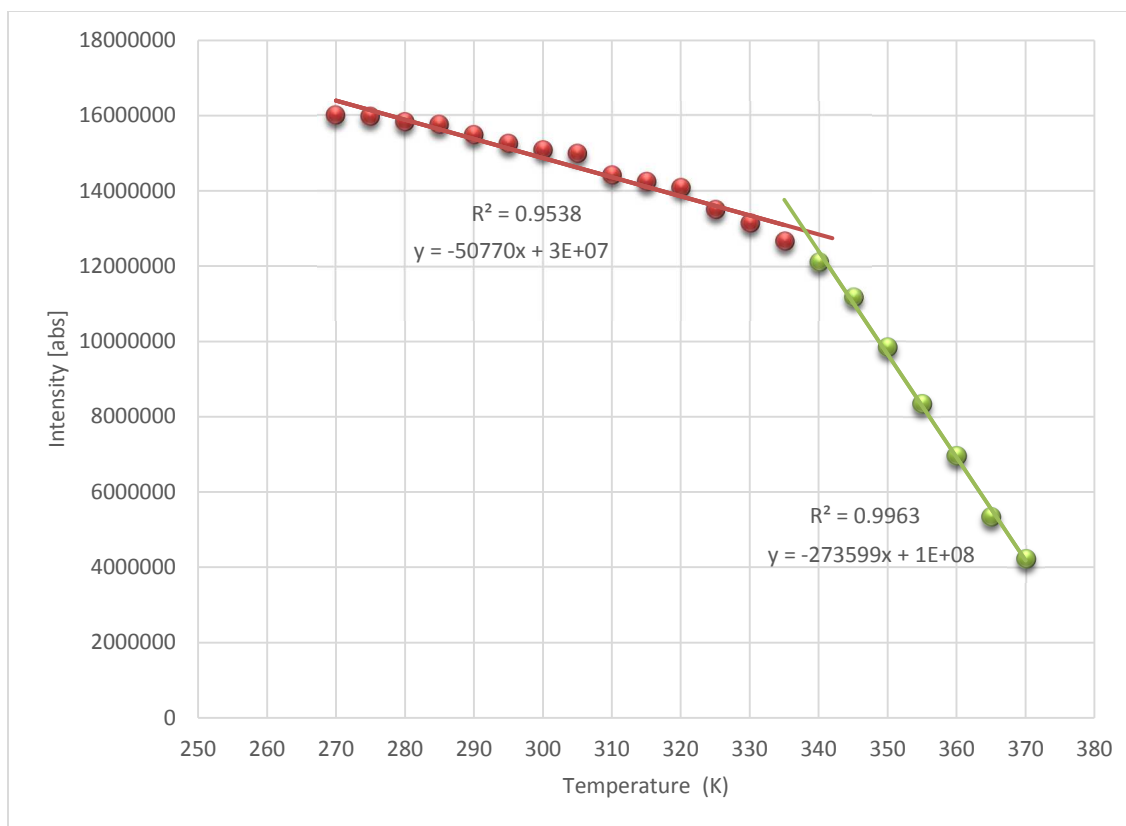
Figure 14. ^{13}C signal intensities of the methylene carbon of copolymer RX-19 as a function of temperature.

The pendant carbonyl carbon plot is displayed in Figure 15. This carbon is not in the chain backbone, so it has a higher degree of motional freedom compare to backbone carbons. The lines shown in the plot intersected at 330 K, about 8 degrees lower than the onset temperature of backbone motion, and somewhat below 328K, the first deviation temperature determined from the DSC result. The carbonyl carbon is part of a pendant group. The presence of pendant groups on the polymer main chain may prevent side chains from packing as tightly as the backbone; therefore, the pendant carbonyl carbon has more room available for mobility than the backbone. The lower intersection temperature of

the pendant carbonyl carbon compared to main chain carbon can be attributed to the availability of more free volume.
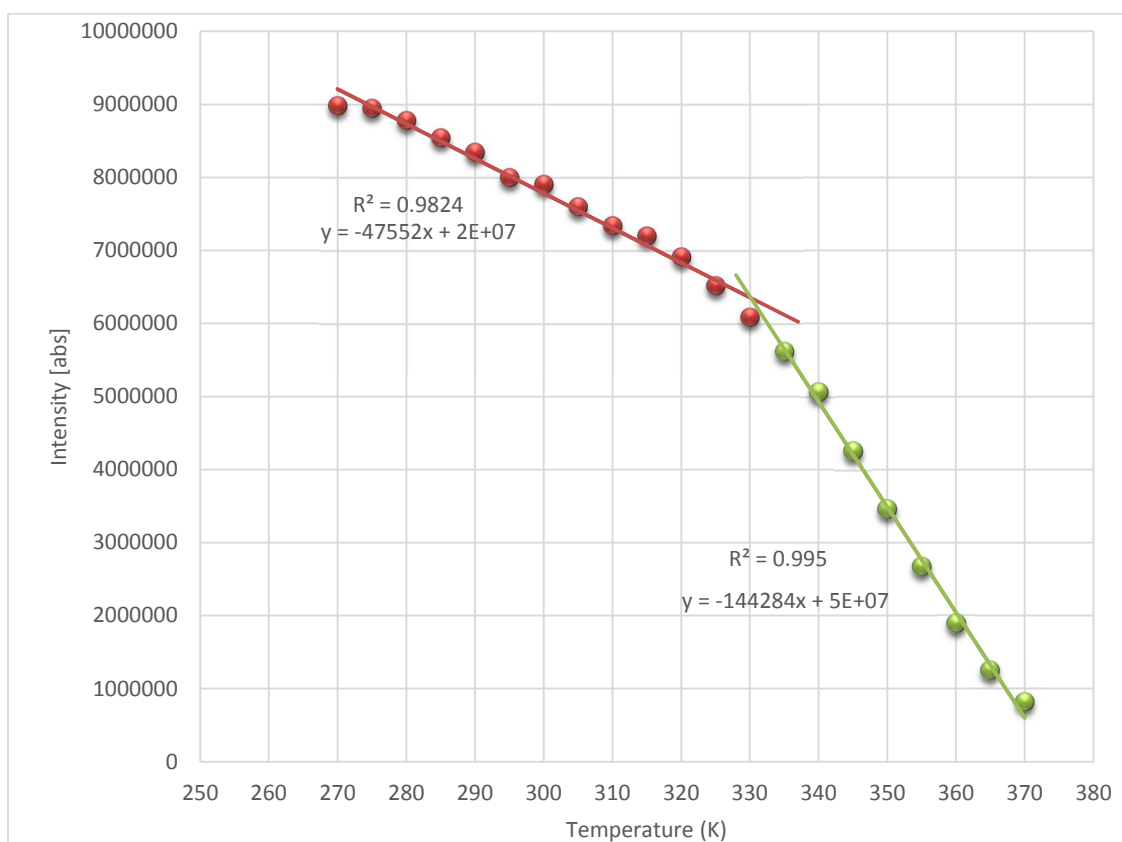
Figure 15. [13]C signal intensities of the carbonyl carbon of copolymer RX-19 as a function of temperature.

The methoxy carbon peak intensity versus sample temperature is illustrated in Figure 16. At low sample temperature, significant data scattering was observed. The scattering can be attributed to peak overlap. The intersection point did occur at a similar temperature to that observed for the carbonyl carbon, 330 K.
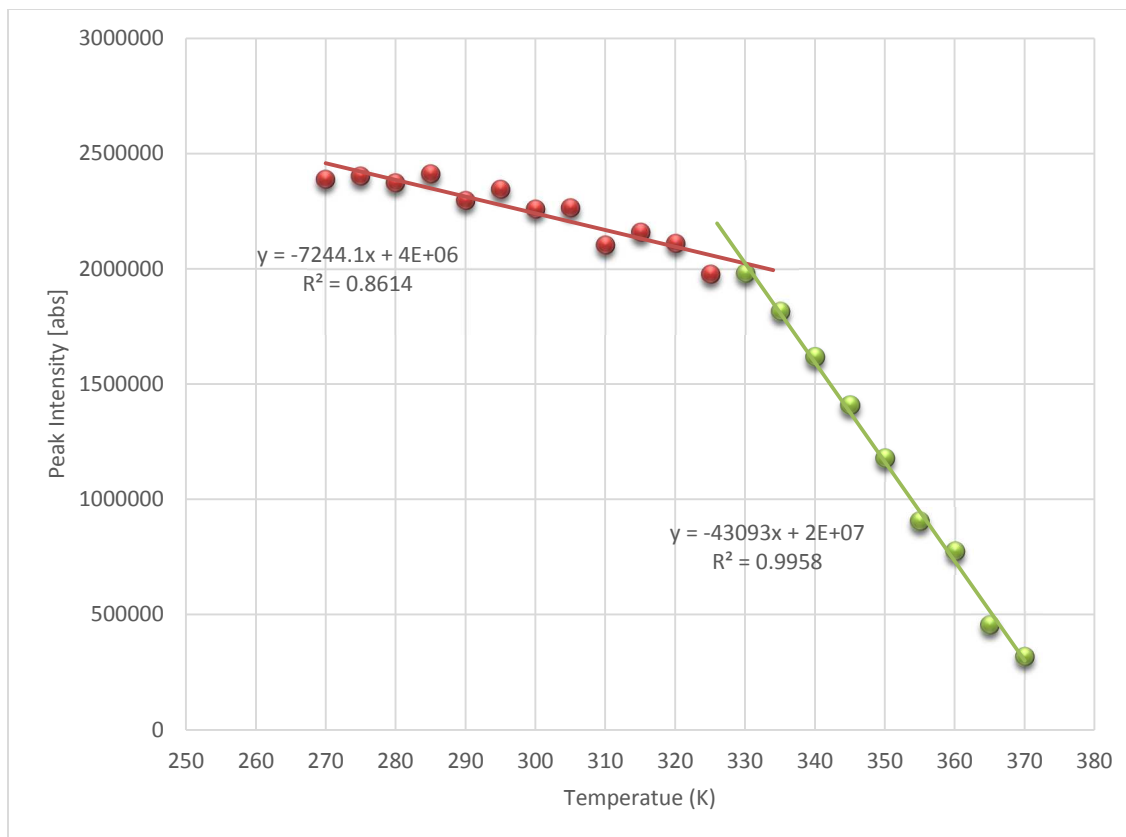
Figure 16. ^{13}C signal intensities of the methoxy carbon of copolymer RX-19 as a function of temperature.

As for the trifluoromethyle group, the values of peak intensity as a function of sample temperature revealed much large scatter compared to the data shown in Figure 17. Therefore, the intersection point temperature cannot be accurately determined. The best intersection point occurs approximately between 330K and 333K. The primary reason behind this data point scatter was low signal strength. This carbon is not directly bonded to protons and has a low molar abundance. The dipolar interaction was expected to be weak, resulting in poor signal enhancements [6,7].
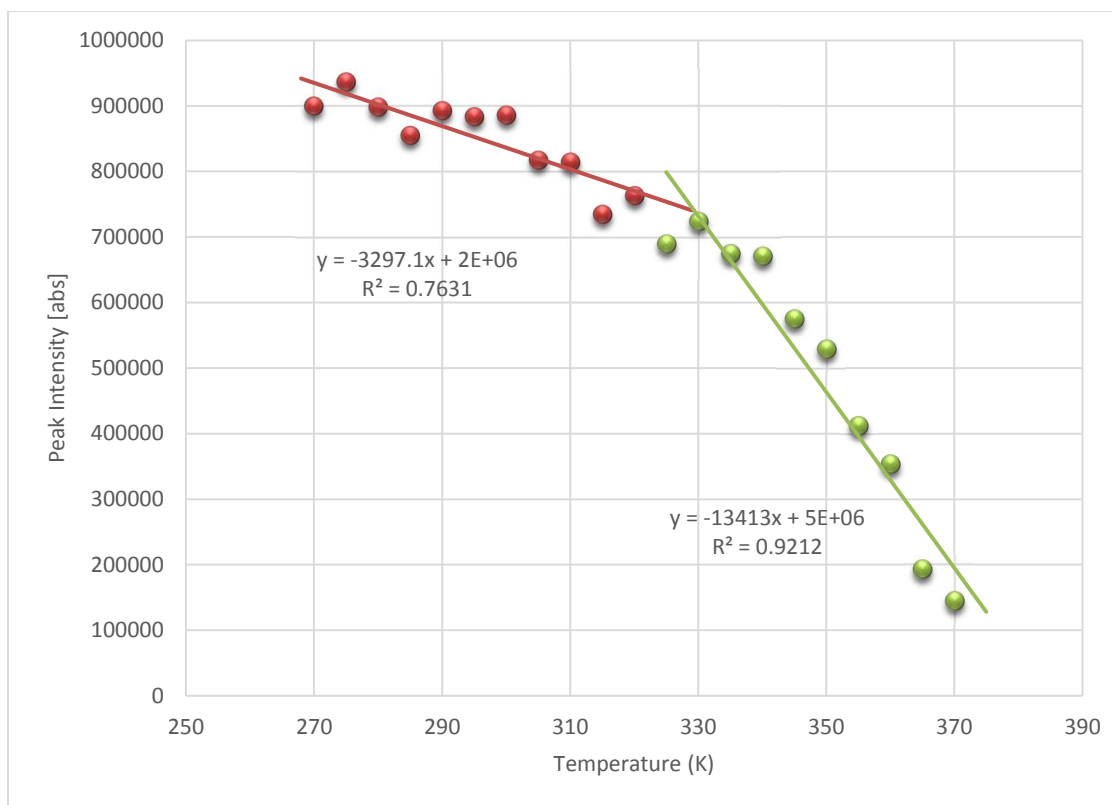
Figure 17. ^{13}C signal intensities of the trifluoromethyl carbon of copolymer RX-19 as a function of temperature.

Table 2 summarized the intersection points measured by the CP-TOSS method, and includes the DSC measurements. The intersection points of solid state NMR peak intensity decay measurements reflect the sample temperature where the onset of motion was measured by DSC. The backbone carbons exhibited intersection points close to the midpoint, Tg, measured by DSC. In turn, the side chain carbons in both polymers exhibited an intersection point temperature close to the first deviation temperature measured by DSC. The difference between the solid state CP-TOSS and DSC measurements may be attributed to the ability of solid state NMR to detect small timescale dynamics

[23]. The sensitivity of this NMR technique provides more details about polymer dynamics compared to DSC.

Table 2

First deviation and midpoint temperatures measured by DSC and intersection points by CP-TOSS method.

Polymer	Segment	DSC		CP-TOSS
		First Deviation Temperature (K)	Mid-Point (K)	Intersection Point (K)
Homopolymer poly(isobutyl methacrylate)	C=O	321	332	322
	-OCH$_2$-	321	332	321
	-CH-	321	332	314
	quaternary	321	332	324
	methylene	321	332	326
	methyl	321	332	--
Copolymer fluorinated polymer RX-19	C=O	328	343	330
	-OCH$_3$	328	343	330
	quaternary	328	343	338
	methylene	328	343	338
	-CF$_3$	328	343	330

The cross polarization efficiency is inversely proportional to the distance between investigated carbons and nearby protons from which the polarization was transferred. Also, the energy of interaction greatly depends on the angle between the external field and the C-H vector (see Equation 2). Temperature-activated motion causes this angle to modulate resulting in an averaging and reduction of interaction. The intersection point of temperature-induced peak intensity decay curves reflects the pronounced change of either C-H distance and/or the angle between C-H vector and B_o. We suggest that segmental motion is responsible for changing distance and angle. It is apparent from Table 2 that there is a different intersection point temperature associated with each segment. As the distance from the backbone increases, the intersection point sample temperature decreases. The side groups minimize chain packing efficiency. Hence, the energy barrier to segmental motion is lower. The spaces available for side chains allow the dynamics to take place at lower onset temperatures than the backbone chain.

4. CONCLUSION

Variable temperatures CP-TOSS ^{13}C NMR experiments were utilized to study polymer dynamics. A homopolymer and copolymer were investigated by this method. Plots of carbon peak intensities for each segment in the polymer chain vs temperature yielded two linear regions. The intersection point temperatures for line pairs were found to be close to the first deviation temperatures measured by DSC. Variable temperature peak intensity decay can

provide information about the dynamic motions of both main chain and side chains in polymer systems. However, this method is associated with some limitations, carbons with low molar abundance, lack of attached protons, and carbons with overlapping peaks do not exhibit clearly defined intersection points.

5. ACKNOWLEDGMENTS

The authors thank the Department of Chemistry and Missouri S& T Coating Institute for financial support and resources.

6. REFERENCES

[1] Ibbett R N. NMR Spectroscopy of polymers, First edition, Blackie Academic & Professional, 1993.

[2] Henrichs P M, Nicely V A. Macromolecules 1991; 24: 2506

[3] Brennan W P, A review of the glass transition. Perkin-Elmer Therm. Anal. Study 1973; 7.

[4] Wunderlich B, Turi E A, Ed.; Academic Press: Orlando, FL 1981: 91

[5] L.H. Sperling. Introduction to physical polymer science, Fourth edition, John Wiley & Sons, Inc. 2006. Page 349.

[6] Carmel AR, Wasylyk JM, Baust JG. J. Agric. Food Chem1990; 38:1824.

[7] Lyeria JR, Yannoni CS. IBM J. Research Development 1983; 27: 311.

[8] Oliver Z, Simon J. Applied NMR Spectroscopy for Chemists and Life Scientists, John Wiley & Sons. Inc., 2013, Chapter 18, page 383-394.

[9] Schaefer, Jacob, Stejskal, EO. Buchdahl, R. Macromolecules 1975; 8:291.

[10] Schaefer J, Stejskal E, Buchdahl R. Macromolecules 1977; 10:384.

[11] Garroway AN, Vander Hart DL. J. Chem. Phys 1997; 71:2773.

[12] Fyfe CA, Mossbrugger H, Yannoni CS. J. Magn. Reson 1979; 36: 61.

[13] Lyerla JR, Yannoni CS, Fyfe CA. Acc. Chem. Res 1982; 15:208.

[14] Garroway AN, Ritchey WM, Moniz WB. Macromolecules 1982; 15:1051

[15] McGrath KJ, Ngai KL, Roland CM. Macromolecules 1995; 28:2825

[16] Dixon WT. J Chem Phys 1982; 77:1800.

[17] Dixon WT, Schaefer J, Sefcik MD, Stejskal EO, Mckay RA. J Magn
    Reson 1982; 49:341.

[18] Conte P, Spaccini R, Piccolo A. Progress in Nuclear Magnetic
    Resonance Spectroscopy 2004; 44: 215.

[19] Changa TC, Shiha CC, Yina CP, Chenb HB, Wu TR. Polymer
    Degradation and Stability 2005; 87: 87.

[20] Souto-Maior RM, Tavares MI, Monteiro EE, Ann. Magn. Reson
    2005; 4:69.

[21] Mansur C R, Tavares MI, Monteiro EE. Journal of Applied Polymer
    Science 2000; 75: 495.

[22] Georgiev GS, Dakova IG, Eur. Polym. J 1994; 30:1417.

[23] Roach DJ, Dou S, Colby RH, Mueller KT. The Journal of Chemical
    Physics 2013; 138:194907.

III. ANTICORROSIVE EFFECTS OF DERIVATIZED 5-MERCAPTO-1,3,4-THIADIAZOL-2(3H)-THIONE (MTT) AT THE THIOL POSITIONS

Yousef Dawib[a], Aysel Büyüksagis[b], Jigar K. Mistry[a], and

Michael R. Van De Mark[a]*

[a] Missouri University of Science and Technology, Rolla, MO,USA 65409

[b] Afyon Kocatepe University, Afyonkarahisar 03200, Turkey

*Corresponding Author. mvandema@mst.edu

ABSTRACT

A series of 5-mercapto-1, 3, 4-thiadiazole-2(3H)-thione (MTT) derivatives were synthesized and tested for their ability to inhibit corrosion on steel and 304 stainless steel substrates in a 3.5% NaCl solution. This work sought to assess which derivatives possessed the best capacity toward corrosion inhibition. The substituents on the MTT were varied to determine the effect of hydrophobicity, molecular size, and steric hindrance on corrosion inhibition. Both mono and di alkylated MTT were prepared and corrosion behavior investigated by electrochemical impedance spectroscopy (EIS) and potentiodynamic polarization measurements. The results revealed that the best inhibition efficiency of MTT derivatives was achieved by 5-(methylthio)-1,3,4-thidiazole-2(3H)-thione (Me-MTT). In contrast, the poorest inhibition was recorded when 5-(butylthio)-1,3,4-thidiazole-2(3H)-thione (Bu-MTT) was added, the parent MTT was even poorer. Bu-MTT has a greater steric substituent size than Me-MTT, thus the steric hindrance effect resulted in poorer packing on metal surface.

1. INTRODUCTION

Due to environmental regulations, the use of chromate-based inhibitors has been restrained, and a tremendous need for alternative inhibitors has emerged. Organic corrosion inhibitors can be regarded as a pragmatic, alternative approach to existing chromate-based inhibitors. The protection performance of organic inhibitors relies on the molecule's adsorption strength to form an adhered protective film on the metal substrate. The organic molecule interacts with the metal surface either by chemisorption or by physical adsorption [1]. Chemisorption is the most important type of interaction. It functions by forming coordinating –type bonds between metal and organic molecule [1]. A coordinate bond involves the transfer of electrons from an organic molecule to a metal ion on substrate surface.

The chemical structure of an organic molecule is the most important element in both selection and design of an effective organic corrosion inhibitor molecule. The most efficient organic inhibitors are organic compounds that possess reactive atoms with an unshared lone pair of electrons. In general, molecules that containing a nitrogen, oxygen, phosphorus, selenium, or sulfur

have a good tendency to adsorb on metal substrates [1]. The inhibition efficiency generally increases in the following sequence:

Selenium > Sulfur > Nitrogen > Oxygen

This order is explained by a lower electronegativity of elements on the left that make their compounds easily susceptible to polarization [2]. Riggs [3] confirmed this finding and found that sulfur containing inhibitors are superior to nitrogen containing inhibitors. Moreover, the existence of both nitrogen and sulfur atoms in cyclic compounds are more efficient than either element alone.

It is well established that an increase in the electron density on the functional atom will result in increased ability of the organic molecule to be adsorbed on the metal surface. For example, the availability of π electrons, due to the presence of either multiple bonds or aromatic rings, would aid the electron transfer from an organic molecule toward the metal. It would also enhance the electron density on the donor atom. Hackerman et al. [4] found that the inhibition efficiency is enhanced by increasing the electron density at a ligating atom. Trabanelli's et al. [5] validated this finding as they studied alicyclic amine compounds. They concluded that an increase in the inhibitor's effectiveness is associated with the high electron density surrounding the nitrogen atom. This effect can also be influenced by introducing either electron donating or electron withdrawing substituents in a suitable position within molecule [1].

The molecular weights of organic molecules have been correlated with the ability to retard corrosion. Li, Tan and Lee [6] suggested that the molecular weight of an organic molecule greatly influences the corrosion inhibitive

efficiency. They deduced that a larger molecule will offer better corrosion protection as long as the molecule still possesses a minimum solubility in water. They also suggested that the corrosion protection can be enhanced if the organic molecule has an N-H bond. This bond, in turn, establishes hydrogen bonding with an oxygen atom of metal oxide [6].

Recent attempts [7-11] were made to correlate the inhibition efficiency with quantum chemical parameters. The highest occupied molecular orbital (HOMO), the lowest unoccupied molecular orbital (LUMO), the HOMO–LUMO gap, charges on the reactive center, and the dipole moment (μ) have each been used to characterize inhibitor performance. Electrons in the HOMO can be easily donated to a metal surface. Fang and Li [7] performed quantum chemical calculations on four typical amide compounds. They found that the inhibition efficiency decreases as the E_{HOMO} level decreases. It has been proposed that the effective corrosion inhibitor molecule is capable of electron donating to the unoccupied orbital of the metal in conjunction with its ability to accept free electrons from the metal [7]. Semi-empirical calculations [8] indicated that high efficacy compounds have both a high E_{HOMO} value and a low E_{LUMO} value. The E_{HOMO}–E_{LUMO} energy difference is directly related to the molecule's stability. Sastri [11,12] found that a smaller E_{HOMO}-E_{LOMO} value can enhance corrosion inhibition. The orbital theoretical calculations performed on substituted methyl pyridines and substituted ethane derivatives, clearly showed that the corrosion protection improves with the increase in E_{HOMO}, and decrease in E_{HOMO}-E_{LOMO} gap. The dipole moment is another important parameter that may be linked to

inhibition efficiency. The available literature [13-14] suggests that a lack of agreement exists on the correlation between the dipole moment and the inhibition efficiency.

Among the heterocyclic organic compounds that contain both sulfur and nitrogen atoms, 5-mercapto-1,3,4-thiadiazole-2(3H)-thione (MTT) possess five electron pair donating atoms, two nitrogen and three sulfur. These atoms can be strongly chemisorbed onto a metal surface to form a barrier film. This compound has a broad range of potential applications, and unique chemistries. The effectiveness of (MTT) as a corrosion inhibitor for copper in an acid solution has been investigated [15]. The results revealed superior inhibition performance. The MTT adsorb on copper surfaces and forms a monolayer that inhibit both anodic and cathodic reaction sites. Similar findings for MTT corrosion inhibition of mild steel in sulfuric acid have been reported [16]. The results showed lower inhibition than copper. These studies concluded that the MTT acts as a mixed type inhibitor and predominantly acts at the anodic sites. Moreover, a study[17] on efficiency of 5-mercapto-3-phenyl-1,3,4-thiadiazole-2-thione potassium) on copper substrate in a sodium chloride solution shifted the corrosion potential to more positive region which suggest that the MTT was functioning by inhibition of the anodic dissolution of copper. The structure of MTT have been reported in three different forms. Figure 1. Shows MTT's possible structures.
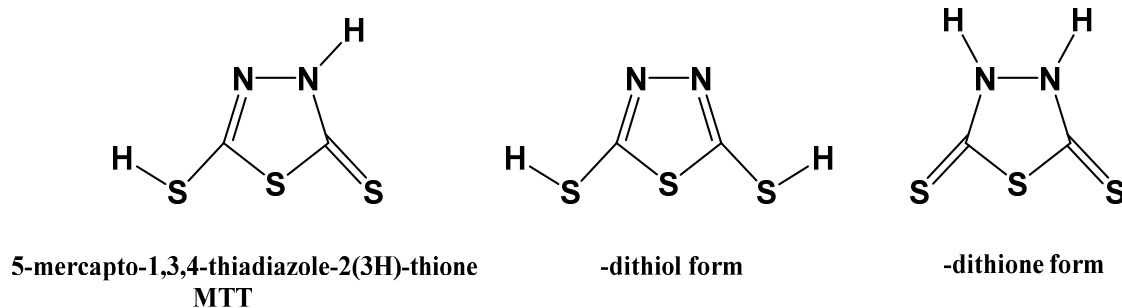
Fig. 1. Three tautomeric forms of MTT.

A detailed investigation into the structure of MTT and its alkylated derivatives was conducted [18]. A combination of X-ray crystallography, ^{13}C nuclear magnetic resonance spectroscopy, and **ab-initio** electronic structure calculations were used to explain which tautomer has the most stability. It was concluded that thion-thiol form is the lowest energy structural isomer. In turn, the most stable structure of mono and di alkylation of MTT are shown in Figure 2.
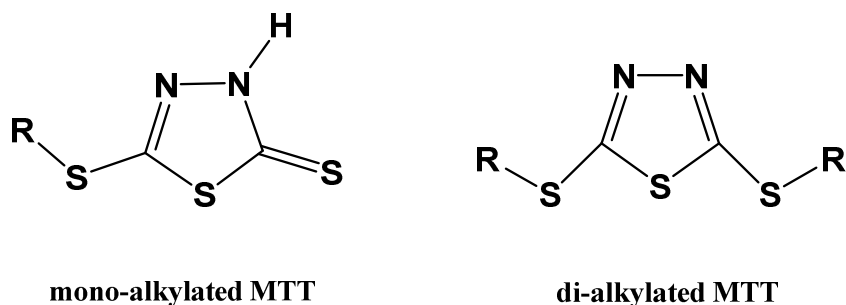
Fig. 2. Structures of mono-alkylated and di-alkylated MTT [18].

The goal of this work was to investigate the corrosion inhibition efficiency of 1, 3, 4-thiadiazole-2(3H)-thione (MTT) derivatives on different metal surfaces

in 3.5% NaCl. The derivative structure parameters were correlated with their effectiveness in corrosion inhibition. These parameters include derivative solubility in water, size of molecule, steric hindrance of the substituent, and quantum chemistry parameters. Electrochemical impedance spectroscopy and electrochemical polarization techniques were utilized for this investigation.

2. EXPERIMENTAL

2.1 Materials

The starting material 5-mercapto-1, 3, 4-thiadiazole-2(3H)-thione (MTT), was obtained from R.T. Vanderbilt. This company lists this chemical as 2,5-dimercapto-1,3,4-thiadiazole (DMTD). MTT was re-crystallized from benzene before use. All of the solvents were dried and distilled before use unless otherwise specified. All MTT derivatives were characterized by ^{13}C, ^{1}H NMR, IR, and MS. Cold rolled steel panels were purchased from Q-Lab Corporation, matte mill finish, R-36 type. The stainless steel specimens 304 were purchased from Anil Paslanmaz Celik Sanayi ve Ticaret Limited Sirketi, Turkey, composed of 0.037% C, 0.03% P, 0.52% Si, 0.02% S, 1.59% Mn, 0.48% Mo, 0.48% Cu, 0.067% N, 8.1% Ni, 18.04% Cr, and Fe the balance. The remaining reagents were purchased from either Fisher or Aldrich and used without further purification. The chemical structures, name, and abbreviation of MTT derivatives are listed figure 3, and table 1 shows the physical parameters of each compound.

R = H   MTT   R, R' = -CH$_3$ Me-MTT-Me

R =-CH$_3$ Me-MTT   R, R' = n-Bu   Bu-MTT-Bu

R= n-Bu   Bu-MTT   R, R' = -CH$_2$CO$_2$H   A-MTT-A

Fig. 3. The chemical structures, and abbreviations of the compounds

Table 1
Physical parameters of MTT derivatives

Compound	Molecular weight g/mole	Solubility in water* ppm
MTT	150.25	980
Me-MTT	164.27	510 (550**)
n-Bu-MTT	206.35	66 (74**)
Me-MTT-Me	178.30	170
n-Bu-MTT-Bu-n	262.46	1.7
A-MTT-A	266.32	250

*SciFinder, Calculated using Advanced Chemistry Development (ACD/Labs) Software V11.02 (© 1994-2013 ACD/Labs)
** Experimentally measured using spectrophotometry technique.

2.2 Synthesis of Mono-Methylated MTT (Me-MTT) [19]

5-Mercapto-1,3,4-thiadiazole-2(3H)-thione (0.1 mol, 15.02g) was added to a solution of potassium hydroxide (0.1 mol, 5.61g) in absolute ethanol (2.17 mol, 99.97 g). The reaction mixture was stirred and heated at 50°C for 30 min. The mixture was cooled before iodomethane (0.11 mol, 15.61g) was slowly added to the mixture and refluxed for 6 hours. The solution was then allowed to cool to room temperature and filtered. The filtered solution was diluted threefold with water to cause separation of the thioether. The precipitated product was filtered off and washed with distilled water. The resulting product 5-(methylthio)-1,3,4-thidiazole-2(3H)-thione (mol. wt. 164.27) was crystallized in benzene to afford a light yellow needle-like crystals. The product was dried in vacuo and the yield was 74% (12.15 g) Me-MTT. The melting point of the compound was 137-138 °C. Me-MTT was characterized by ^{13}C, ^{1}H NMR, IR, and MS. The Me-MTT showed ^{13}C peaks in d-DMSO at 159.39 (–N=C–S–Me), 187.51 (–N–C=S), and 14.67 ppm (–CH$_3$); ^{1}H singlet peak in d-DMSO at 2.52 (S–CH$_3$) and 14.30ppm (N–H); IR bands at 3050, 1480, 1365, and 1100 cm^{-1}; MS peaks at 164, 91, 88, 73 and 59m/z.

2.3 Synthesis of Mono-Butylated MTT (Bu-MTT) [20]

5-Mercapto-1,3,4-thiadiazole-2(3H)-thione (0.1 mol, 15.02g) was added to a solution of potassium hydroxide (0.1 mol, 5.61g) in absolute ethanol (2.17 mol, 99.97 g). The reaction mixture was stirred and heated at 50°C for 30 min. The mixture was cooled before 1-bromobutane (0.11 mol, 15.07g) was slowly added to the mixture and refluxed for 6 hours. The refluxed solution was then allowed to

cool to room temperature and filtered. The filtered solution was diluted threefold with water to cause separation of the thioether. The precipitated product was filtered off and washed with distilled water. The resulting product 5-(butylthio)-1,3,4-thidiazole-2(3H)-thione (mol. wt. 206.35) was dried in vacuo yielding 70% (14.4 g) Bu-MTT. Then Bu-MTT was recrystallized from benzene to afford a yellowish precipitate. The melting point of the compound was 94-95° C. Final product was characterized by ^{13}C, and ^{1}H NMR. The Bu-MTT showed ^{13}C peaks in d-DMSO at 159.39 (–N=C–S–CH2-), 187.51 (–N–C=S), 22 (–S-CH2), 34.3 ppm (-CH$_2$), and 14.67 ppm (–CH$_3$); ^{1}H peaks in d-DMSO, triplet at 3.2 (S–CH$_2$), multiple peaks at 1.46 and 1.68 (-CH$_2$), triplet peaks at 1.1 (-CH$_3$), and 14.30 ppm (N–H). IR bands at 3050, 1480, 1365, and 1100 cm^{-1}. MS peaks at 206,148, 104,57, and 32.

2.4 Synthesis of Di-Methylated MTT (Me-MTT-Me) [21]

5-Mercapto-1,3,4-thiadiazole-2(3H)-thione (0.1 mol, 15.02g) was added to an aqueous solution 100 ml distilled water with sodium hydroxide (0.3 mol, 12g) in 1,4-dioxane (0.12 mol, 100 ml). The reaction mixture was stirred and heated at 50˚C for 30 min. The mixture was cooled before iodomethane (0.21 mol, 29.80g) was slowly added to the mixture and refluxed for 6 hours. The refluxed solution was allowed to cool to room temperature and then poured into water. This solution was extracted twice with diethyl ether and dried over anhydrous sodium sulfate. The dried solution was filtered and rotovaped. The resulting product was a yellowish liquid 2, 5-bis(methylthio)-1,3,4-thiadiazole (mol. wt. 178.30). The yield was 79% (14.08 g). The boiling point of the compound was 311-313°C at

atmospheric pressure. Final product was characterized by ^{13}C, 1H NMR, and MS. The Me-MTT-Me showed ^{13}C peaks in d-DMSO at 165.56 (–N=C–S–Me) and 15.60 ppm (–CH$_3$); ^{1}H singlet peak in d-DMSO at 2.55 ppm (–CH$_3$), and GC–MS parent peak at 177 and significant m/z peaks at 146, 162, 91, and 87.

2.5 Synthesis of Di-Butylated MTT (Bu-MTT-Bu) [21]

5-Mercapto-1,3,4-thiadiazole-2(3H)-thione (0.1 mol, 15.02g) was added to an aqueous solution 100 ml distilled water with sodium hydroxide (0.3 mol, 12g) in 1,4-dioxane (0.12 mol, 100 ml). The reaction mixture was stirred and heated at 50°C for 30 min. The mixture was cooled before 1-bromobutane (0.21 mol, 28.77g) was slowly added to the mixture and refluxed for 6 hours. The refluxed solution was allowed to cool to room temperature and then poured into water. This solution was extracted twice with diethyl ether and dried over anhydrous sodium sulfate. The dried solution was filtered and rotovaped. The resulting product was a yellowish liquid 2,5-bis(butylthio)-1,3,4-thiadiazole (mol. wt. 262.46). The yield was 73% (19.1 g). The boiling point of the compound was 382-384°C at atmospheric pressure. Final product was characterized by ^{13}C, ^{1}H NMR, and MS. ^{13}C, ^{1}H NMR, and MS. The Bu-MTT-Bu showed ^{13}C peaks in d-DMSO at 159.39 (–N=C–S–), 14.67 (CH$_3$), 22 (–S-CH$_2$), 34.0 and 36.2 ppm (CH$_2$-); ^{1}H peaks in d-DMSO triplet peaks at 3.2 (S–CH$_2$), multiple peaks at 1.46 and 1.68 (-CH$_2$), and triplet peak at 1.1 ppm, and GC–MS parent peak at 262 and 205. Significant m/z peaks at 133 and 57.

2.6 Synthesis of 2,5-Bis(thioacetic acid)-1,3,4-Thiadiazole (A-MTT-A) [22]

5-Mercapto-1,3,4-thiadiazole-2(3H)-thione (75 g, 0.5 mol) was added to an aqueous solution of chloroacetic acid (94.5 g, 1 mol) and sodium carbonate (53 g, 0.5 mol). The reaction mixture was stirred and refluxed for 3 hours. The refluxed solution was then allowed to cool down to room temperature, then concentrated hydrochloric acid was added with stirring until pH = 2 with formation of white crystals. The precipitate was filtered off and washed with distilled water. The resulting product was 2,5-bis(thioacetic acid)-1,3,4-thiadiazole (mol. wt. 266.32). The product was dried in vacuo to afford white crystals and the yield was 83% (110.51 g). The melting point of the compound was 164-165 ^{o}C. Final product was characterized by ^{13}C, ^{1}H NMR, IR, and MS. The A-MTT-A showed ^{13}C peaks in d-DMSO at 164.56 (–N=C–S–), 169.11 (–CO$_2$H), and 35.74 ppm (–CH$_2$–); ^{1}H peaks in d-DMSO, singlet at 4.11 (–CH$_2$) and 11.46 ppm (–OH); IR bands at 3410, 2920, 2830, 1750, and 1600 cm^{-1}. MS peaks at 262, 207, 131,91 and 59.

2.7 Test Protocol

All electrochemical studies were carried out in 3.5 % NaCl solution using a conventional Princeton flat cell model K0235 comprising a mild steel substrate or 304 stainless steel with an exposed area of 1 cm^2 as a working electrode (WE), saturated calomel electrode as a references electrode (SCE), and platinum foil as a counter electrode. Reference electrode was brought to close proximity with the working electrode by a Luggin capillary. Prior to each experiment the WE was polished with 1200 grade emery paper, washed with distilled water and acetone.

To prepare the saturated solutions, the compounds under investigation were added to a 3.5% NaCl solution at its maximum solubility and stirred overnight then filtered. Also, in order to get a quantitative comparison, the measurements were carried out on steel substrates exposed to sodium chloride solutions containing the same concentration of inhibitor, 50 ppm. The Bu-MTT-Bu has low solubility in water 1.7 ppm, thus it has been excluded from 50 ppm measurements. Measurements were recorded after 1 h of exposure of the working electrode in the test solution at room temperature. Each test was repeated five times on different specimens in five different solutions at the same concentration to confirm its reproducibility.

2.8 Electrochemical Impedance Measurements

Electrochemical impedance measurements were carried out at open circuit potential OCP. Measurement system was composed of a Solartron SI 1260 impedance gain-phase analyzer connected to a Solartron 1287 electrochemical interface. The amplitude of sine wave signal was 10 mV, and the frequency range extended from 100 kHz to 0.01Hz for steel specimens and from 100 kHz to 0.1 Hz for 304 stainless steel specimens. The impedance spectra were simulated by ZView software from Scribner Associates, Inc.

2.9 Polarization Measurements

The potentiodynamic polarization measurements were performed immediately after the EIS on the same electrode. Potential range of ±250 mV with respect to open circuit potential, and a scan rate of 2mV/sec were applied.

3. RESULTS AND DISCUSSION

## 3.1 Electrochemical Impedance Spectroscopy (EIS)

Figure 4 and Figure 5 show the Nyquist plot for steel substrates exposed to 3.5% NaCl solution containing either saturated or 50 ppm MTT derivatives at room temperature. It is obvious from the results that the addition of MTT derivatives causes significant change in the impedance response. The impedance data were analyzed and interpreted in terms of an equivalent standard circuit displayed in Fig (6). This circuit has been generally used to describe the inhibition mechanism of organic compounds [23]. The circuit consists of a solution resistance (R_Ω), a constant phase element (CPE), and a charge transfer resistance (Rct). The introduction of CPE instead of the double layer capacitance C_{dl} is to get accurate impedance fitting of the electrical double layer. The impedance of a CPE is given by:

$$Z_{CPE} = \frac{1}{Y_O (j\omega)^n} \tag{1}$$

Where Y_o is the magnitude of CPE, ω is the angular frequency (in rad s^{-1}), j is the imaginary number where $j^2 = -1$, and n is a CPE exponent (phase shift) that indicates the roughness of surface and ranges from 0 to 1 [24]. The capacitance values can be derived from the CPE parameter value Y_o and n by using the expression:

$$C_{dl} = (Y_O . R_{ct}^{1-n})^{1/n} \tag{2}$$

The characteristic parameters associated with the impedance response, charge transfer resistance, double layer capacitance and the inhibition efficiency are tabulated in Table 2 & 3.
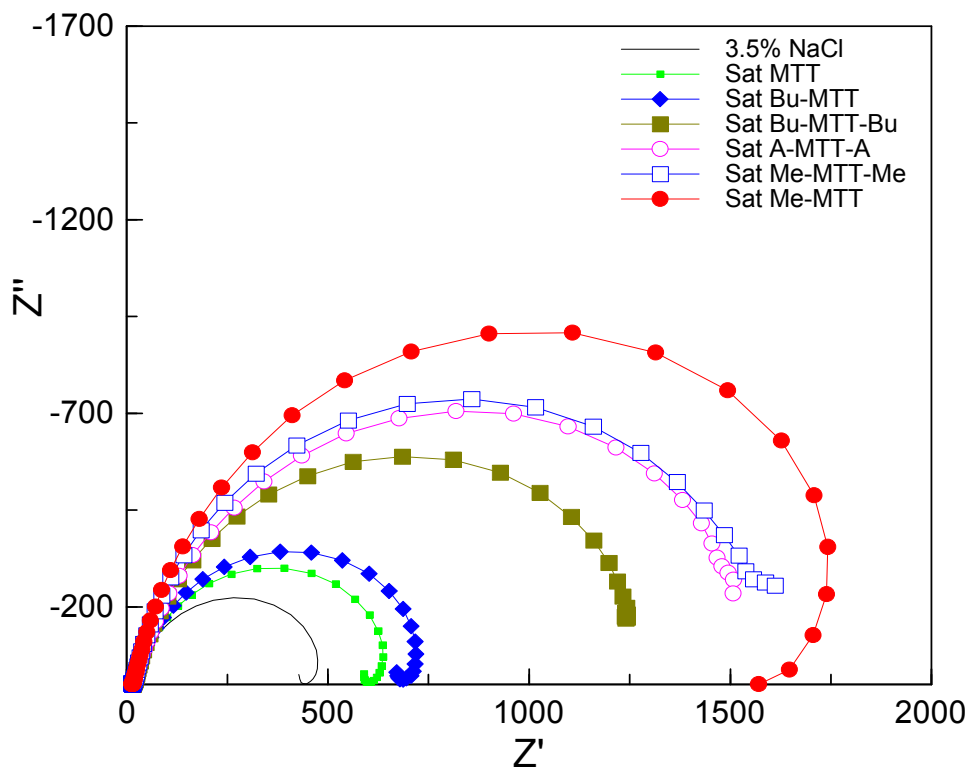
Fig.4. Nyquist plot of steel in 3.5% NaCl solutions with and without addition of saturated MTT derivatives.
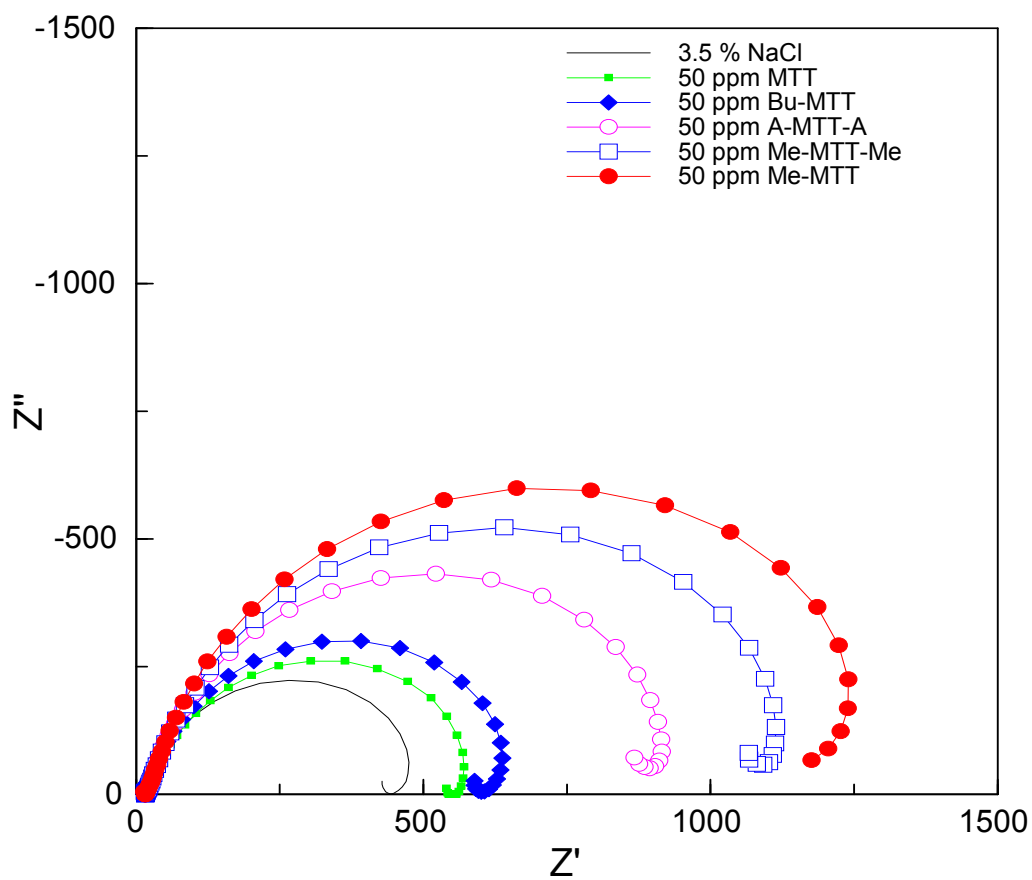
Fig. 5. Nyquist plot of steel in 3.5% NaCl solutions with and without addition of 50 ppm MTT derivatives.
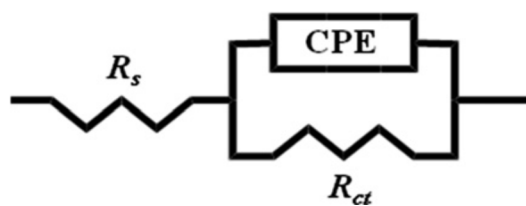
Fig. 6. Equivalent circuit for impedance analysis.

Table 2
Parameters of EIS spectra obtained for steel in the absence and the presence of saturated MTT derivatives.

Compounds	Rct (Ω cm^2)	Cdl (μF cm^{-2})	E% *
Blank	433	380	--
MTT	585	374	26
Me-MTT	1870	339	77
Bu-MTT	750	365	42
Me-MTT-Me	1472	344	70
Bu-MTT-Bu	1170	356	63
A-MTT-A	1402	352	69

* Inhibition efficiency calculated from equation 3

Table 3
Parameters of EIS spectra obtained for steel in the absence and the presence of 50 ppm MTT derivatives.

Compounds	Rct (Ω cm^2)	Cdl (μF cm^{-2})	E% *
Blank	433	380	--
50 ppm MTT	522	375	17
50 ppm Me-MTT	1466	346	70
50 ppm Bu-MTT	698	371	38
50 ppm Me-MTT-Me	1170	355	63
50 ppm A-MTT-A	984	358	56

* Inhibition efficiency calculated from equation 3

The shape of the Nyquist plot indicates a charge transfer process [23]. The diameter of the semi-circle of steel samples exposed to a solution containing MTT derivatives have larger radius than the blank control solution. Consequently, the charge transfer resistance values in the presence of MTT derivatives were higher than the blank solution. It was also observed that the charge transfer resistance values increases only moderately as the MTT derivatives concentration increases from 50 ppm to the saturated state. This indicated that the MTT derivatives are most likely functioning by surface adsorption. Corrosion rate is inversely proportional to the value of charge transfer resistance, thus, Rct values can be used to calculate the inhibition efficiency by applying the following equation:

$$E(\%) = \frac{Rct - R^{O}ct}{Rct} \times 100 \tag{3}$$

Where, Rct and R^{o}ct are the charge transfer resistances of substrate with and without inhibitors, respectively. Charge transfer resistance (Rct) can also be used as an indication of protective film formation on substrate surface. The adsorption of organic molecules on a metal surface causes water molecules to be displaced from the surface, thus, increasing the charge transfer resistance. The higher the Rct, the better the formation of the protective layer [25,26]. Furthermore, the results show that the electrical double layer capacitance decreases as a result of adding MTT derivatives to the NaCl solution. This may also be attributed to the adsorption of MTT derivatives on metal surface. The existence of double layer at metal surface and solution interface can be substantially altered by the

adsorption of organic molecules. The altering of the water layer lowers the dielectric constant and decrease the double layer capacitance [27]. The double layer capacitance can be related to dielectric constant and thickness of double layer by the following formula:

$$C_{dl} = \frac{\varepsilon \varepsilon_o A}{d}$$ (4)

Where C_{dl} is double layer capacitance, ε the dielectric constant of the water layer, ε_o is the dielectric constant of free space (8.854×10^{-12} F/m), A is the substrate exposure area, and d is double layer thickness.

The increase in R_{ct} and decrease of C_{dl} upon addition of MTT derivatives suggested that the MTT derivatives is functioning by adsorption on the metal surface and blocking the active site of the metal.

The corrosion behavior of the 304 stainless steel specimens was investigated using electrochemical impedance spectroscopy in 3.5%NaCl. Nyquist plot, Fig 7 shows that the charge transfer resistance, Rct, dramatically increases upon addition of the MTT derivatives, which indicate the inhibition effect of these compounds. Values of the associated parameters are presented in Table 4. The results for 304 stainless steel paralleled the results for the steel substrate with only small difference in the percent inhibition.
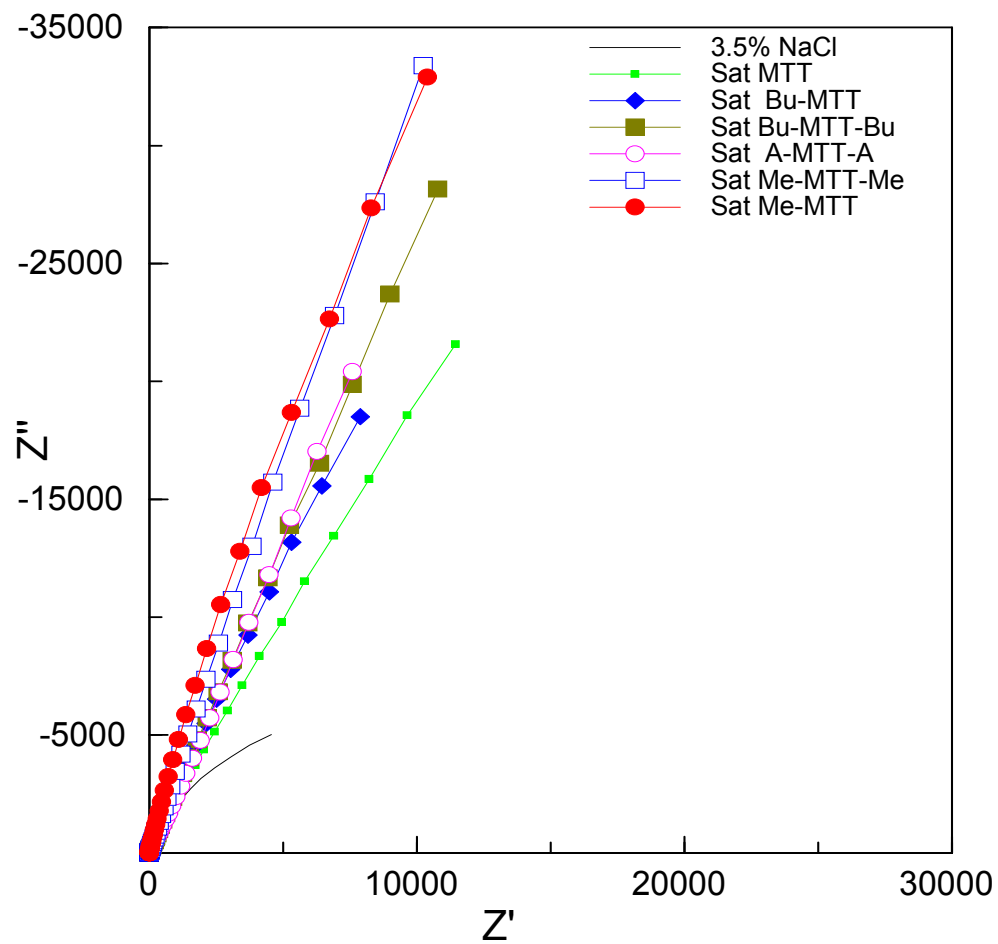
Fig. 7. Nyquist plot of 304 stainless steel in 3.5% NaCl solutions with and without addition of saturated MTT derivatives.
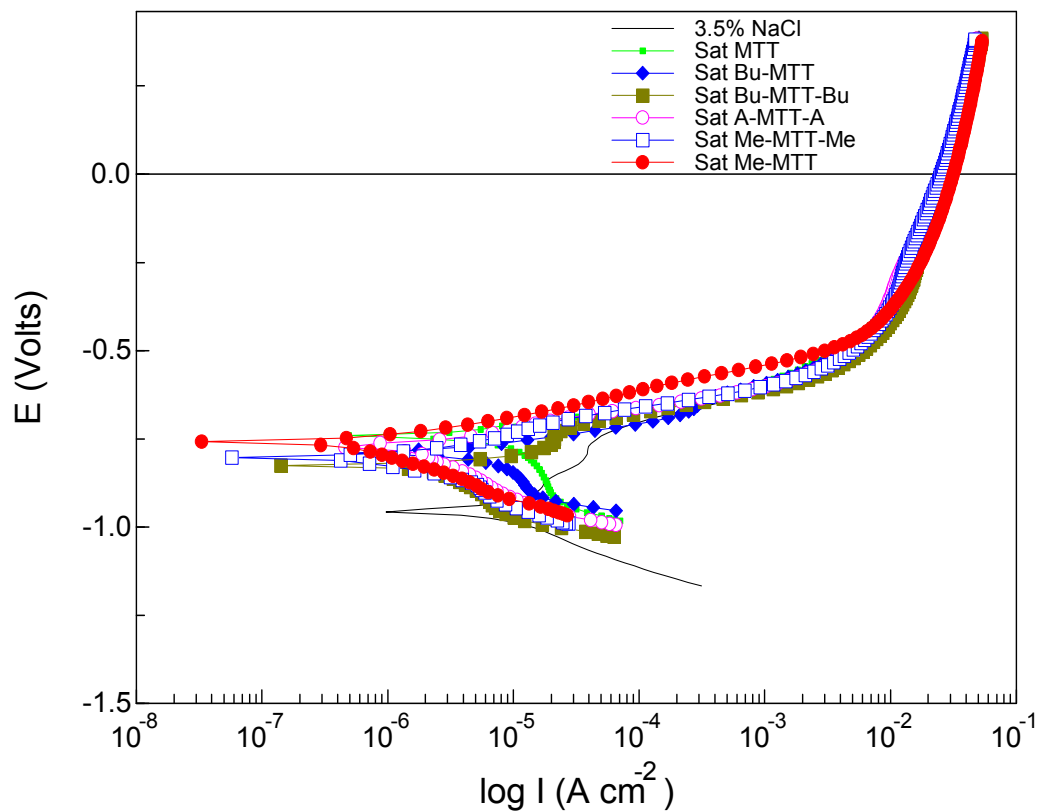
Table 4
Parameters of EIS spectra obtained for 304 stainless steel in the absence and the presence of saturated MTT derivatives.

Compounds	R_{ct} (kΩ cm^2)	C_{dl} (μF cm^{-2})	E%*
Blank	10.9	23.1	--
MTT	15.5	20.5	30
Me-MTT	72.6	6.7	85
Bu-MTT	21.9	20.1	50
Me-MTT-Me	68.3	8.4	84
Bu-MTT-Bu	31.1	9.9	64
A-MTT-A	41.8	9.2	74

* Inhibition efficiency calculated by equation 3

3.2 Tafel Extrapolation

The potentiodynamic polarization curves for steel substrates exposed to 3.5% NaCl in the presence and the absence of either saturated or 50 ppm MTT derivatives are shown in Fig 8 and Fig 9. The pertinent parameters to electrochemical process of each curve were derived by evaluation and extrapolation of both the anodic and cathodic region of the tafel plots; i.e. corrosion current density (icorr), corrosion potential (Ecorr), and cathodic and anodic tafel slopes (βc and βa). Data analysis was conducted by using CorrView software. Different concentrations of MTT derivatives do not affect corrosion potential significantly, but did affect the corrosion current. Values presented are the average value of five experiments. All data are summarized in Table 5 and 6.

Fig.8. Polarization curves of steel in 3.5% NaCl solutions with and without addition of saturated MTT derivatives.
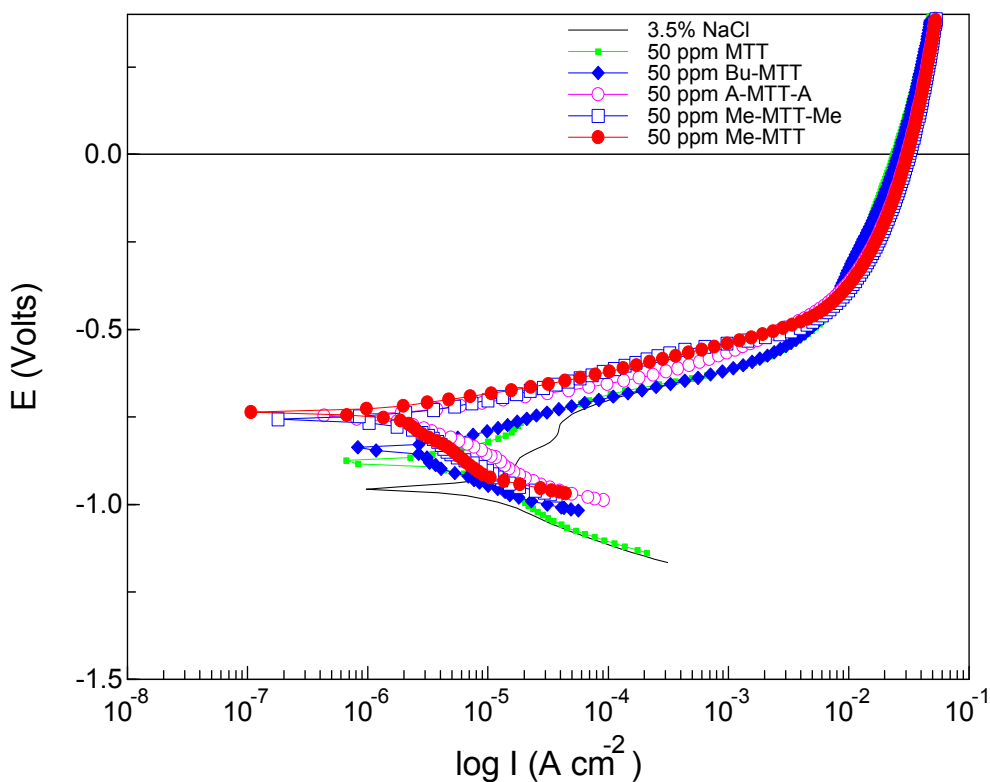
Fig. 9. Polarization curves of steel in 3.5% NaCl solutions with and without addition of 50 ppm MTT derivatives.

Table 5
Potentiodynamic polarization parameters obtained for steel in the absence and the presence of saturated MTT derivatives.

Compound	Ecorr mV	βa mV/decade	βc mV/decade	I_{cor} μA/cm^2	Inhibition efficiency E%*
Blank	-890	153	138	7.23	--
MTT	-742	60	140	5.56	23
Me-MTT	-766	70	154	1.09	85
Bu-MTT	-794	60	100	3.91	46
Me-MTT-Me	-802	70	190	1.99	72
Bu-MTT-Bu	-841	80	213	2.80	61
A-MTT-A	*-774*	60	221	2.14	70

* Inhibition efficiency calculated using equation 5.

Table 6
Potentiodynamic polarization parameters obtained for steel in the absence and the presence of 50 ppm MTT derivatives.

Compound 50 ppm	Ecorr mV	βa mV/decade	βc mV/decade	I_{cor} μA/cm^2	Inhibition efficiency E%*
Blank	-890	153	138	7.23	--
MTT	-749	80	110	5.99	17
Me-MTT	-740	60	120	1.45	80
Bu-MTT	-780	100	110	4.50	38
Me-MTT-Me	-790	77	110	2.63	63
A-MTT-A	-750	60	80	2.81	61

* Inhibition efficiency calculated using equation 5.

Figure 10 shows the polarization curves of the 304 stainless steel immersed in 3.5% NaCl. The values of the corrosion current density (icorr), corrosion potential (Ecorr), and the cathodic and anodic tafel slopes (βc and βa) are calculated and displayed in Table 7:
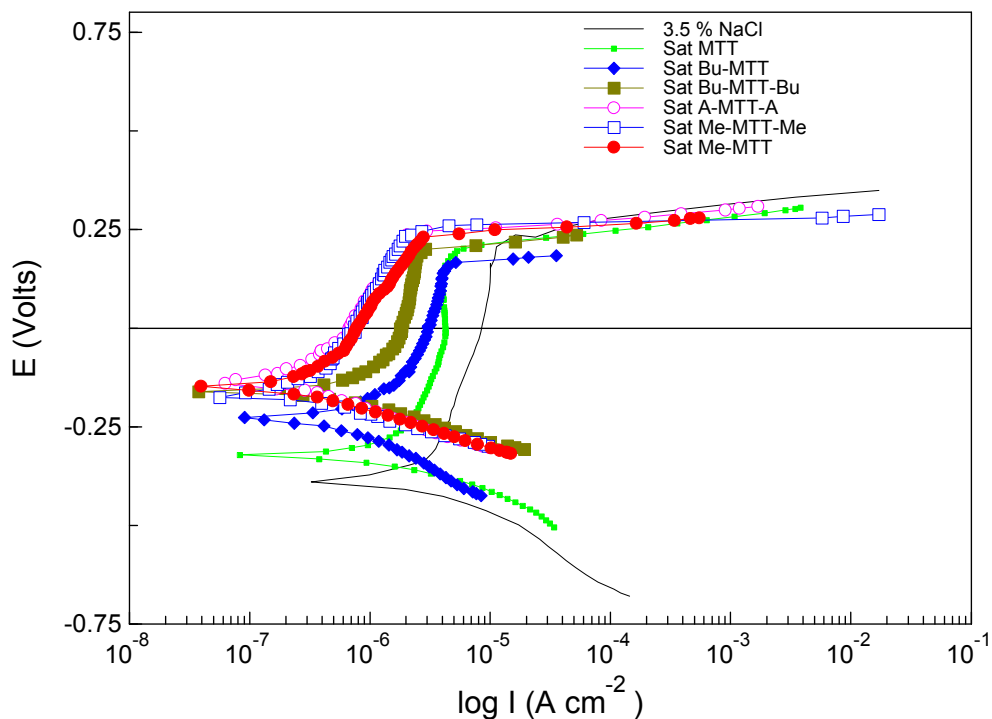
Fig. 10. Polarization curves of 304 stainless steel in 3.5% NaCl solutions with and without addition of saturated MTT derivatives.

Table 7
 Potentiodynamic polarization parameters obtained for 304 stainless steel in the absence and the presence of saturated MTT derivatives.

Compound	Ecorr mV	βa mV/decade	βc mV/decade	I_{cor} $\mu A/cm^2$	E%[*]
Blank	-360	90	50	0.79	--
MTT	-320	85	55	0.50	37
Me-MTT	-150	68	30	0.09	88
Bu-MTT	-230	100	100	0.34	57
Me-MTT-Me	-160	100	100	0.11	86
Bu-MTT-Bu	-160	100	60	0.28	64
A-MTT-A	-150	90	50	0.18	77

[*] Inhibition efficiency calculated using equation 5.

It can be clearly seen from the figures 8, 9, and 10 that the presence of MTT derivatives caused a reduction in the corrosion current. The inhibition efficiency was calculated from the following formula:

$$E(\%) = \frac{i_o - i}{i_o} \times 100$$

(5)

Where i_o and i are the value of corrosion current density in the absence and the presence of inhibitors, respectively.

The presence of MTT derivatives results in the E_{corr} values which were shifted toward more positive potential suggesting that these inhibitors are blocking the active sites by adsorption on metal surface [15, 17]. According to Riggs [28], the classification of a compound as an anodic or cathodic inhibitor is feasible when the OCP displacement is at least 85mV in relation to that measured for the blank solution. The OCP displacement associated with the addition of MTT derivatives is greater than 85 mV, therefore, the MTT derivatives acted as an anodic inhibitor. These results agreed with previous finding that MTT inhibited the corrosion by forming a mono layer on steel and stainless steel substrates and inhibit both anodic and cathodic reactions with an anodic predominance [15, 17, 29].

The inhibition efficiency E% of the MTT derivatives tested decreases in the order Me-MTT> Me-MTT-Me > A-MTT-A > Bu-MTT-Bu> Bu-MTT > MTT

There was a slight improvement in inhibition efficiency of MTT derivatives for 304 stainless steel over the steel substrate. This difference may be explained in view of the previous finding that MTT has a greater affinity toward copper substrates [15, 17]. The 304 stainless steel contains 0.48% Cu. However, the corrosion current was an order of magnitude lower for stainless steel than regular steel.

The mono substituent derivative Me-MTT shows the most effective inhibition. Similar performance has been noted with di substituent Me-MTT-Me, which displays good corrosion protection. The -CH$_3$ group acts as an electron donating group and enhances the electron density at the active adsorption sites (sulfur atoms) [4,5]. The other important factor that predetermines the greatest inhibition potency of mono and di methylated MTT may be the size of methyl group. The steric hindrance effect of a -CH$_3$ group is minimal due to its small size. As a consequence, there is no significant congestion around sulfur atoms, and can easily adsorb and pack on a metal substrate. Previous studies [30, 31] discussed the adsorption modes of thiophene derivatives. They reported the possibility of two adsorption modes, parallel and vertical see figure 11. For imidazole derivatives the small size of –CH$_3$ groups allows it to reside on metal surface in parallel resulting in better surface coverage [32]. The effectiveness of mono and di methylated MTT over the MTT itself can be attributed to the presence of hydrophobic –CH$_3$ groups that help the displacement of water molecules from the metal substrate. Additionally, the superiority of inhibition efficiency of Me-MTT over Me-MTT-Me is probably due to better packing on

metal surface. Also the presence of the N-H bond in Me-MTT may also contribute to its efficiency. The N-H bond can establish hydrogen bonding with an oxygen atom in a surface metal oxide resulting in increased adhesion of the protective film [6]. It is also possible that the thione may exist as the thiol form, a tautomer, when bonded to the metal surface.
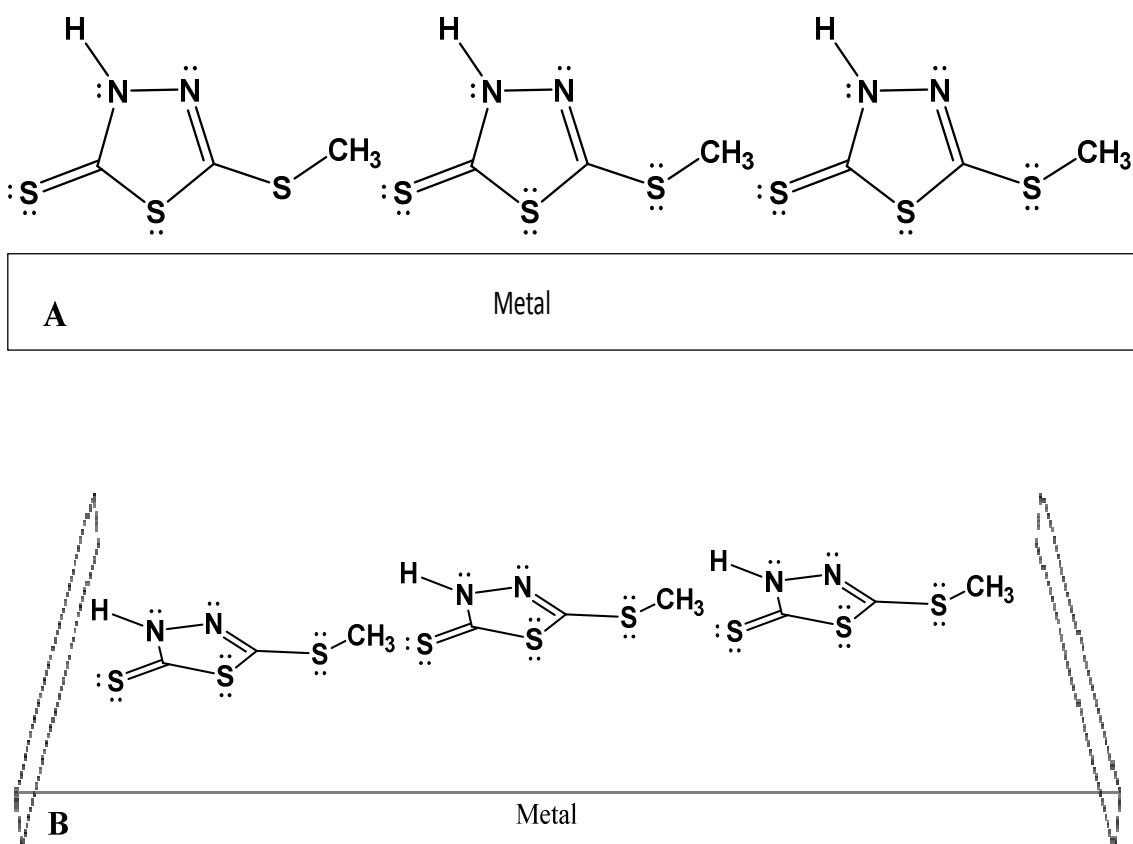
Fig. 11. Schematic of possible adsorption modes and packing suggested of Me-MTT on substrate surface: vertical mode (A), and parallel mode (B).

The mono and di butylated MTT showed lower inhibition. Previous study [33,34] on corrosion inhibition ability of bis-thiadiazole derivatives (1,3,4-thiadiazol-2-amine, 5,5'-methylenebis and 1,3,4-thiadiazol-2-amine, 5,5'-(1,2-

ethanediyl)bis-)   and 2-amino-5-alkylthiadiazole derivatives as a corrosion inhibitors of mild steel and carbon steel in 1 M HCl and H_2SO_4 have been performed. It has been concluded that the presence of long aliphatic chains showed better inhibition and was attributed to the increase in size of the molecule. However, the presence of the C_4H_9 bulky group on sulfur atoms may cause a steric effect which reduces the packing density on the surface. The lowest protection performance of mono and di butylated MTT is adsorption mode that the bulky butyl groups in mono and di butylated MTT resides on metal surface perpendicularly in order to minimize steric effect (see figure 12) [32]. This stacking mode results in less surface coverage and lower hydrophobic effect [32]. The better performance of Bu-MTT-Bu over Bu-MTT is probably due to the greater hydrophobic effect [33]. The Bu-MTT-Bu has the lowest solubility in water among all the MTT derivatives (1.7 ppm), but Bu-MTT-Bu shows inhibition ability close to Me-MTT-Me inhibition ability. The inhibition ability of Bu-MTT-Bu can be attributed to the greater hydrophobicity effect of long aliphatic chain. It would be concluded that in addition to electronic interaction, there are two factors that govern the MTT derivatives corrosion inhibition performance; hydrophobicity and steric hindrance.
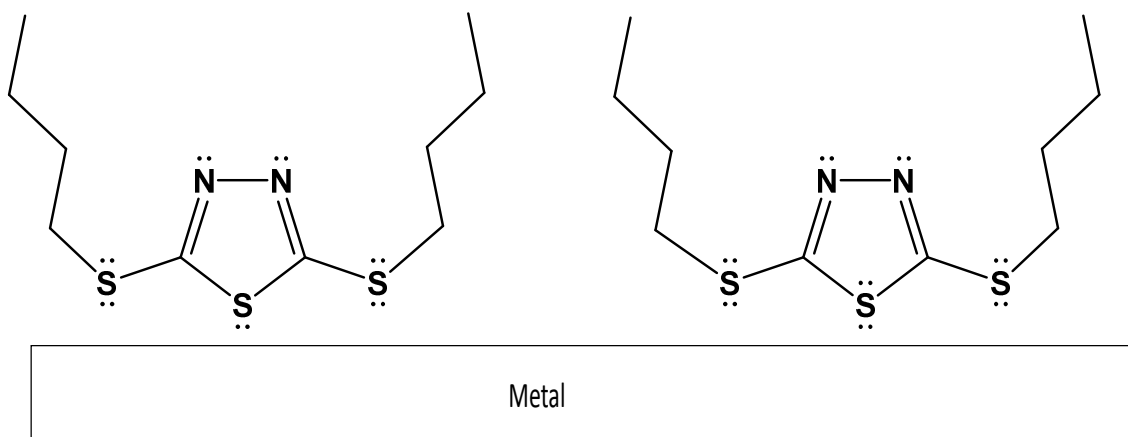
Fig. 12. Schematic of possible adsorption mode and packing suggested of Bu-MTT-Bu on substrate surface.

The di-acetic acid A-MTT-A showed good inhibition efficiency. This can be attributed to the presence of extra electron donor atoms. Oxygen atoms act as an additional adsorption active site [1]. Thus, adsorption of the protective layer may be enhanced [1]. Previously, A-MTT-A has been tested as a flash rust inhibitor [22] and it showed excellent inhibition ability.

3.3 Theoretical Calculation

In order to get a better insight into the electronic interaction of MTT derivatives with steel and stainless steel surfaces, the quantum chemical parameters were calculated with B3LYP functional at basis set 6-311G. Table 8 summarized the E_{HOMO}, E_{LUMO}, energy different $E_{HOMO-ELUMO}$, and dipole moment μ.

Table 8
Molecular properties of MTT compounds using B3LYP.

Compound	E_{HOMO} Hartree	E_{LUMO} Hartree	E_{HOMO}- E_{LUMO}	Dipole moment μ Debye
MTT	-0.23535	-0.0642	-0.17115	5.803
Me-MTT	-0.23208	-0.0620	-0.17008	7.184
Bu-MTT	-0.23145	-0.0614	-0.17005	7.861
Me-MTT-Me	-0.23159	-0.0485	-0.18305	0.524
Bu-MTT-Bu	-0.23011	-0.0474	-0.18265	0.152
A-MTT-A	-0.23921	-0.0534	-0.18578	2.978

The correlations between experimental inhibitor efficiency and quantum chemical parameters are displayed in Figure.13.
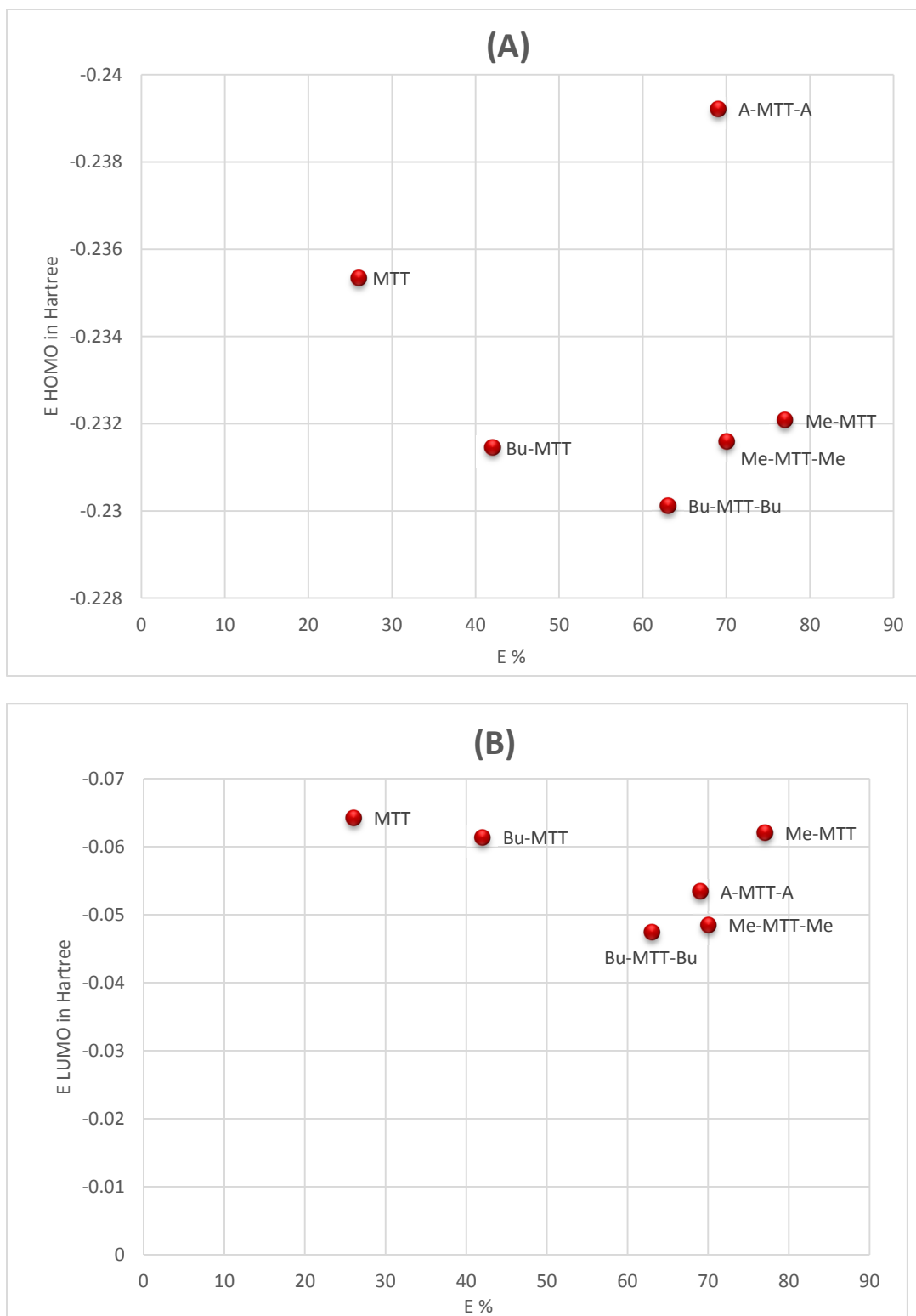
Fig.13. Correlation between quantum parameters and inhibitor efficiency E%: E$_{HOMO}$ (A); E$_{LUMO}$ (B); E$_{HOMO}$-E$_{LUMO}$ (C); and Dipole moment μ (D).
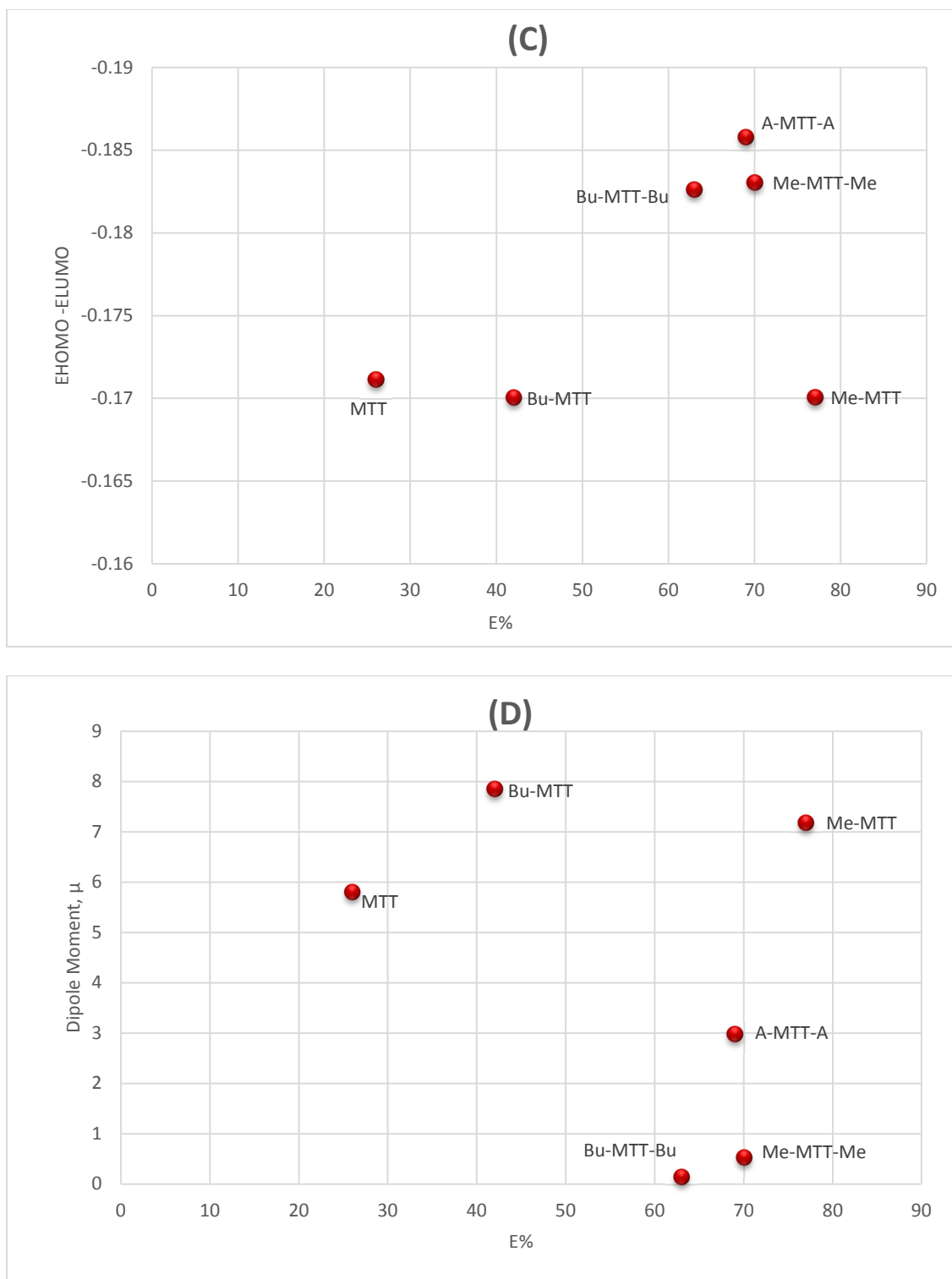
Fig.13. Correlation between quantum parameters and inhibitor efficiency E%: E_{HOMO} (A); E_{LUMO} (B); E_{HOMO}-E_{LUMO} (C); and Dipole moment μ (D).

Figure 13 revealed no good correlation between the quantum parameters and inhibitor efficiency. The inhibition ability of the MTT derivatives may be dominated in part by steric hindrance. The electron interaction between the MTT derivatives and metal substrates is not only the factor controlling the inhibition performance of these molecules.

Electron densities on each atom have also been calculated in order to determine the most possible adsorption site of MTT molecules. Atoms with the highest electron density are the preferred center for ligation [35,36]. Figure 14 and table 9 display the electron density on all adsorbing centers of MTT derivatives.
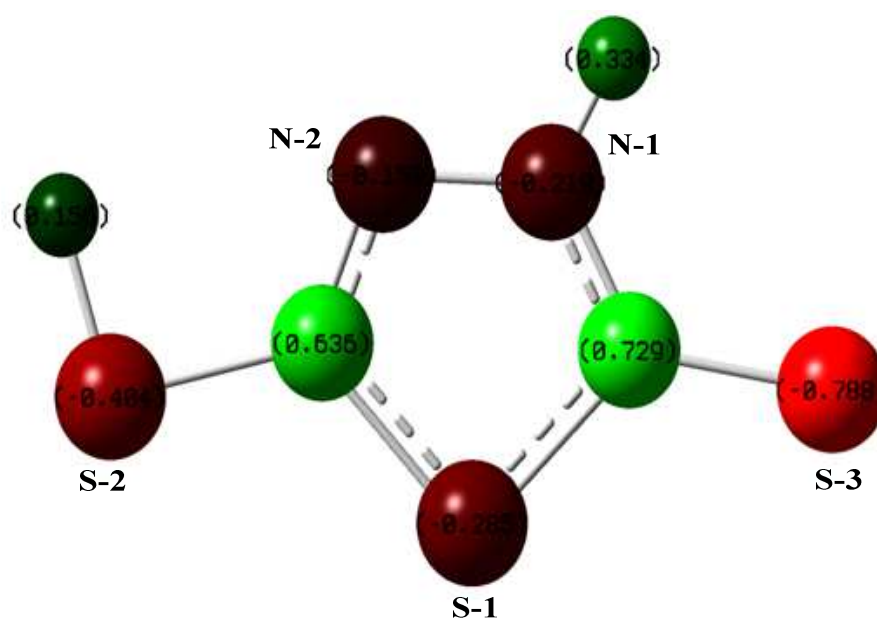
Fig. 14. Charge distribution of MTT.

Table 9
Electron density of MTT derivatives.

	N-1	N-2	S-1	S-2	S-3	O-1	O-2
MTT	-0.218	-0.150	-0.285	-0.404	-0.788	--	--
Me-MTT	-0.287	-0.060	-0.373	-0.376	-0.787	--	--
Bu-MTT	-0.339	-0.005	-0.408	-0.525	-0.809	--	--
Me-MTT-Me	-0.214	-0.214	-0.364	-0.415	-0.560	--	--
Bu-MTT-Bu	-0.206	-0.206	-0.380	-0.560	-0.560	--	--
A-MTT-A	-0.204	-0.204	-0.368	-0.485	-0.485	-0.491	-0.401

Table 9 shows that there is a variation in negative charges located on the sulfur and nitrogen atoms in all MTT derivatives. These atoms act as nucleophilic agents, and they would be the most favorable points of interaction between MTT derivatives and metal surface [16]. The performance benefit for the alkylated MTT is likely in part due to the higher charge density on S-1, for all the derivatives. As the charge density of thiazole ring atoms is pronounced, it is possible to expect these atoms can adsorbed on the surface, and the parallel adsorption mode is anticipated to be the most possible mode. Previous studies [31,37] on thiophene and pyridine derivatives found the existence of two adsorption modes. However, the steric hindrance effect of long aliphatic chain in Bu-MTT may lower the stacking density and contribute in low inhibition performance see figure 12. Oxygen atoms in A-MTT-A have also showed high electron density and contribute in molecule surface interaction.

4. CONCLUSION

1- By derivatizing MTT, the corrosion inhibition ability for steel and
   304 stainless steel in 3.5% NaCl solutions was improved.

2- The electrochemical measurement results indicated that the inhibition
   efficiency of MTT derivatives of steel and 304 stainless steel in 3.5%
   NaCl were in the following order Me-MTT> Me-MTT-Me > A-MTT-A >
   Bu-MTT-Bu> Bu-MTT > MTT.

3- The inhibitive impact of MTT derivative is affected by the nature and
   size of substituent group.

4- Hydrophobicity aids and steric hindrance reduces the performance of
   the inhibitor .

5- Mono and di methylated MTT were found to be the most effective
   corrosion inhibitors on both steel and stainless steel.

6- The MTT derivatives inhibit corrosion process by forming a protective
   film on metal substrate. They function in part by inhibit the anodic
   reactions.

7- There was a good agreement between the results obtained by
   polarization measurements and EIS.

8- The theoretical study showed that the inhibitors efficiency does not
   directly correlate with quantum chemistry parameters. This may
   propose that the corrosion protection mechanism of MTT derivatives is
   governed by both electronic and steric hindrance effect.

9- The characterization of corrosion inhibition efficiency of MTT derivatives
   has to be made in terms of a combination of several molecular

structure parameters. An individual parameter is not adequate to provide clear explanations of molecule inhibition ability.

5. ACKNOWLEDGMENTS

6. REFERENCES

[1] V. S. Sastri, Corrosion inhibitors Principle and Applications, John Wily & Sons. Ltd., New York, 1998.
[2] I.L.Rozenfeld, Corrosion Inhibitors, McGraw-Hill Inc., New York, 1981.
[3] L.R .Every, L.O Riggs, Materials Protection, 3(9) (1964), 46-47.
[4] R.R. Annand, R.M. Hurd, N. Hackerman, J.Electrochem.Soc. 112 (1965) 138-144.
[5] G.Trabanelli, V. Carassiti, Advanced in Corrosion Science and Technology, Plenum Press. 1(1970) 147-228.
[6] P. Li, T.C.Tan, J.Y.Lee, Corrosion (NACE). 53 (1997) 186-194.
[7] J. Fang, J. Li, Journal of Molecular Structure. 593 (2002) 179–185.
[8] E.H. El Ashry, A. El Nemr, S. A. Esawy, S. Ragab, Electrochimica Acta. 51 (2006) 3957–3968.
[9] Gokhan Gece, Corrosion Science 50 (2008) 2981–2992.
[10] Z. Zhou, R.G. Parr, J. Am. Chem. Soc. 112 (1990) 5720–5724.
[11] V.S. Sastri, J.R. Perumareddi, Corrosion (NACE). 53 (1997) 617-622.
[12] V.S. Sastri, J.R. Perumareddi, Corrosion. 50 (1994) 432-437.
[13] M. Sahin, G. Gece, F. Karcı, S. Bilgic, J Appl Electrochem, 38 (2008) 809–815.
[14] G Gao, C Liang, Electrochimica Acta. 52 (2007) 4554–4559.
[15] Ting Ting Qin, Jun Li, Hong Qun Luo, Ming Li, Nian Bing Li, Corrosion Science. 53 (2011) 1072–1078.
[16] Wen Chen, Hong Qun Luo, Nian Bing Li, Corrosion Science. 53 (2011) 3356–3365.

[17] Wen Chen, Song Hong, Hua Bing Li, Hong Qun Luo, Ming Li, Nian Bing Li, Corrosion Science. 61 (2012) 53–62.

[18] J. K. Mistry, R. Dawes, A. Choudhury, M. R. Van De Mark, Journal of Heterocyclic Chemistry. 51(2014) 747-754.

[19] A.R. Katritzky, Z. Wang, R.J Offerman, Journal of Heterocyclic Chemistry. 27(1990) 139-142.

[20] G. D. Thorn, R. A. Ludwig, Canadian Journal of Botany.36 (1958) 389-392.

[21] G.A.Tashbaev, I.M Nasyrov, K.S. Zakharov, L.A Zegel'man, Izvestiya Akademii Nauk Tadzhikskoi SSR, Otdelenie Fiziko-Matematicheskikh, Khimicheskikh i Geologicheskikh Nauk. 1 (1991) 88-89.

[22] E. Sianawati, J.K. Mistry, M.R. Van De Mark, European Coatings Journal. 12 (2008) 35-39.

[23] K.F. Khaled, M. A. Amin, Corrosion Science. 51 (2009) 1964–1975.

[24] D.A. Lopez, S.N. Simison, S.R. Sanchez, Electrochim. Acta 48 (2003) 845–854.

[25] S. Muralidharan, K.L.N. Phani, S. Pitchumani, S. Ravichandran, S.V.K. Iyer, J. Electrochem. Soc. 142 (1995) 1478-1483.

[26] P. Kern, D. Landolt, Electrochimica Acta. 47 (2001) 589–598

[27] E.Mc. Cafferty, N. Hackerman, J. Electrochem. Soc. 119 (1972) 146-154.

[28] O. L. Riggs, Jr., in C. C. Nathan (Ed.), Corrosion Inhibitors, 2nd edition. NACE,Houston, TX, 1973.

[29] C.T. Wang, S.H. Chen, H.Y. Ma, C.S. Qi, J. Appl. Electrochem. 33 (2003) 179–186.

[30] M. Lashgari, M.R Arshadi, M. Biglar, Chemical Engineering Communications 197(2010), 1303-1314.

[31] M. Bouklah, B. Hammouti, M. Benkaddour, T. Benhadda, Journal of Applied Electrochemistry, 35 (2005), 1095-1101.

[32] Seung-Hyun Yoo , Young-Wun Kim, Kunwoo Chung, Seung-Yeop Baik, Joon-Seop Kim, Corrosion Science. 59 (2012) 42–54

[33] A. K. Singh, M.A. Quraishi, Corrosion Science. 52 (2010) 1373–1385.

[34] O. Olivares-Xomet, Natalya V. Likhanova, Noel Nava, Agustín Cabral Prieto. Int. J. Electrochem. Sci., 8 (2013) 735 – 752.

[35] A. Y. Musa, A. Mohamad, A. H. Kadhum, M. S. Takriff, W. Ahmoda, Journal of Industrial and Engineering Chemistry. 18 (2012) 551–555.

[36] I. Lukovits, E. Kalman, F. Zucchi, Corrosion, 57(2001), 3-8.

[37] Lashgari, M., Arshadi, M. R., and Parsafar, Gh. A, Corrosion, 61(2005), 778–783.

SECTION

2. SUMMARY

Two acrylic copolymers were synthesized, and colloidal unimolecular polymer (CUPs) suspension system was prepared through water reduction process. The CUP particles of the two copolymers are true nano scale particles, their measured size is 4.1 and 6.5 nm. The CUP systems were studied by low field proton NMR. The bound water fraction was determined using spin-lattice relaxation T_1 measurements. The existence of bound water layer was confirmed, and particles with 6.2 nm diameter hold thicker water layer thickness than particle with 4.1 nm. The charge density on CUP surface is the key role in determining the amount of bound water. The increase of CUP associated with a decrease in measured spin lattice relaxation time due to the increase of bound water population.

Variable temperature ^{13}C Solid state NMR was used to examine the polymer chain dynamics of a homopolymer and a copolymer. A method that relies on obtaining ^{13}C NMR spectra free of rotational echoes was used. The magic angle spinning of the sample with polarization and the pulse sequence for total spinning sideband suppression CP-TOSS was used. Measurement of peak intensity decay as a function of temperatures provided an information about the segment onset motion, Tg. Results were compared with results obtained by differential scanning calorimetry (DSC) technique with exactly agreement.

The substitution of 5-mercapto-1,3,4-thiadiazole-2(3H)-thione MTT at thion-thiol position were carried out. Five MTT derivatives were synthesized and characterized including MTT itself for their corrosion inhibition performance on both steel and stainless steel substrates. The substituent size was found to be crucial in the molecule inhibiting corrosion. The steric hindrance caused by the substituent prevents molecules from proper packing on metal surface.

VITA

Yousef Abobaker Dawib was born in Tripoli, Libya. In June 1996, he received his Bachelor's Degree in Chemistry from Tripoli University (Formerly known as Al-Fateh University). He worked in oil industry as a corrosion specialist in Waha Oil Company, major Oil Production Company in Libya. In Nov 2003, he received his Master Degree in corrosion science and engineering from The University of Manchester (Formerly known as UMIST). In March 2006, he joined Al Jabal Al Gharbi University, Faculty of Science, Al Zintan, Libya as a lecturer in Chemistry Department. In August 2009, he joined the Missouri University of Science and Technology to pursue a Ph. D degree in Chemistry and began his doctoral studies under the guidance of Dr. Michael R. Van De Mark. During the course of his Ph. D. work, Yousef worked as a Teaching Assistant for the Department of Chemistry and as a Research Assistant for Missouri S&T Coatings Institute. Yousef presented his research work in two conference articles, one poster, and he has submitted three articles for publication. In July, 2015, Yousef received his Ph.D. in Chemistry from Missouri University of Science and Technology.